

**Fermilab**

FERMILAB-THESIS-1999-39

**A Measurement of the Dijet Mass Differential  
Cross Section in  $p\bar{p}$  Collisions at  $\sqrt{s} = 1.8$  TeV**

by

**Björn Hinrichsen**

A thesis submitted in conformity with the requirements  
for the degree of Doctor of Philosophy  
Graduate Department of Physics  
University of Toronto

©Copyright by Björn Hinrichsen, 1999



# Abstract

We have used  $86 \text{ pb}^{-1}$  of data collected with the Collider Detector at Fermilab (CDF) to measure the cross section for production of two or more jets as a function of dijet invariant mass. The data are corrected for detector response and calorimeter resolution effects. Our results are compared with predictions from next-to-leading order Quantum Chromodynamics (QCD) and a measurement performed by the DØ experiment. We see a trend, similar to the excess observed in the inclusive jet cross section at high transverse energy, but find our data to be in agreement with the QCD predictions. The CDF and DØ data are in good agreement.



# Acknowledgements

Results in high energy physics are never the products of individuals. This analysis would not have been possible without the contributions and help from numerous people; to list them all is impossible.

Firstly, I would like to thank my supervisor, William Trischuk, for his guidance, insight and advice. He patiently read through the numerous drafts of this thesis and helped to make it a more complete work. It has been a pleasure to work with him.

I am indebted to Robert Harris for his extraordinary support throughout this analysis. His help and encouragement was of great value for me throughout this analysis.

I thank all my CDF colleagues at Fermilab, in particular Eve Kovács, Frank Chlebana, Tommaso Dorigo, Marjorie Shapiro, Brenna Flaughner and Jodi Lamoureux, who have contributed to this analysis through many helpful discussions.

Many thanks to the people in the CDF group in Toronto, especially to Pierre Savard for countless animated and stimulating discussions about the  $\chi^2$  procedure and to Wendy Taylor for having been a great office mate.

Finally, I thank Pekka Sinervo and Bob Orr for generously allowing me to switch thesis experiments for reasons that had nothing to do with physics.



# Contents

<b>Abstract</b>	<b>iii</b>
<b>Acknowledgements</b>	<b>v</b>
<b>Introduction</b>	<b>1</b>
<b>1 Theoretical Introduction</b>	<b>3</b>
1.1 The Standard Model: An Overview . . . . .	3
1.1.1 Matter . . . . .	3
1.1.2 Forces . . . . .	5
1.2 Quantum Chromodynamics and Jets . . . . .	8
1.2.1 The Static Quark Model . . . . .	9
1.2.2 The Quark-Parton Model . . . . .	10
1.2.3 QCD and the Running Coupling Constant . . . . .	11
1.2.4 Evolution Equations for the Parton Densities . . . . .	15
1.2.5 Jets in $p\bar{p}$ Collisions . . . . .	16
1.2.6 Jet Fragmentation . . . . .	16
1.3 The Dijet Mass Cross Section . . . . .	18

1.3.1	Leading Order QCD Subprocesses . . . . .	19
1.3.2	Higher-Order QCD Processes . . . . .	22
1.4	Outline of the Analysis . . . . .	22
<b>2</b>	<b>The CDF Detector at the Tevatron Collider</b>	<b>24</b>
2.1	The Tevatron Collider . . . . .	25
2.2	Layout of the CDF Detector . . . . .	26
2.3	The Tracking System . . . . .	28
2.4	The Solenoid Magnet . . . . .	30
2.5	The Calorimeter System . . . . .	30
2.5.1	The Central Calorimeter . . . . .	31
2.5.2	The Endwall Hadron Calorimeter . . . . .	34
2.5.3	The Plug Calorimeter . . . . .	35
2.5.4	The Forward / Backward Calorimeters . . . . .	38
2.5.5	Uninstrumented Regions in the Calorimeter . . . . .	39
2.6	The Muon Detection System . . . . .	39
2.7	The Trigger and Data Acquisition Systems . . . . .	40
<b>3</b>	<b>Measurement of the Dijet Mass Cross Section</b>	<b>43</b>
3.1	Jets and Jet Algorithms . . . . .	43
3.1.1	Jet Definition in the Cone Algorithm . . . . .	44
3.1.2	Jet 4-Vectors . . . . .	47
3.1.3	Jet Energy Corrections . . . . .	48
3.2	The Data Sample . . . . .	49

3.2.1	Event Selection . . . . .	50
3.2.2	Trigger Efficiencies . . . . .	52
3.2.3	$z$ -Vertex Cut Efficiency . . . . .	54
3.2.4	Jet Trigger Prescale Factors . . . . .	54
3.2.5	Properties of the Data Sample . . . . .	56
3.3	The Dijet Mass Distribution . . . . .	57
<b>4</b>	<b>The Unsmearing Procedure</b>	<b>63</b>
4.1	Calorimetry . . . . .	63
4.1.1	Electromagnetic Showers . . . . .	64
4.1.2	Hadronic Showers . . . . .	67
4.2	Jet Energy Smearing . . . . .	70
4.3	<i>True</i> and <i>Measured</i> Dijet Masses . . . . .	72
4.4	True Level Clustering Routines . . . . .	72
4.5	QFL Energy Scale Corrections . . . . .	75
4.6	Parameterization of the Detector Response . . . . .	76
4.7	Results of the Unsmearing Procedure . . . . .	81
4.8	Check of the Unsmearing Procedure . . . . .	83
4.8.1	Efficiencies of the Monte Carlo Samples . . . . .	84
4.8.2	True and Measured Monte Carlo Distributions . . . . .	86
4.8.3	Results of the Consistency Check . . . . .	89
<b>5</b>	<b>Systematic Uncertainties</b>	<b>92</b>
5.1	Uncertainties on the Cross Section . . . . .	92

5.1.1	Absolute Jet Energy Scale . . . . .	92
5.1.2	Relative Jet Energy Scale . . . . .	95
5.1.3	Integrated Luminosity and Trigger Normalizations . . . . .	96
5.2	Uncertainties on the Unsmearing Corrections . . . . .	97
5.2.1	Parameterization of the Detector Resolution . . . . .	97
5.2.2	Difference between the Analytic and MC Procedure . . . . .	100
5.2.3	QFL Energy Scale Corrections . . . . .	100
5.3	Combined Systematic Uncertainties . . . . .	100
<b>6</b>	<b>Results</b>	<b>103</b>
6.1	The Fully Corrected Cross Section . . . . .	103
6.2	QCD Calculations . . . . .	104
6.3	Comparison of Data and QCD . . . . .	106
6.4	$\chi^2$ Evaluation between Data and Theories . . . . .	111
6.5	Comparison of CDF and DØ Data . . . . .	115
	<b>Conclusions</b>	<b>117</b>
<b>A</b>	<b>Details of the <math>\chi^2</math> Procedure</b>	<b>119</b>
A.1	Floating Normalization of the Theory . . . . .	119
A.2	Variation of the Correlation Coefficients . . . . .	124
A.3	Summary of the $\chi^2$ Procedure . . . . .	127
<b>B</b>	<b>The CDF Collaboration</b>	<b>128</b>
	<b>Bibliography</b>	<b>133</b>

# List of Tables

1.1	The particles of the Standard Model. . . . .	4
1.2	Summary of the interactions of the Standard Model. . . . .	8
1.3	QCD subprocesses that contribute to lowest-order parton-parton scattering. . . . .	20
2.1	Summary of the calorimeter components most relevant to this analysis.	32
3.1	Measured and nominal values for prescale factors of the jet trigger bits.	56
3.2	Level 2 triggers, mass cuts, efficiencies at threshold and prescale factors.	56
5.1	The relative jet energy scale uncertainties. . . . .	96
6.1	The fully corrected dijet mass cross section and the statistical and systematic uncertainties. . . . .	104
6.2	The individual low-side systematic uncertainties in the 18 mass bins.	113
6.3	The $\chi^2$ values and the corresponding probabilities for the theories. . .	114
A.1	Values and uncertainties of a toy data set and values of a toy theory.	120

# List of Figures

1.1	Interactions in the framework of gauge field theories: A gauge boson is exchanged in between two fermions. . . . .	6
1.2	Example of parton distribution functions. . . . .	11
1.3	Higher-order corrections to interactions. . . . .	13
1.4	Schematic view of a hard proton-antiproton interaction. . . . .	17
1.5	Gluon jets in the LUND-string model. . . . .	18
1.6	Feynman diagrams for lowest-order parton-parton scattering. . . . .	21
1.7	Selected examples of higher-order Feynman diagrams that contribute to $2 \rightarrow 3$ parton-parton scattering. . . . .	23
2.1	The Tevatron collider and the system of pre-accelerators. . . . .	27
2.2	The CDF detector. . . . .	29
2.3	Schematic view of the light-collection system of the CEM. . . . .	33
2.4	The Plug Electromagnetic Calorimeter. . . . .	37
3.1	A typical dijet event at CDF. . . . .	45
3.2	Flow diagram of the JETCLU algorithm. . . . .	47
3.3	Schematic view of the dijet mass system. . . . .	51
3.4	The Run 1B jet trigger efficiencies. . . . .	53

3.5	Mass thresholds corresponding to full efficiency of the jet triggers. . . . .	54
3.6	The $z$ -vertex cut efficiencies for the individual dijet mass bins. . . . .	55
3.7	Comparison of some of the kinematic variables of our data set and the Monte Carlo events. . . . .	58
3.8	Comparison of some of the angular variables of our data set and the Monte Carlo events. . . . .	59
3.9	Scatter plot of the $\phi$ distributions of the two leading jets. . . . .	60
3.10	The partially corrected differential dijet mass cross section. . . . .	61
3.11	Fractional differences between the partially corrected data and a smooth parameterization. . . . .	62
4.1	The longitudinal shape of an electromagnetic shower. . . . .	66
4.2	The response of a detector Monte Carlo simulation to positrons. . . . .	68
4.3	The smearing of the true differential cross section. . . . .	70
4.4	Definitions of true and measured dijet masses. . . . .	73
4.5	Comparison between the two true level clustering routines. . . . .	74
4.6	Single Gaussian fits to the fractional differences between the true and measured jet $p_T$ . . . . .	77
4.7	The mean values of the Gaussian functions from the fits to the fractional differences between true and measured jet $p_T$ . . . . .	78
4.8	Detector responses to dijets with true masses of 50, 125, 250, 500, 750, and 1000 GeV/ $c^2$ , respectively. . . . .	79
4.9	Detector responses to dijets, plotted on a logarithmic scale. . . . .	80
4.10	The parameters of the detector resolution function as a function of dijet mass. . . . .	82

4.11	The unsmearing correction factor, $K$ , the ratio of smeared and true distributions, as a function of dijet mass. . . . .	83
4.12	The partially corrected differential dijet mass cross section, plotted on a doubly logarithmic scale. . . . .	84
4.13	Comparison of the smeared fit to the data. . . . .	85
4.14	The true dijet mass efficiencies of the Monte Carlo samples, used to form the full Monte Carlo distributions. . . . .	87
4.15	The measured dijet mass efficiencies of the Monte Carlo samples. . . . .	88
4.16	The full Monte Carlo distributions. . . . .	89
4.17	Comparison of the correction factors from the analytic method and the Monte Carlo method. . . . .	90
4.18	Fractional differences between the true Monte Carlo distribution and the analytically unsmearing Monte Carlo cross section. . . . .	91
5.1	The systematic uncertainties on the dijet mass cross section, due to uncertainties on the absolute energy scale. . . . .	94
5.2	Fit of a single Gaussian function to the detector response. . . . .	98
5.3	The unsmearing correction factors from the default analysis, compared to the ones obtained from the single Gaussian fit. . . . .	99
5.4	The additional corrections to the QFL energy scale and $1\text{-}\sigma$ variations of the statistical uncertainty. . . . .	101
5.5	Unsmearing corrections as a function of the dijet mass: Default analysis, QFL scale corrections $+1\sigma$ and $-1\sigma$ . . . . .	101
5.6	The systematic uncertainties on the dijet mass cross section. . . . .	102

6.1	Comparison of our data with predictions from the JETRAD Monte Carlo program (logarithmic scale). . . . .	108
6.2	Comparison of our data with predictions from the JETRAD program for different PDF's (linear scale). . . . .	109
6.3	Comparison of our data with predictions from the JETRAD program for different choices of $\mu$ (linear scale). . . . .	110
6.4	Comparison of our data with results from the DØ collaboration. . . . .	116
A.1	The total $\chi^2$ values between the data and the theoretical predictions for freely floating normalizations of the theories. . . . .	121
A.2	Graphical comparison of a toy data set with a toy theory. . . . .	122
A.3	The differences between the toy data set and the toy theory in terms of the systematic uncertainties. . . . .	123
A.4	The differences between data and theories in terms of the absolute systematic uncertainties. . . . .	125
A.5	The total $\chi^2$ as a function of the correlation coefficients. . . . .	126



# Introduction

Particle physics addresses the question, “What is the world made of?” on the most fundamental level. The beginning of particle physics can be attributed to J.J. Thompson, who discovered the electron in 1897 [1]. In 1911, E. Rutherford showed that the atom consisted of a hard core that was surrounded by a cloud of electrons [2]. When J. Chadwick discovered the neutron in 1932 [3], the most important questions about the structure of matter seemed to have been answered. However, one year later, C.D. Anderson established the existence of the positron [4], the first antiparticle postulated by P.A.M. Dirac. Subsequently, the muon [5] and the neutrino [6] were discovered, and by the late 1950’s an inexplicable number of other particles (hadrons) were found.

In 1964, M. Gell-Mann [7] and G. Zweig [8] independently proposed that hadrons were built up from even ‘more elementary’ particles, which Gell-Mann called quarks. The Standard Model of elementary particle physics was developed. According to the Standard Model, all matter (and antimatter) consists of six quarks, six leptons and their respective antiparticles. The fundamental interactions between particles (with the exception of gravity) are described in terms of the exchange of gauge bosons. Despite several open questions, the Standard Model is the most promising theory available to describe nature, a notion that received important further support by the discovery of the gauge bosons of the weak interaction at CERN in 1983 [9] and the discovery of the top quark at Fermilab in 1994 [10, 11].

While the Standard Model describes the electromagnetic and the weak interactions

very successfully, the theory of the strong interaction, the interaction that binds quarks inside the nucleons and nucleons inside the nuclei, still remains partly a mystery. The best candidate for a theory of the strong interactions is the theory of Quantum Chromodynamics (QCD). However, due to the nature of QCD, accurate quantitative predictions are extremely difficult to obtain and QCD calculations still rely on semi-phenomenological models and a variety of assumptions.

A characteristic feature of QCD is the occurrence of collimated bunches of hadronic particles, called *jets*. In this thesis, we measure the cross section for the production of two or more jets as a function of the dijet mass at a center-of-mass energy of 1.8 TeV, currently the highest in the world. This large centre-of-mass energy allows the production of extremely massive dijets with masses of up to  $1 \text{ TeV}/c^2$ . The measured dijet mass distribution spans six order of magnitude and provides an excellent testing ground for comparisons with QCD calculations, as well as testing our understanding of jet dynamics. This measurement is particularly interesting in light of the recent CDF measurements of the inclusive transverse jet energy distribution [12] and the total transverse jet energy [13]. Both observed an excess in the data over QCD predictions at high jet energies.

This dissertation is organized as follows: Chapter 1 provides a short theoretical introduction; the Standard Model is introduced, the theory of the strong interactions is discussed and the analysis method is outlined. Chapter 2 gives an overview of the CDF detector and discusses the aspects of the detector that are relevant to this analysis. The data selection, the experimental jet-finding method and the measurement of the dijet mass cross section is explained in Chapter 3. The unsmearing procedure, which enables us to compare our data to QCD predictions, is the topic of Chapter 4. The systematic uncertainties on our measurement are discussed in Chapter 5 and the results are presented in Chapter 6. A summary and outlook concludes this thesis.

# Chapter 1

## Theoretical Introduction

### 1.1 The Standard Model: An Overview

The properties of all elementary particles and the details of their interactions, with the exception of gravity, are described by the Standard Model. Particles in the Standard Model are considered to be elementary in the sense that they do not exhibit any observable spatial structure and are therefore, classically speaking, point-like. Elementary particles are divided into two groups, half-integer-spin particles, called fermions, and integer-spin particles, called bosons. While fermions provide the building blocks of matter, interactions between particles are mediated by bosons.

#### 1.1.1 Matter

Fermions exist in two different types, leptons and quarks, the main difference being that leptons do not couple to the strong interactions (see below). The Standard Model contains six leptons, six quarks and their respective antiparticles. The six leptons are the electron ( $e$ ), the muon ( $\mu$ ), the tau ( $\tau$ ) and their neutrino counterparts ( $\nu_e, \nu_\mu$  and  $\nu_\tau$ ). The six quark flavours are called up, down, charm, strange, top and bottom ( $u, d, c, s, t$  and  $b$ ). There are three generations of leptons, each generation

containing one lepton doublet and one quark doublet. Except for differences in the masses, nothing seems to further distinguish between the three generations. Leptons and antileptons are assigned the lepton numbers  $+1$  and  $-1$ , respectively. The number of leptons is conserved so that leptons and antileptons can only be created and destroyed in pairs. Furthermore, no transition from one lepton generation to another has been observed experimentally to date. This is referred to as the generation-wise conservation of lepton number. Similarly, the baryon number is a conserved quantity, with quarks and antiquarks being assigned the baryon numbers  $+1/3$  and  $-1/3$ , respectively. Table 1.1 lists the particles of the Standard Model.

Generation	Quarks	Charge	Leptons	Charge
1	up $u$	$2/3$	electron-neutrino $\nu_e$	0
	down $d$	$-1/3$	electron $e$	$-1$
2	charm $c$	$2/3$	muon-neutrino $\nu_\mu$	0
	strange $s$	$-1/3$	muon $\mu$	$-1$
3	top $t$	$2/3$	tau-neutrino $\nu_\tau$	0
	bottom $b$	$-1/3$	tau $\tau$	$-1$

Table 1.1: The particles of the Standard Model.

In the naive quark-parton model [14], quarks and antiquarks are the fundamental building blocks of matter from which all strongly interacting particles, *hadrons*, are built up. Hadrons are subdivided into two classes, *mesons* and *baryons*.

Mesons are bound systems consisting of a quark ( $q$ ) and an antiquark ( $\bar{q}$ ) with a total spin of either 0 or 1; they are bosons. Like any other quantum mechanical bound system, mesons have a discrete energy level spectrum, corresponding to the different modes of  $q\bar{q}$  excitation, e.g. rotations or vibrations. A typical example of a meson is the positive pion ( $\pi^+$ ), a combination of  $u$  and  $\bar{d}$  quarks.

Baryons are three-quark systems, consisting of either three quarks ( $qqq$ ) or three antiquarks ( $\bar{q}\bar{q}\bar{q}$ ). They carry a total spin of either  $1/2$  or  $3/2$  and are fermions. Examples of baryons are the proton ( $uud$ ) and the neutron ( $udd$ ). Each baryon (antibaryon) carries the baryon number  $+1$  ( $-1$ ).

### 1.1.2 Forces

The three fundamental interactions within the Standard Model, the electromagnetic, the weak and the strong interactions, are described by a special class of theories, called gauge field theories. In a gauge field theory, the Lagrangian of an interaction is required to be invariant under local gauge transformations. The local invariance of the theory is ensured by requiring that the 4-potential of the interaction transforms in an appropriate way. In other words, changes in the 4-potential compensate for local gauge changes, resulting in an invariant Lagrangian. The full Lagrangian can be obtained by imposing local gauge invariance, Lorentz invariance, invariance under space inversion and time reversal, and renormalizability on the theory [15]. A theory is said to be renormalizable if the various unphysical infinite contributions, that typically arise in quantum field theories, can all be consistently eliminated.

By regarding classical fields as operators and by setting up canonical commutation relations for them, the theory can be quantized. In a quantized gauge theory the quantized states of the 4-potential are associated with the mediators of the interaction, the gauge bosons, and the interaction is described in terms of an exchange of gauge bosons between fermions, see Fig. 1.1. While all known gauge bosons are spin-1 particles, their properties depend on the nature of the underlying gauge theory.

#### The Electromagnetic Interaction

The prototypical and most accurate quantum gauge theory is the theory of Quantum Electrodynamics (QED), which describes the electromagnetic interaction. The gauge

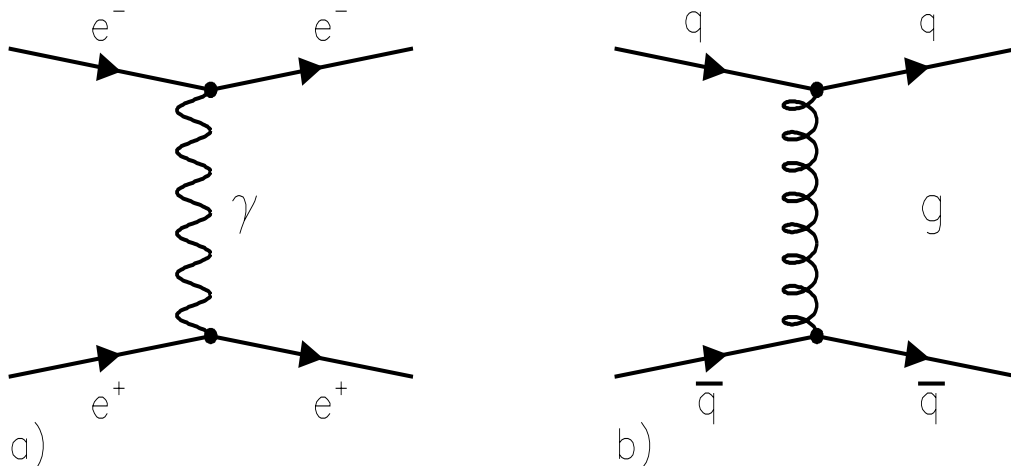


Figure 1.1: Interactions in the framework of gauge field theories: A gauge boson is exchanged in between two interacting fermions. a) Electromagnetic interaction: A photon is exchanged between an electron and a positron. b) Strong interactions: A gluon is exchanged in between two quarks.

boson associated with the electromagnetic force is the photon. Because of the infinite range of the electromagnetic field, the photon is massless. Quantum Electrodynamics is locally invariant under the following local gauge transformation [16]

$$\Psi(x) \rightarrow e^{ie\Lambda(x)} \Psi(x) \quad (1.1)$$

$$A_\mu(x) \rightarrow A_\mu(x) + \partial\Lambda(x)/\partial x_\mu, \quad (1.2)$$

with the electron field,  $\Psi(x)$ , the photon field,  $A_\mu$ , the electron charge,  $e$ , and the arbitrary gauge parameter,  $\Lambda(x)$ . The phase factor,  $e^{ie\Lambda(x)}$ , belongs to the group  $U(1)$ , the unitary group in one dimension and QED is called a  $U(1)$  theory. Since  $U(1)$  transformations are commutative, QED is an Abelian gauge theory. The photon field plays a crucial role, for without it, there could be no local gauge invariance.

The extremely high accuracy with which QED predicted, for instance, the anomalous magnetic moment of the electron encouraged attempts to find other possible symmetry groups that would provide the basis of a more general description of the

fundamental forces in terms of gauge theories.

### The Weak Interactions

The weak interactions take place between all quarks and leptons. They lie behind processes like the nuclear beta decay, which allows protons to turn into neutrons and vice versa. Weak forces are vital for the synthesis of heavy elements in the early universe and for the fusion power cycles in stars. They are so feeble that they are usually swamped by the much stronger electromagnetic and strong interactions. The weak interactions are mediated by massive vector bosons,  $W^\pm$  and  $Z^0$ , in analogy with photon exchange in electromagnetic interactions.

### The Glashow-Salam-Weinberg Model of the Electroweak Interaction

The electromagnetic and the weak interactions were unified in the 1960's by Glashow, Salam and Weinberg [17] with their  $SU(2)\times U(1)$  electroweak model. In order to describe the weak interactions, they chose a  $SU(2)$  symmetry<sup>1</sup> with the three gauge bosons,  $W^+$ ,  $W^-$  and  $W^0$ , corresponding to the three generators of the group  $SU(2)$ . To be able to describe both interactions with one theory, an additional symmetry,  $U(1)$ , had to be introduced with the corresponding gauge boson  $Y^0$ . The two observable neutral gauge bosons of the theory, the photon and the  $Z^0$ , cannot be directly associated with the  $W^0$  and the  $Y^0$ . Instead, they are quantum mechanical superpositions of the two with the electroweak mixing or Weinberg angle,  $\theta_W$ , which determines the degree of mixing between the two parts of the theory.

The short-range nature of the weak interaction requires the gauge bosons to be massive. However, the presence of mass terms in the Lagrangian spoils the local gauge invariance of the theory. The introduction of massive gauge bosons, while preserving the invariance of the theory, is possible through the process of spontaneous symmetry

---

<sup>1</sup> $SU(2)$  denotes the special unitary group in two dimensions, where 'special' means that the determinants of the matrices that generate the group are +1.

breaking [18] or Higgs mechanism. The Higgs mechanism requires the presence of (at least) one more boson, the Higgs boson. Whereas the masses of the electroweak gauge bosons are predicted by the theory, the mass of the Higgs boson is a free parameter and can be determined only experimentally. After the discovery of the weak gauge bosons and the top quark, the question of the existence and mass(es) of the Higgs boson(s) is one of the most important outstanding issues in particle physics today.

### The Strong Interactions

Analogous to the electromagnetic and the weak interactions, the strong interactions can be described by using a group-theoretical approach. Introducing the *colour* quantum number and eight gauge bosons, called gluons, the strong interactions can be described in terms of a SU(3) local gauge symmetry. This theory is known as Quantum Chromodynamics (QCD). Since this thesis directly compares experimental data with predictions from QCD, the features of this theory are described in more detail in the next section. Table 1.2 summarizes the interactions of the Standard Model.

Force	Gauge Boson(s)	Symmetry	acts on	Example
electromagnetic	photon	U(1)	quarks, $e, \mu, \tau$	atomic binding
weak	$W^+, W^-, Z^0$	SU(2)	all fermions	$\beta$ -decay
strong	8 gluons	SU(3)	quarks	nuclear binding

Table 1.2: Summary of the interactions of the Standard Model.

## 1.2 Quantum Chromodynamics and Jets

In this section the theory of the strong interactions, Quantum Chromodynamics, is introduced. Whereas the electromagnetic and the weak forces are well-described

by the  $SU(2)\times U(1)$  electroweak model, QCD provides a less complete picture of the strong interactions, due to its non-perturbative nature. A characteristic feature of QCD is the occurrence of collimated bunches of hadronic particles, called *jets*.

### 1.2.1 The Static Quark Model

During the 1960's, when large amounts of data on baryon and meson resonances were accumulated, regularities or patterns were noted among these hadron states. In 1964, M. Gell-Mann and G. Zweig showed that the regularities could be accounted for by postulating three types of fermion constituents in a baryon, which Gell-Mann called quarks<sup>2</sup>. These quark types or flavours were called  $u$  (for up),  $d$  (for down) and  $s$  (for strange). However, this simple model failed when used to classify the  $\Delta^{++}$  baryon resonance. The  $\Delta^{++}$  was thought to be made up of three  $u$  quarks, which all had to be in the same spin state (spin-up), thereby violating the Pauli exclusion principle [20], which states that no two fermions in a single system can carry identical quantum numbers. In order to resolve this conflict, a new charge, called *colour*, was introduced. The colour charge is the source of interquark forces, just as electric charge is the source of electromagnetic forces between charged particles. It was postulated that each quark exists in three different colours, red, green and blue and that baryons and mesons are colour singlets. Mesons are built up of quark-antiquark combinations, with the antiquark carrying the anticolour of the quark and the three quarks in a baryon carry one colour each, adding up to zero net colour charge. Subsequently, it turned out that this additional degree of freedom was necessary for other reasons as well.

---

<sup>2</sup>Gell-Mann took this term from James Joyce's novel *Finnegans Wake*. In Gell-Mann's own words: 'In 1963, when I assigned the name "quark" to the fundamental constituents of the nucleon, I had the sound first, without the spelling, which could have been "kwork". Then, in one of my occasional perusals of *Finnegans Wake*, by James Joyce, I came across the word "quark" in the phrase "Three quarks for Muster Mark". ... From time to time, phrases occur in the book that are partially determined by calls for drinks at the bar. I argued, therefore, that perhaps one of the multiple sources of the cry "Three quarks for Muster Mark" might be "Three quarts for Mister Mark," in which case the pronunciation "kwork" would not be totally unjustified. In any case, the number three fitted perfectly the way quarks occur in nature.' [19]. The term originally used by Zweig was *aces*.

### 1.2.2 The Quark-Parton Model

A dynamical (rather than static) understanding of the structure of hadrons has its origin in 1968, when data from deep-inelastic lepton-nucleon scattering led to the development of the quark-parton model. Data from inelastic scattering showed an approximate independence of the total cross section on the energy of the neutrino. This *scaling* behavior was first predicted by Bjorken [21] and is commonly referred to as *Bjorken scaling*. The interpretation of scaling is that the neutrino interacts with point-like constituents inside the nucleon, called *partons*, a term introduced by Feynman. In the quark-parton model, hadrons are composed of many partons. Protons, for example, are composed of three *valence quarks* ( $uud$ ) and a number of virtual partons into which it constantly dissociates. These virtual constituents can either be gluons or virtual quark-antiquark pairs (*sea quarks*). The lifetimes,  $\tau_{virt}$ , of the virtual partons are limited by the Heisenberg uncertainty principle [22], according to which  $\tau_{virt} \approx \hbar/\Delta E$ , with the energy difference,  $\Delta E$ , between the hadron and the virtual state. In the quark-parton model, partons inside hadrons are massless and move collinearly with their parent hadron.

Suppose that  $f_i(x_i)$  is the probability for finding a parton,  $i$ , inside the hadron with a certain fraction,  $x_i$ , of the total hadron momentum. The inclusive cross section is then given by the cross section for scattering off the parton times  $f_i(x_i)dx$ , summed over all partons  $i$  and integrated over  $dx$ . The parton distributions are empirically determined from deep inelastic scattering data, in which electrons or neutrinos are scattered off hadrons. There are several competing parameterizations of the parton distribution functions (PDF). A typical example of the distributions for valence  $u$ -quarks, valence  $d$ -quarks and gluons, as a function of  $x$ , are shown in Fig. 1.2 [16].

The identification of the partons with quarks lead to the expectation that the parton distribution function integrals

$$\int_0^1 [u(x) + \bar{u}(x) + d(x) + \bar{d}(x) + s(x) + \bar{s}(x)]x dx \approx 1, \quad (1.3)$$

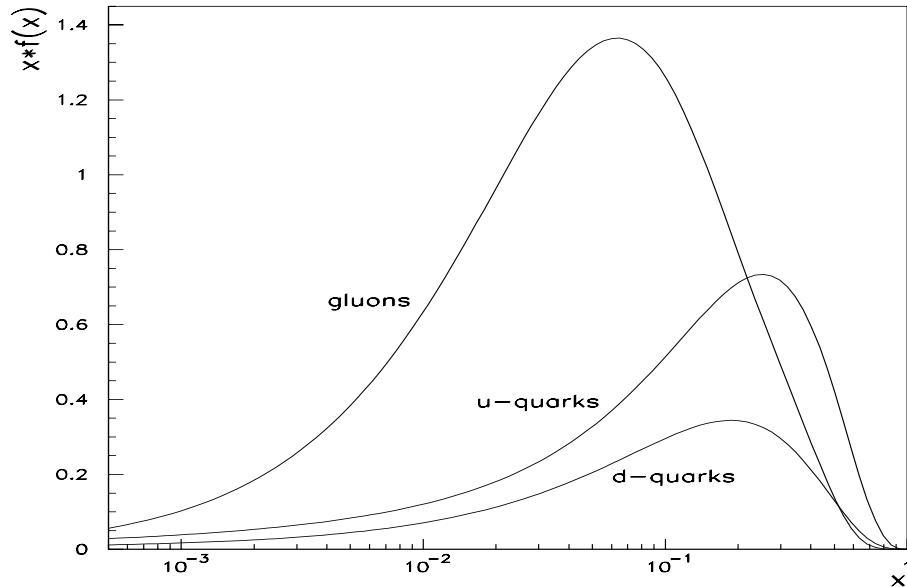


Figure 1.2: A typical example of parameterizations of the parton distribution functions. Shown are the distributions for valence  $u$ -quarks, valence  $d$ -quarks and gluons.

since the total fractional momentum summed over all constituents is necessarily unity. However, in 1972, fits to deep inelastic scattering data resulted in a value for this sum of only about 0.5 [23]. This was a first indication that gluons had a real dynamical meaning, since the remaining half of the proton momentum had to be carried by neutral constituents, the gluons, which themselves participated in the scattering process.

One year later, deviations from the scaling behavior of the parton distribution functions in muon scattering experiments were observed at Fermilab [24]. These *scaling violations* could not be explained with the parton model. A new theory of the strong interactions, called Quantum Chromodynamics, was developed.

### 1.2.3 QCD and the Running Coupling Constant

Quantum Chromodynamics [25] is regarded as the fundamental theory of the strong interactions, the interactions between quarks and gluons. It associates the colour charge, introduced to explain the  $\Delta^{++}$ , with the charge of the strong interaction, and identifies the neutral particles, discovered as 'missing momentum' in deep inelastic

scattering, with the gluons. Finally, QCD takes the dynamical properties of the gluons correctly into account to explain, for instance, the observation of scaling violations.

The theory of QCD is a non-Abelian gauge theory, based on the  $SU(3)$  colour symmetry and eight corresponding gauge bosons, the gluons. Quarks carry a colour charge (red, green or blue) and antiquarks carry a corresponding anticolour (antired, anti-green or antiblue). They are held together by the exchange of gluons, which carry two labels, one colour and one anticolour. A quark can change its colour by emitting a gluon with the appropriate colour-anticolour combination. Only coloured particles can emit or absorb gluons. Leptons and the other gauge bosons are colourless and do therefore not interact strongly.

Since no coloured particles were observed experimentally it was postulated that only colourless combinations of quarks and antiquarks were allowed. The simplest colourless configurations of quarks are (i) quark-antiquark combinations (one colour and one anticolour) and (ii) three quarks or three antiquarks (one of each colour or anticolour). These are exactly the valence-quark combinations that describe the known baryons and mesons. The impossibility to observe colour is one of the main characteristics of the strong interactions. It arises naturally within the framework of a  $SU(3)$  gauge theory.

When calculating the cross section for a certain interaction, the picture of a simple exchange of a gauge boson, as in Fig. 1.1, yields only the approximate, lowest-order solution. In principle one has to include processes of higher orders as well, for instance a process in which the exchanged photon fluctuates into an  $e^+e^-$ -pair, see Fig. 1.3.

These higher-order terms generally lead to divergences (infinite values) of the cross section if integrated over all possible momentum transfers. In order to obtain physically meaningful (finite) results, the theory must be *renormalized*. This is done by a special, but arbitrary, prescription that introduces a new dimensional scale, the renormalization scale,  $\mu$ . Renormalization procedures with different values of  $\mu$  all have to lead to the same observable amplitudes, a fact that is expressed by the Renormal-

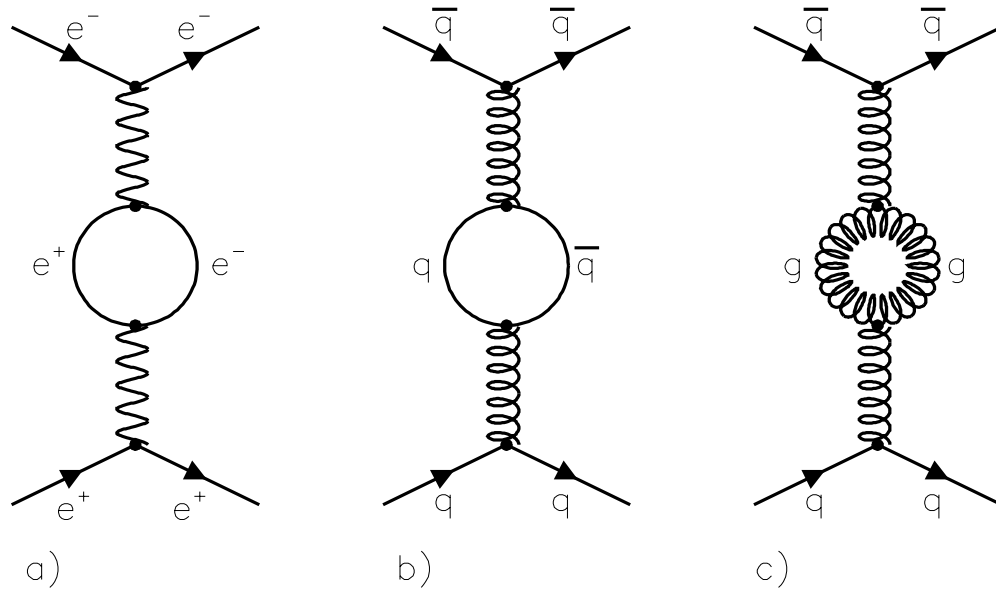


Figure 1.3: Higher-order corrections to interactions. a)  $e^+e^-$ -loop correction to the exchange of a photon. b)  $q\bar{q}$ -loop correction to the exchange of a gluon. c) Gluon self-interaction term.

ization Group Equations. In practice, however, amplitudes can only be calculated in perturbation series of the interaction's coupling strength. Since the number of possible diagrams and the complexity of the calculations involved rise dramatically with the order of the calculation, the series has to be truncated and amplitudes depend, however slightly, on the value of  $\mu$ .

The coupling strength of an interaction is determined by the charge of the particles associated with it. Higher-order processes in the calculations lead to a dependence of the strength of the interaction with the negative square of the 4-momentum transfer,  $Q^2$ . It turns out that, despite the similarities between QED and QCD, the  $Q^2$ -evolution of their coupling constants is fundamentally different. Due to the non-Abelian nature of QCD the gluons carry colour charges themselves, giving rise to a QCD Lagrangian that contains gluon self-interaction terms. This is in sharp contrast to QED, where the photon is electrically neutral and does not couple to itself, a fact that is reflected by the Abelian nature of the U(1) symmetry.

In the case of QED vacuum polarization, the production of virtual electron-positron pairs (Fig. 1.3a)) that surround the electron, leads to a screening of the electron's charge. The strength of the electromagnetic interaction therefore decreases with larger distances (corresponding to smaller  $Q^2$  values) from the electron.

In the case of QCD three effects contribute to vacuum polarization. The production of virtual quark-antiquark pairs result in a screening of the colour charges of the quarks, similar to the QED effect, see Fig. 1.3b). This effect is dependent of the number of quark flavours,  $n_f$ . Two additional effects from the production of virtual gluon pairs result in an anti-screening of the colour charge of the quark (Fig. 1.3c)) [26]. Taking all these effects into account, the effective QCD coupling strength,  $\alpha_s(Q^2)$ , is given to the order  $\mathcal{O}(\alpha_s^2)$  by [27]

$$\alpha_s(Q^2) = \frac{12\pi}{(33 - 2n_f) \ln \frac{Q^2}{\Lambda_{QCD}^2}}, \quad (1.4)$$

with

$$\Lambda_{QCD}^2 = \mu^2 \exp \left( \frac{-12\pi}{(33 - 2n_f) \alpha_s(\mu^2)} \right). \quad (1.5)$$

The parameter  $\Lambda_{QCD}$  is to be determined by experiment. The theory is applicable only for  $Q^2 \gg \Lambda_{QCD}^2$ , for which the values of  $\alpha_s$  are small, so that perturbation theory can be applied. Since  $n_f$  is assumed to be six, the strong coupling constant  $\alpha_s(Q^2)$  decreases with increasing  $Q^2$ . At sufficiently high values of  $Q^2$ ,  $\alpha_s$  gets arbitrarily small. This is called the *asymptotic freedom* [28] of the strong interactions. The value of  $\alpha_s$  is usually quoted at a  $Q^2$  equal to the square of the mass,  $M_Z$ , of the  $Z$  boson. The current world average value is [29]

$$\alpha_s(M_Z^2) = 0.119 \pm 0.002. \quad (1.6)$$

The decrease of the coupling strength with  $Q^2$  implies that the colour forces increase with the distance between quarks. It is impossible to completely separate two quarks

because their potential energy is proportional to the distance between them. Once the energy is large enough, a quark-antiquark pair (a meson) is created from the vacuum. This phenomena is called *colour confinement*. Despite the absence of an analytic proof, due to the complicated mathematical structure of QCD, the concept of colour confinement is widely accepted since no coloured objects have been observed.

### 1.2.4 Evolution Equations for the Parton Densities

Because of their colour charge, gluons can be radiated off other gluons or quarks before and after an interaction. These gluon bremsstrahlung processes introduce an explicit non-scaling  $Q^2$ -dependence to the parton distribution functions. The  $Q^2$ -evolution of the quark densities is described by the Altarelli-Parisi evolution equations [30]. The quark evolution can be written as integro-differential equations for the quark densities  $f(x, Q^2)$  [27]:

$$\frac{df(x, Q^2)}{d \log Q^2} = \frac{\alpha_s}{2\pi} \int_x^1 \frac{dy}{y} f(y, Q^2) P_{qq} \left( \frac{x}{y} \right). \quad (1.7)$$

The equations express the fact that a quark with momentum fraction  $x$  could have originated from a parent quark with a larger momentum fraction  $y$  that has radiated a gluon. The probability that this happens is proportional to  $\alpha_s P_{qq}(x/y)$ , where the *splitting function*

$$P_{qq}(z) = \frac{4}{3} \left( \frac{1+z^2}{1-z} \right) \quad (1.8)$$

represents the probability of a quark emitting a gluon and so becoming a quark with momentum reduced by a fraction  $z = x/y$ .

Equation (1.7) holds for valence quarks in the nucleon. The evolution of the sea quarks is given by an analogous equation with a second term added, because the gluons can transform into  $q\bar{q}$  pairs.

Given the quark structure functions at some reference point  $f(x, Q_0^2)$ , they can be calculated at any value of  $Q^2$  using the so called DGLAP (Dokshitzer-Gribov-Lipatov-

Altarelli-Parisi) equations [30, 31, 32].

### 1.2.5 Jets in $p\bar{p}$ Collisions

A direct consequence of the concept of colour confinement is the occurrence of jets of hadronic particles. The first evidence for multiple production of hadrons in nucleon-nucleon scattering dates back to 1950 [33]. Quark-jets were first observed in 1975 by the Mark-I Collaboration at SLAC [34]; four years later, experiments at the PETRA collider at DESY reported the first evidence for gluon jets [35]. The first jets in  $p\bar{p}$  collisions were observed by the UA2 Collaboration at CERN in 1982 [36].

The production of jets in proton-antiproton collisions can be understood with the help of Fig. 1.4, which shows a schematic view of a hard  $p\bar{p}$  interaction. The collision is seen as the interaction of a single parton,  $i$ , inside the proton with a single parton,  $j$ , inside the antiproton. The remaining partons, called *spectator partons*, do not participate in the interaction. The collision causes the proton and antiproton to disintegrate. The nucleon remnants disappear down the beam pipe and are usually not detected. The resulting hadrons, some of which decay further into lighter hadrons, are observed in the detector. Since the transverse momenta of the partons are independent of the energy of the parent hadron, one expects, at sufficiently high energies, the occurrence of *jets*, bunches of hadronic particles, which all move in a similar direction. By analyzing the characteristics of jets, one can gain insight into the kinematics and the properties of the underlying partons. Since quarks and gluons can be observed only indirectly through jets, the analysis of jets is a powerful tool to study the strong interaction and to test the predictions of QCD.

### 1.2.6 Jet Fragmentation

The development of quarks and gluons into a hadronic final state, the hadronization or jet fragmentation process, typically occurs at energies of a few GeV [37]. Because

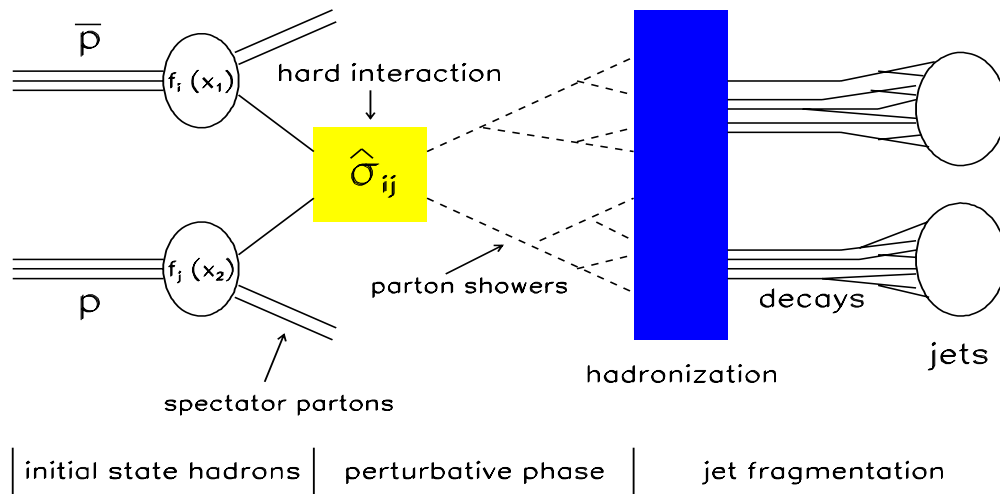


Figure 1.4: Schematic view of a hard proton-antiproton interaction.

of the  $(\ln Q^2)^{-1}$  behaviour of the strong coupling constant, perturbative methods can not be employed. Instead, one has to rely on semi-empirical models that approximate the process of jet fragmentation. Two examples of such models are the Feynman-Field independent fragmentation model [38] and the LUND-string model [39]. Since the latter is used in the Monte Carlo program that was employed in this analysis, it is briefly described here.

In the LUND-string model, the fragmentation does not depend on the nature of the underlying scattering process but follows a general model. When a colour-neutral  $q\bar{q}$  pair is created in a collision, a colour force field is created between them. For a confining theory like QCD the colour lines of force are mostly concentrated in a narrow tube connecting  $q$  with  $\bar{q}$ , acting like a string with a constant tension,  $k$  (independent of the separation,  $r$ , between  $q$  and  $\bar{q}$ ). Observed relations between the angular momenta and the energies of light hadronic states indicate a potential of the form [40]

$$V = kr, \quad (1.9)$$

with a value of  $k \approx 1 \text{ GeV/fm}$  [16]. The colour tube is treated dynamically as a massless, relativistic string. If the two ends of the string (the two quarks) are separated,

the potential energy between  $q$  and  $\bar{q}$  rises linearly with  $r$  and the string breaks as soon as sufficient energy for the production of a hadron is available. This process is repeated until the invariant string mass is too low to produce any more hadrons.

Gluons are described in the LUND model as kinks in the colour string. The string is suspended in between the gluon and the quarks, running from  $q$  to  $g$  to  $\bar{q}$ , see Fig. 1.5a). Instead of attaching massless particles at the ends of the string, a massless gluon is now attached to a point in the middle. A breaking of the string results in two chains of mesons, similar to what one would get from two  $q\bar{q}$  strings, except that one of the mesons includes a piece from both segments. Whereas the  $q\bar{q}$  string results in two back-to-back-jets, the resulting hadron distributions from the  $q\bar{q}g$  system are distributed around the direction of the original gluon, giving rise to a third jet, as shown in Fig. 1.5b).

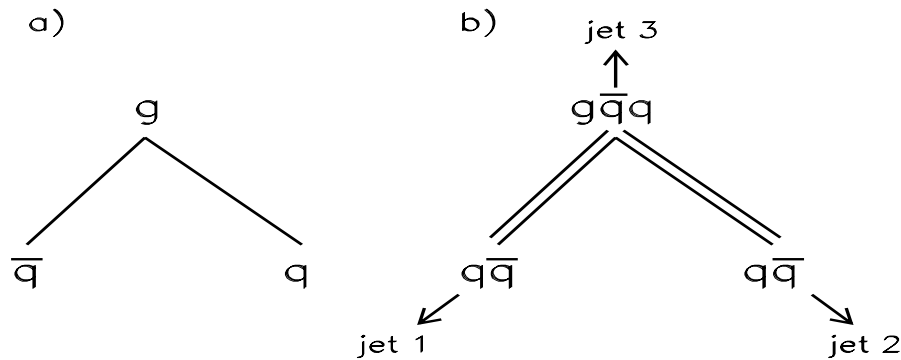


Figure 1.5: Gluon jets in the LUND-string model.

### 1.3 The Dijet Mass Cross Section

Most interactions in  $p\bar{p}$  collisions are due to soft processes and their cross sections cannot be calculated from first principles. Only in selected kinematic regions can one observe the hard scattering of the underlying partons and compare experimental observations with perturbative QCD calculations. A parton-parton scattering results, to lowest order, in four jets, two from scattered partons and two from the remnants

of the broken-up nucleons. The latter, called *spectator jets*, are lost in the beam pipe and are ignored in this analysis. The term *dijet* in this analysis refers to the two jets that arise from the scattered partons. When these two jets hit the calorimeter they are opposite in azimuth and their experimental signature is a very large energy deposition in a localized region of the calorimeter. To lowest order, they have equal transverse energies,  $E_T = E \sin \theta$ , where  $E$  is the energy of the jet and  $\theta$  is the polar angle, with respect to the direction of the incoming proton.

### 1.3.1 Leading Order QCD Subprocesses

When discussing the parton-parton scattering process of the form  $AB \rightarrow CD$  it is convenient to introduce the following Lorentz-invariant (Mandelstam) variables [27]:

$$\begin{aligned}\hat{s} &= (p_A + p_B)^2, \\ \hat{t} &= (p_A - p_C)^2, \\ \hat{u} &= (p_A - p_D)^2,\end{aligned}\tag{1.10}$$

where  $p_A$  and  $p_B$  are the 4-momenta of the incoming partons and  $p_C$  and  $p_D$  are those of the scattered partons. The subprocess centre-of-mass energy squared,  $\hat{s}$ , is related to the centre of mass energy squared,  $s$ , according to

$$\hat{s} = sx_p x_{\bar{p}},\tag{1.11}$$

where  $x_p$  and  $x_{\bar{p}}$  are the momentum fractions of the interacting partons inside the proton and antiproton, respectively, that take part in the scattering process.

The leading order  $2 \rightarrow 2$  scattering subprocesses are listed in Table 1.3 [16]. Their cross sections are of the form

$$\frac{d\hat{\sigma}}{d\hat{t}}(AB \rightarrow CD) = \frac{|\mathcal{M}|^2}{16\pi\hat{s}}.\tag{1.12}$$

The transition matrix element,  $\mathcal{M}$ , can be calculated from Feynman rules for quark and gluon propagators and vertices in QCD [15]. The lowest-order Feynman diagrams that contribute to the cross section are shown in Fig. 1.6.

Subprocess	$ \mathcal{M} ^2 / (16\pi^2\alpha_s^2)$	$ \mathcal{M}(90^\circ) ^2 / (16\pi^2\alpha_s^2)$
$q_i q_j \rightarrow q_i q_j$	$\frac{4}{9} \frac{\hat{s}^2 + \hat{u}^2}{\hat{t}^2}$	2.2
$q_i \bar{q}_j \rightarrow q_i \bar{q}_j$		
$q_i q_i \rightarrow q_i q_i$	$\frac{4}{9} \left( \frac{\hat{s}^2 + \hat{u}^2}{\hat{t}^2} + \frac{\hat{s}^2 + \hat{t}^2}{\hat{u}^2} \right) - \frac{8}{27} \frac{\hat{s}^2}{\hat{u}\hat{t}}$	3.3
$q_i \bar{q}_i \rightarrow q_i \bar{q}_i$	$\frac{4}{9} \frac{\hat{t}^2 + \hat{u}^2}{\hat{s}^2}$	0.2
$q_i \bar{q}_i \rightarrow q_j \bar{q}_j$	$\frac{4}{9} \left( \frac{\hat{s}^2 + \hat{u}^2}{\hat{t}^2} + \frac{\hat{t}^2 + \hat{u}^2}{\hat{s}^2} \right) - \frac{8}{27} \frac{\hat{u}^2}{\hat{s}\hat{t}}$	2.6
$q_i \bar{q}_i \rightarrow gg$	$\frac{32}{27} \frac{\hat{u}^2 + \hat{t}^2}{\hat{u}\hat{t}} - \frac{8}{3} \frac{\hat{u}^2 + \hat{t}^2}{\hat{s}^2}$	1.0
$gg \rightarrow q_i \bar{q}_i$	$\frac{1}{6} \frac{\hat{u}^2 + \hat{t}^2}{\hat{u}\hat{t}} - \frac{3}{8} \frac{\hat{u}^2 + \hat{t}^2}{\hat{s}^2}$	0.1
$q_i g \rightarrow q_i g$	$\frac{\hat{s}^2 + \hat{u}^2}{\hat{t}^2} - \frac{4}{9} \frac{\hat{s}^2 + \hat{u}^2}{\hat{u}\hat{s}}$	6.1
$gg \rightarrow gg$	$\frac{9}{4} \left( \frac{\hat{s}^2 + \hat{u}^2}{\hat{t}^2} + \frac{\hat{s}^2 + \hat{t}^2}{\hat{u}^2} + \frac{\hat{u}^2 + \hat{t}^2}{\hat{s}^2} + 3 \right)$	30.4

Table 1.3: QCD subprocesses that contribute to lowest-order parton-parton scattering and the corresponding matrix elements squared, i.e. averaged over spin and colour (from [16]).

Another quantity that influences the two-jet production cross section are the parton distribution functions,  $f_i(x)$ , which were introduced in Section 1.2.2. With these ingredients the two-jet production cross section can be written as [41]

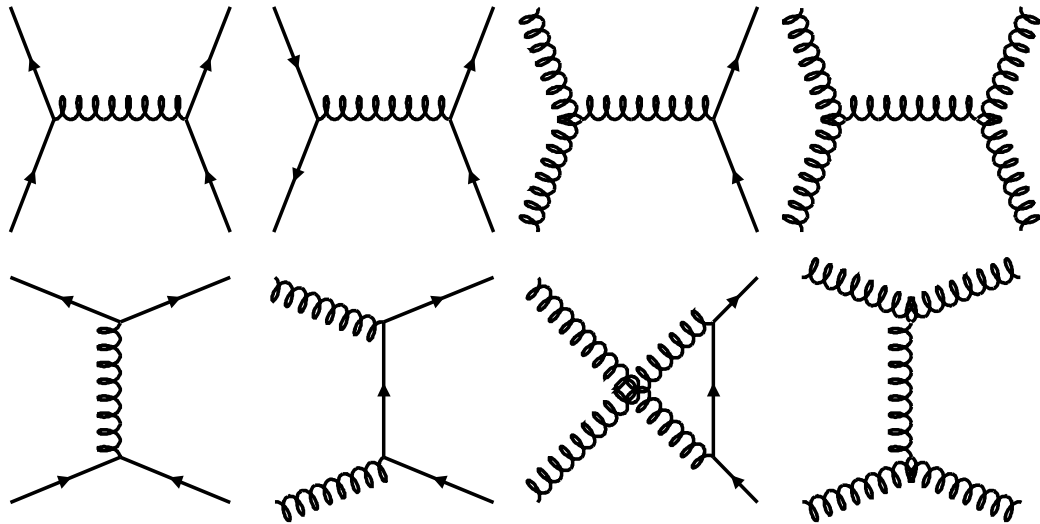


Figure 1.6: Feynman diagrams for lowest-order parton-parton scattering.

$$\frac{d^3\sigma}{dy_3 dy_4 dp_T^2} = \frac{1}{16\pi\hat{s}^2} \sum_{A,B,C,D=q,\bar{q},g} \frac{f_A(x_1, \mu^2)}{x_1} \frac{f_B(x_2, \mu^2)}{x_2} \times \overline{\sum} |\mathcal{M}(AB \rightarrow CD)|^2 \frac{1}{1 + \delta_{CD}}, \quad (1.13)$$

where  $p_T = p \sin \theta$  is the transverse jet momentum, the Kronecker delta,  $\delta_{CD}$ , gives an additional factor of  $\frac{1}{2}$  to identical final state partons, since they are summed twice, and  $y_3$  and  $y_4$  are the rapidities of the final state partons, with

$$y = \frac{1}{2} \ln \left( \frac{E + p_z}{E - p_z} \right), \quad (1.14)$$

where  $p_z = p \cos \theta$  is the longitudinal jet momentum.

Based on this description, a few simple characteristic features of the dijet mass cross section can be derived. First, from Table 1.3 we can see that the largest contributions to two-jet production stem from the elastic scattering processes ( $gg \rightarrow gg$ ). Second, the two-jet production cross section is directly proportional to the parton distribution functions. Since gluons dominate the parton distributions at low  $x$  (see Fig. 1.2) we

expect, at low dijet masses, the cross section to be dominated by gluon-gluon scattering. As we move towards higher  $x$ , quark-quark scattering becomes more important, since the valence quarks dominate the parton distribution at high  $x$ . Third, the two-jet production cross section is inversely proportional to the subprocess cross section  $\hat{s}^2 \equiv M_{jj}^2$ , where  $M_{jj}$  is the dijet invariant mass, defined as

$$M_{jj} = \sqrt{(E_1 + E_2)^2 - (\vec{p}_1 + \vec{p}_2)^2}. \quad (1.15)$$

We therefore expect a falling shape of the dijet mass distribution. At high  $x$ , corresponding to high dijet masses, the falloff of the parton distribution functions leads to a steeper falling dijet mass cross section.

### 1.3.2 Higher-Order QCD Processes

Higher-order QCD processes result in more complicated configurations of partons. Quarks and gluons can radiate off gluons before and after the hard scattering process. This is referred to as *initial state* and *final state radiation*. The probability of these higher-order processes is proportional to the strong coupling constant  $\alpha_s$ . In the  $Q^2$ -range of the CDF data, the value of  $\alpha_s$  is around 0.1, so that processes of the order  $n$  are suppressed by  $n$  orders of magnitude. Figure 1.7 shows selected examples of higher-order Feynman diagrams that contribute to  $2 \rightarrow 3$  parton-parton scattering.

## 1.4 Outline of the Analysis

In this thesis we measure the differential dijet mass cross section,  $d\sigma/dM_{jj}$ , with the dijet mass as defined in Eqn. (1.15), using the two *leading jets*, i.e. the two jets with the highest transverse energies in an event.

Because we compare our data to next-to-leading order QCD calculations, which include processes that result in 3-jet events, we measure the *inclusive* dijet mass cross

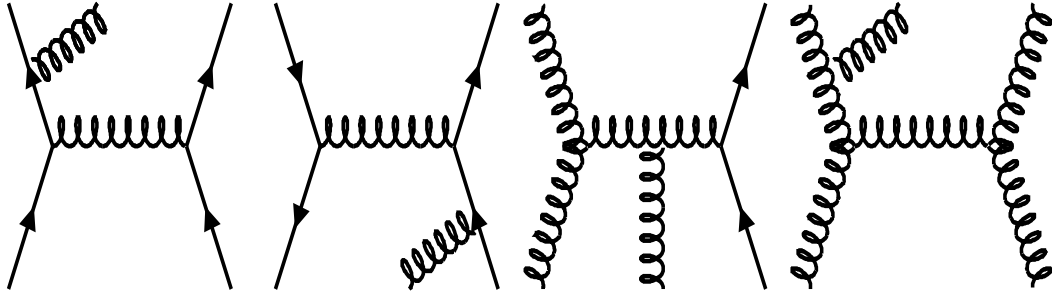


Figure 1.7: Selected examples of higher-order Feynman diagrams that contribute to  $2 \rightarrow 3$  parton-parton scattering.

section. That means we do not restrict ourselves to events with exactly two jets but include events with any number of jets in our analysis. In other words, we examine events with two or more jets and count the number of these events as a function of the dijet mass.

The fully corrected dijet mass cross section is measured in two steps. In the first step we measure what we refer to as the *partly corrected* cross section. The partly corrected cross section is based on data that are corrected for calorimeter response effects (non-linearity and non-uniformity of response of the calorimeter), trigger efficiencies and data selection cut efficiencies. The second step involves the correction of the data for detector resolution effects, which result in a measured cross section that is different from the true cross section. We then compare the fully corrected dijet mass cross section with predictions from next-to-leading order QCD calculations. This analysis probes regions of dijet masses, higher than any previous experiment. The importance of comparing the shape and normalization of the measurements to QCD predictions is of particular interest as any significant deviation may signal the presence of new physics.

## Chapter 2

# The CDF Detector at the Tevatron Collider

The experimental apparatus used in this study is located at the Fermi National Accelerator Laboratory (Fermilab) in Batavia, Illinois. Fermilab was founded in December 1968. Today, more than 2200 scientists from 20 countries work on numerous particle physics experiments on the 28 km<sup>2</sup> site, situated about 65 kilometers west of Chicago. Fermilab's main accelerator, the Tevatron, produces proton-antiproton collisions at a centre-of-mass energy of 1.8 TeV, the highest available world wide today.

The system of particle accelerators that is used to accelerate and collide the protons and antiprotons, culminating in the Tevatron, is briefly described in Section 2.1. The observation and analysis of these collisions involves the use of a multipurpose particle detector, the Collider Detector at Fermilab (CDF). Section 2.2 introduces the overall layout of the CDF detector and sections 2.3 through 2.7 describe its main components. Emphasis is placed upon the system of calorimeters, the part of the detector most relevant to this analysis.

## 2.1 The Tevatron Collider

In the fall of 1985, the Tevatron  $p\bar{p}$  collider came into operation. The Tevatron [42] is a synchrotron with a circumference of 6.3 km that accelerates protons and antiprotons to energies of 900 GeV, corresponding to a centre-of-mass energy of  $\sqrt{s} = 1.8$  TeV. They collide in two interaction regions, where the two particle detectors, CDF and DØ, are installed to record the products of the  $p\bar{p}$  interactions. The Tevatron tunnel has an inner diameter of 3 m and is situated 6 m underground.

Before protons and antiprotons reach their nominal Tevatron energies, a set of pre-accelerators is used as an injection system. A Cockcroft-Walton pulsed ion source provides the first stage of acceleration, during which electrons are added to hydrogen atoms and the resulting negative ions are accelerated to an energy of 750 keV. The 150 m-long Linear Accelerator (Linac) accelerates the  $H^-$  ions further to 400 MeV before injecting them into the Booster accelerator. During the injection, both electrons are stripped from the  $H^-$  ions by passing them through a carbon foil. The Booster is an alternating gradient synchrotron with a diameter of about 150 m. It accelerates the resulting protons to energies of 8 GeV and loads twelve bunches of protons into the Main Ring. In the Main Ring, a synchrotron that is housed in the same tunnel as the Tevatron, the protons are accelerated to energies of around 150 GeV before they are injected into the Tevatron for the final stage of the acceleration process. In the Tevatron, which is located directly below the Main Ring, the protons reach their final energy of 900 GeV. To keep protons and antiprotons on a circular orbit, the Tevatron is equipped with 774 superconducting dipole magnets. The magnet coils produce a magnetic field of 4.4 T and consist of superconducting niobium-titanium (Nb-Ti) filaments embedded in copper. Liquid helium is used to cool them to their operating temperature of 5 K.

A counter-rotating beam of antiprotons is produced by using 120-GeV protons that are extracted from the Main Ring and strike a 7-cm-thick nickel or copper target [43]. The antiprotons are then directed into the Debuncher, a ring with a circumference

of 520 m, where they are stochastically cooled [44], before they are transferred to the Accumulator, a ring that is concentric with the Debuncher, for storage and further cooling. Once enough antiprotons are accumulated they are injected into the Main Ring, accelerated to 150 GeV and transferred into the Tevatron, where they are, in counter-rotation to the protons, accelerated to their final energy of 900 GeV.

The Tevatron operates with bunches of protons and antiprotons. During Run I, instantaneous luminosities in excess of  $2 \cdot 10^{31} \text{cm}^{-2} \text{sec}^{-1}$  were achieved with six bunches of protons and antiprotons. Each proton and antiproton bunch consisted of about  $2 \cdot 10^{11}$  and  $6 \cdot 10^{10}$  particles, respectively [45]. The corresponding time between consecutive bunches was  $3.5 \mu\text{s}$ . Figure 2.1 shows the Tevatron collider and the system of pre-accelerators.

## 2.2 Layout of the CDF Detector

The CDF detector is a multipurpose detector, designed to measure the momenta, energies, scattering angles, and, where possible, determine the identities of the particles produced in Tevatron  $p\bar{p}$  collisions. Event analysis is based on charged particle tracking, magnetic momentum analysis, fine-grained calorimetry and muon detection. The total weight of the detector is about 5000 t. The CDF collaboration consists of over 450 physicists from 47 institutions.

The calorimeter system covers the detector pseudorapidity region of  $|\eta_d| < 4.2$ , while covering the full range of the azimuthal angle,  $\phi$ . It has approximately uniform granularity in  $\eta_d$  and  $\phi$ . The central tracking chambers measure charged particle momenta in the range  $21^\circ < \theta < 159^\circ$ . The momenta of charged particles are analyzed in a 1.4 T solenoidal magnetic field. Muon coverage is provided by drift chambers in the region  $|\eta_d| < 1$  and by large forward toroid systems in the region  $1.96 < |\eta_d| < 3.64$ . The approximately 140 000 detector channels are read out by a custom front-end electronics system, followed by a large Fastbus network. Data acquisition is handled

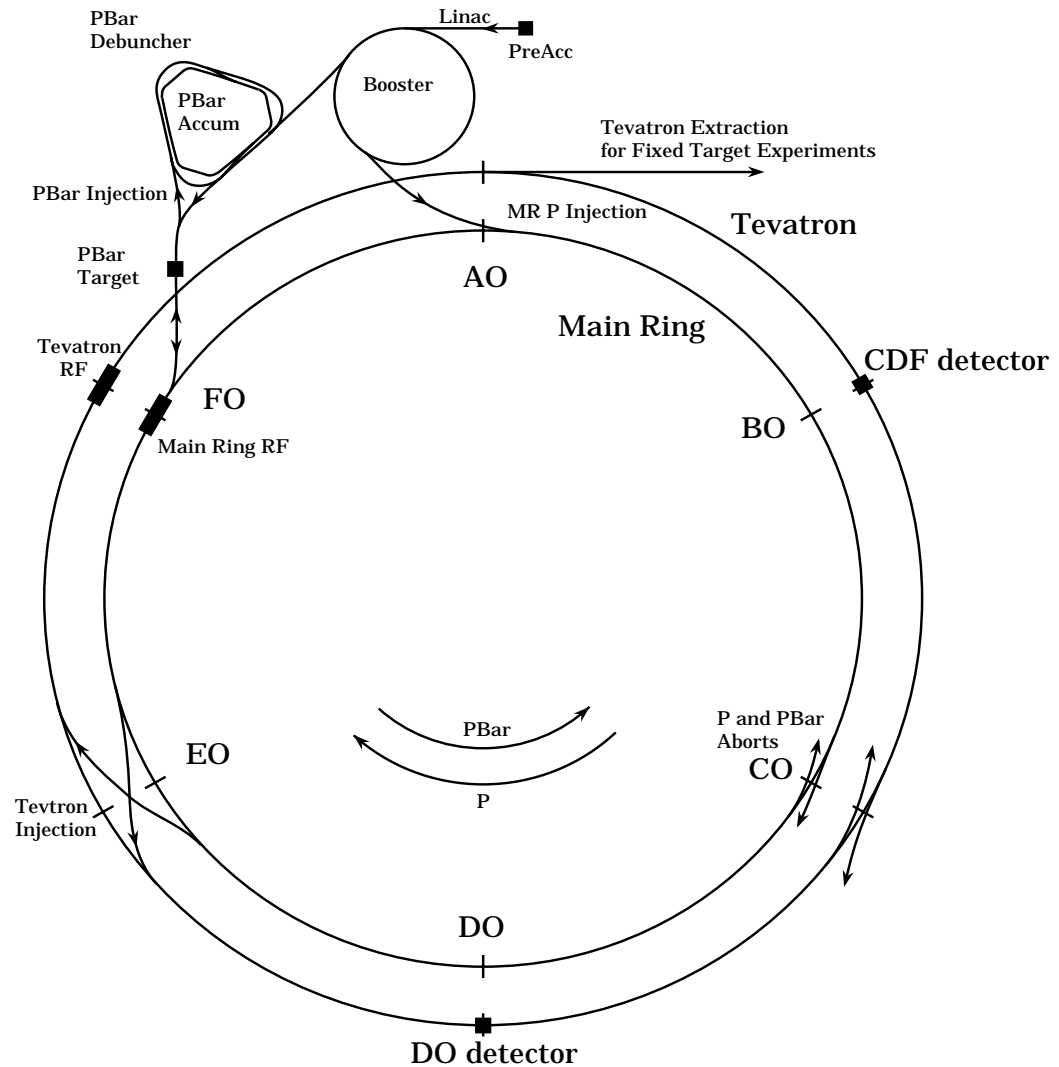


Figure 2.1: The Tevatron collider and the system of pre-accelerators.

by a three level trigger system.

The overall layout is as follows. The detector consists of a 2000 t movable central detector and two identical forward/backward detectors. The central detector is made up of the tracking chambers, the solenoidal magnet, the steel yoke, electromagnetic and hadronic calorimeters, and muon chambers. The forward/backward detectors consist of electromagnetic and hadronic calorimeters, and steel toroidal magnets, used as muon spectrometers. Single layers of scintillation counters in front of the electromagnetic shower counters serve as luminosity monitors and 'minimum bias'

triggers. Figure 2.2 shows perspective views of the CDF detector.

The CDF coordinate system is right-handed, with the origin defined to be in the centre of the detector. The  $x$  axis points radially outwards in the plane of the Tevatron, the  $y$  axis points upward, and the  $z$  axis points along the direction of the protons. The pseudorapidity is defined according to

$$\eta = -\ln \left( \tan \frac{\theta}{2} \right). \quad (2.1)$$

In the following, we distinguish between the physics pseudorapidity,  $\eta$ , and the detector pseudorapidity,  $\eta_d$ . Whereas the measured  $z$  vertex is used for the determination of  $\eta$ , a  $z$  vertex of zero is assumed for  $\eta_d$ . The two quantities are equal for interactions occurring at  $z = 0$  and they differ by about  $\pm 0.2$  for  $z = \pm 60$  cm.

Starting from the interaction point (vertex), a description of the detector components is given below. For the present analysis the central, endwall, and plug calorimeters are of special importance. These parts of the detector are therefore described in more detail. For a comprehensive description of the CDF detector, see [46, 47] and references therein.

## 2.3 The Tracking System

Within the magnetic field of the solenoid there are three separate tracking systems for charged particles, the silicon vertex detector, a vertex drift chamber and the central tracking chamber.

Immediately surrounding the beam pipe is a four-layer silicon microstrip vertex detector (SVX') [48], a radiation-hard version of the SVX that was installed in 1993. The SVX' consists of two identical 51 cm-long cylindrical modules that meet at  $z = 0$ . The four layers of the SVX' are at distances of 2.9, 4.2, 5.7, and 7.9 cm from the beamline, respectively. Axial microstrips provide precision track reconstruction with

Figure 2.2: Perspective view of the CDF detector along the beam axis (upper picture).  
Schematic side view of one quadrant of the CDF detector (lower picture).

a single-hit reconstruction of  $13\ \mu\text{m}$  and an impact parameter resolution of  $17\ \mu\text{m}$ .

Outside the SVX' is a set of vertex drift chambers (VTX) that provide tracking information up to a radius of 22 cm. The VTX measures tracks used to reconstruct the vertices of  $p\bar{p}$  interactions with a precision of 1 mm in the  $z$  direction.

Both the SVX' and the VTX are mounted inside the central tracking chamber (CTC) [49]. The CTC is a 3.2, m-long drift chamber with an outer radius of 132 cm, covering the  $\eta_d$ -region  $-1 < \eta_d < 1$ . It contains 6156 sense wires in 84 cylindrical layers, grouped into nine 'superlayers'. Five of these superlayers have wires parallel to the beam direction (axial wires) and provide tracking in the  $r - \phi$  plane. The four remaining superlayers are tilted by  $\pm 3^\circ$  with respect to the beam direction (stereo wires) and, together with the axial wires, provide tracking information in the  $r - z$  plane. The two-track resolution of the CTC was measured to be 3.5 mm, the spatial resolution is better than  $200\ \mu\text{m}$  in  $r - \phi$  and 6 mm in  $z$ .

## 2.4 The Solenoid Magnet

In order to obtain precise momentum determination for charged particles that are produced in the central region, the CTC is immersed in a uniform 1.4 T magnetic field along the beam direction. The field is produced by a 3 m-diameter, 5 m-long superconducting solenoidal coil. The coil is made of 1164 turns of a NbTi/Cu superconductor, cooled with liquid helium. The overall thickness of the coil and cryostat is 0.85 radiation lengths.

## 2.5 The Calorimeter System

The CDF calorimeter system consists of four sections, the central, endwall, plug, and forward calorimeters, covering the range of  $|\eta_d| < 4.2$  and the full azimuthal range. In this analysis, the central, endwall, and plug calorimeters were used to measure

the energies and directions of the jets, whereas the forward calorimeter was used for background rejection only.

All CDF calorimeters are constructed with a projective tower geometry to measure the energy flow in fine bins of pseudorapidity and azimuthal angle. The term 'projective' indicates that the towers point towards the nominal interaction point. By measuring the energy deposited by a particle in a projective tower, the angle with which it emerged from the vertex is measured simultaneously. In the central, plug, and forward regions, each tower consists of an electromagnetic section in front of a hadronic section. Although some hadronic energy is deposited in the electromagnetic section, comparisons of electromagnetic and hadronic energies can be made on a tower-by-tower basis. The calorimeters are made up of approximately 5000 towers. Their height is about 0.1 units in  $\eta_d$  and their width ranges from 5 to  $15^\circ$  in  $\phi$ .

All CDF calorimeters are sampling calorimeters, which, as opposed to total absorption calorimeters, only sample a fraction of the energy deposited by an incoming particle. Two types of sampling calorimeters are employed at CDF. While the central and end-wall calorimeters have scintillator sampling, the plug and the forward calorimeters are gas based. Scintillator calorimeters were chosen for the low- $|\eta_d|$  region because of their good energy resolution, due to their larger sampling fraction, compared to gas calorimeters. In the more forward region of the detector energy resolution becomes less critical. At the same time, a finer transverse segmentation is needed to realize the same spatial resolution as in the central calorimeter. In addition, the high multiplicities in the forward region would age scintillator too quickly. As a result, all CDF calorimeters in the region  $|\eta_d| > 1.2$  are gas based. Table 2.1 gives a summary of the properties of the central, the endwall and the plug calorimeters.

### 2.5.1 The Central Calorimeter

The solenoid is surrounded by the central calorimeter. It consists of 48 wedge-shaped modules, assembled into four self-supporting arches that rest on the yoke box. The

	Central		Endwall	Plug	
	EM	Hadron	Hadron	EM	Hadron
$ \eta_d $ coverage	0 - 1.1	0 - 0.9	0.7 - 1.3	1.1 - 2.4	1.3 - 2.4
Tower size, $\Delta\eta_d \times \Delta\phi$	$\approx 0.1 \times 15^\circ$		$\approx 0.11 \times 15^\circ$	$\approx 0.09 \times 5^\circ$	
Active medium	polystyrene scintillator	acrylic scintillator	acrylic scintillator	Proportional tube chambers	
Scintillator thickness or tube size [cm]	0.5	1.0	1.0	0.7 x 0.7	1.4 x 0.8
Number of layers	31	32	15	34	20
Absorber	Pb	Fe	Fe	Pb	Fe
Absorber thickness [cm]	0.32	2.5	5.1	0.27	5.1
Energy resolution at 50 GeV	2%	11%	14%	4%	20%
Position resolution at 50 GeV [cm <sup>2</sup> ]	0.2 x 0.2	10 x 5	10 x 5	0.2 x 0.2	2 x 2

Table 2.1: A summary of the calorimeter components most relevant to this analysis.

arches join together in pairs to provide complete azimuthal coverage. The central calorimeter is composed of an electromagnetic and a hadronic section.

### Central Electromagnetic Calorimeter

The Central Electromagnetic Calorimeter (CEM) [50] covers the region  $|\eta_d| < 1.1$ . It uses a hybrid design with scintillator/absorber sandwiches for energy measurement and an embedded strip chamber for position determination and longitudinal shower development. The hybrid design combines the good energy resolution of scintillator with the high spatial resolution of a gas strip chamber.

The basic layout of one of the CEM wedges is shown in Figure 2.3. The innermost part of the CEM is an 1.4 mm-thick aluminum base plate, located at a distance of

173 cm from the beamline. Electromagnetic shower measurement is performed by using 31 layers of 5 mm-thick SCSN-38 polystyrene scintillator. The individual pieces of scintillator are wrapped in two layers of vellum drawing paper. Interleaved with the scintillator are 30 layers of 0.3 mm lead, clad on both sides with 0.4 mm aluminum. The pieces are assembled to form ten projective towers, each covering 0.1 units in  $\eta_d$  and  $15^\circ$  in  $\phi$ . Each side of the tower is covered with a 1.9 mm-thick cover plate. The gap in between the steel cover plates and the scintillator/absorber sandwiches are filled with wavelength shifters that collect the light emitted by the scintillator. Two photomultiplier tubes per tower, one on either side, read out the signal.

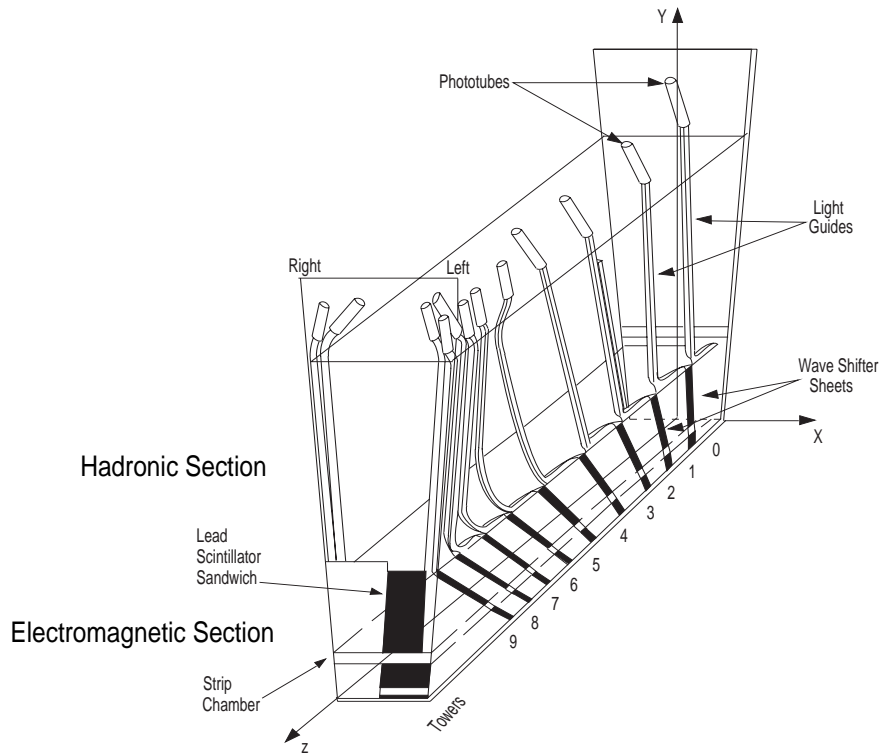


Figure 2.3: Schematic view of the light-collection system of the CEM. The hadronic section is located directly on top of the electromagnetic section.

The CEM modules were initially calibrated with a 50 GeV electron test beam. The electron energy resolution for electrons between 10 and 100 GeV was measured to be  $\sigma/E_T = 13.5\%/\sqrt{E_T} \oplus 2\%$ , where  $E_T$  is the transverse energy of the electrons in GeV and the symbol  $\oplus$  indicates that the independent contributions are added in

quadrature.

The strip chambers are located near the shower maximum, between the fifth and the sixth scintillator layers. High voltage wires are strung orthogonally to the strips, which are made of copper-backed 1.6 mm PC boards. The chambers determine shower position and transverse development by measuring the charge deposition on the strips and wires.

### Central Hadronic Calorimeter

The Central Hadronic Calorimeter (CHA) [51], a pure sampling calorimeter without strip chambers, covers the range  $|\eta_d| < 0.9$ . It consists of 32 layers of 2.5 cm-thick steel and 1 cm-thick PMMA-based scintillator, mounted on the outside of the CEM. The tower structure of the CHA matches that of the CEM, i.e. there is a one-to-one correspondence between the CEM and the CHA towers. Analogous to the CEM, the light signal from the scintillator is collected by wavelength-shifters on either side of the tower and read out by photomultiplier tubes.

Initial calibration of the CHA modules was done with a test beam of 50 GeV pions. No deviation from linearity of response was observed for pions that were minimum ionizing in the CEM, in the energy range between 10 and 150 GeV. The energy resolution of the CHA was found to be  $\sigma/E_T = 75\%/\sqrt{E_T} \oplus 3\%$ . Calibration maintenance is performed by using a pulsed laser system. Laser calibration results can be compared with those of a separate calibration check done with a  $^{137}\text{Cs}$  source.

### 2.5.2 The Endwall Hadron Calorimeter

The Endwall Hadron Calorimeter (WHA) [51] fills the gap between the central and plug calorimeters. The towers of the WHA and the CHA combine to form a single hadron calorimeter. The WHA covers the pseudorapidity region  $0.7 < |\eta_d| < 1.3$  and consists of a hadronic section only. There are two separate wall calorimeters,

one in either  $z$  direction from the interaction point. Each of the wall calorimeters is azimuthally arranged in 24 separate modules that are mated to the corresponding CHA wedges. The WHA towers are arranged in a projective geometry. Their size is  $0.11 \times 15^\circ$  ( $\Delta\eta_d \times \Delta\phi$ ).

Like the Central Hadron Calorimeter, the Wall Hadron Calorimeter is a pure steel-scintillator sampling calorimeter with layers of 1 cm-thick acrylic scintillator. The WHA consists of 15 layers of 5.1 cm-thick steel. The signal collection technique is essentially the same as for the CHA.

The WHA was calibrated together with the CHA modules. The resolution of the WHA for pions was measured to be  $\sigma/E_T = 105\%/\sqrt{E_T} \oplus 5\%$ . Compared to the CHA, the energy-dependant term is larger by about a factor of  $\sqrt{2}$ , a value that is expected from the lower sampling fraction, due to the thicker absorber plates of the WHA.

### 2.5.3 The Plug Calorimeter

The plug calorimeter extends the calorimeter coverage down to  $10^\circ$ . As mentioned in Section 2.5, the plug is a gas calorimeter, with the active medium being a mixture of 50% argon, 50% ethane and a small amount of alcohol. The plug consists of two identical calorimeters that are located in the ends of the solenoid, at  $z = \pm 173$  cm.

#### Plug Electromagnetic Calorimeter

The two Plug Electromagnetic Calorimeters (PEM) [52] cover the regions  $1.2 < \eta_d < 2.4$  and  $-2.4 < \eta_d < -1.2$ , respectively. They are cylindrical in shape and are made up of four  $90^\circ$  quadrants. The projective towers cover  $5^\circ$  in  $\phi$  and there are 16 towers segmented in  $\eta_d$ . The first tower, at  $|\eta_d| = 2.4$ , is of size 0.09 in units of  $\eta_d$ , the next four towers are only half that size, and the remaining eleven towers are of size 0.09 again. The four smaller rows of towers were usually combined offline to form two

standard sets of towers.

The PEM is a sandwich of lead and gas filled proportional tube layers, arranged in cylindrically symmetric volumes on either side of the interaction region. Four quadrants share the same gas volume. Each proportional layer is constructed from proportional tubes. Each proportional tube consists of gold plated tungsten wires, centered in a resistive plastic tube, see Fig. 2.4a). The tubes have a cross section of  $0.7 \times 0.7 \text{ cm}^2$  and span the length of a quadrant. Each plane of tubes is assembled into a fan-shaped quadrant in azimuth, with the tubes arranged perpendicularly to the beam. To construct a proportional layer, the planes were sandwiched by a pair of 1.6 mm-thick copper clad G-10 panels, as pictured in Fig. 2.4b). The wires are the anodes and the copper clad panels are the cathodes. On one side of the panel, the copper is subdivided into pads. Copper traces on the opposite side of that panel carry the signal to the edge of the quadrant. Summing up the signals longitudinally yields the tower signal. The longitudinal depth of the PEM is 34 proportional layers, each 1.2 cm thick, interleaved with 33 layers of 0.27 cm-thick lead. The front of the PEM is covered with a 1.3 cm-thick steel plate, which acts as first absorber layer. Similarly, the rear is covered with a 4.5 cm-thick steel plate, acting as the first absorber layer of the Plug Hadronic Calorimeter.

All towers of the PEM were calibrated with a 100 GeV electron beam. The energy resolution for electrons in the range from 20 to 200 GeV was measured to be  $\sigma/E_T = 28\%/\sqrt{E_T} \oplus 2\%$  and the response of the PEM was found to be linear (as a function of the incident particle energy) within 3%.

### **Plug Hadronic Calorimeter**

The Plug Hadronic Calorimeter (PHA) covers the region  $1.2 < |\eta_d| < 2.4$ . It is arranged in twelve  $30^\circ$  sectors. The towers cover 0.09 units in  $\eta_d$  and  $5^\circ$  in  $\phi$ .

The PHA is a sandwich of gas filled proportional tube layers and steel. The construction of the proportional layers is similar to the PEM. Gold plated tungsten wires,

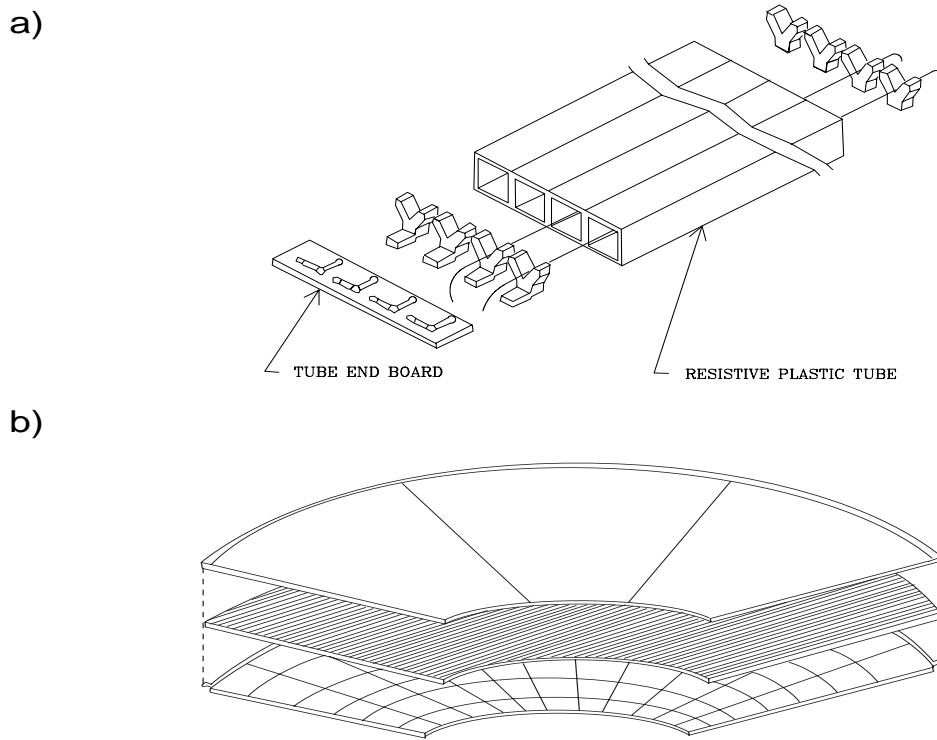


Figure 2.4: The Plug Electromagnetic Calorimeter. a) Proportional tubes, plastic anodes, and wire supports. b) Proportional layer. The plane of proportional tubes is sandwiched by G-10 panels.

centered in resistive plastic tubes with a cross section of  $0.8 \times 1.4 \text{ cm}^2$ , act as anodes. The cathode planes consist of 72 electrically distinct pads on the inner side, which are connected to the outer side via a through hole. Copper traces on the outer side carry the signals to the edge of the wedges, from where they are transmitted to front end amplifiers in the collision hall. The 20 proportional chambers are sandwiched with 21 steel plates, each 5.1 cm thick<sup>1</sup>.

The PHA sectors were calibrated with 200 GeV pions. No deviation from linearity was observed for the response to pions between 20 and 200 GeV. The energy resolution for pions in this energy range was measured to be  $\sigma/E_T = 90\%/\sqrt{E_T} \oplus 4\%$ .

<sup>1</sup>The plate after the fourth proportional layer has a thickness of 6.4 cm.

### 2.5.4 The Forward / Backward Calorimeters

The Forward / Backward Calorimeters complete the coverage of the CDF calorimeters, extending the range to  $|\eta_d| < 4.2$ . The two identical calorimeters are box shaped and are located 6.5 m from the interaction point in either  $z$  direction. In this study, the Forward / Backward Calorimeters were used for the rejection of the background only. The following description applies to the Forward Calorimeter. The Backward calorimeter is located at the opposite side of the interaction region.

#### Forward Electromagnetic Calorimeter

The Forward Electromagnetic Calorimeter (FEM) covers the region  $2.3 < \eta_d < 4.2$ . It is a sandwich of gas filled proportional chambers and lead. It is azimuthally arranged in four  $90^\circ$  quadrants. The projective towers cover 0.1 units in  $\eta_d$  and  $5^\circ$  in  $\phi$ . There are 19 divisions in  $\eta_d$ . Thirty proportional layers are interleaved with layers of lead. Pad signals are read out in two longitudinal depth segments. The FEM quadrants were calibrated with electrons. The response was found to be linear for electrons in the energy range 20 to 160 GeV and the energy resolution was measured to be  $\sigma/E_T = 25\%/\sqrt{E_T} \oplus 2\%$ .

#### Forward Hadronic Calorimeter

The Forward Hadronic Calorimeter (FHA) [53] covers the region  $2.3 < \eta_d < 4.2$ . Like the FEM it is a sandwich of gas filled proportional chambers and steel, azimuthally arranged in four  $90^\circ$  quadrants. The 19 projective towers cover 0.1 units in  $\eta_d$  and  $5^\circ$  in  $\phi$ . Twenty-seven proportional layers are sandwiched with 27 layers of steel. The tube dimensions are 50% larger than the ones of the FEM and there is no longitudinal depth segmentation. The FHA was calibrated with pion beams. The response was found to be linear for pions from 40 to 200 GeV and the pion energy resolution was measured to be  $\sigma/E_T = 130\%/\sqrt{E_T} \oplus 4\%$ .

### 2.5.5 Uninstrumented Regions in the Calorimeter

Mechanical constraints in the design of the calorimeter necessarily result in uninstrumented regions or *cracks*. Measured quantities, such as the transverse energies of jets, have to be corrected for the effects of these cracks.

Of particular importance for this analysis are the two  $\theta$  cracks [54]. At  $\theta = 90^\circ$  (at  $z = 0$ ) the CEM modules are bounded by 2.5 cm steel endplates that are separated from the scintillator/absorber stack by a 1.6 cm support gap. The steel endplates of the east and west modules that are joined at  $z = 0$  are separated by an air gap of about 0.5 cm. This crack will be referred to as the  $90^\circ$  crack. At  $\theta = 38^\circ$ , the CEM wedges are bounded by a 5.1 cm steel plate, separated from the stack by a 5.1 cm gap that is occupied by the light guides. This is called the  $30^\circ$  crack. The effects of the cracks on the jet energies will be discussed in Section 3.1.3.

## 2.6 The Muon Detection System

Compared to the electron, the muon has a much higher mass, resulting in a cross section for losses due to radiation that is significantly smaller. This ability of the muon to penetrate matter motivates the location of the muon subsystems in the outer region of the CDF detector. The material between the interaction region and the muon detection system, primarily the calorimeters, filters out the majority of electrons and hadrons before they reach the muon detectors. There are two separate systems to measure muons at CDF.

In the central region, the Central Muon Detector (CMU) [55] covers the region  $|\eta_d| < 0.65$  and is located on the outer edge of the central hadronic calorimeter, 3.47 m from the beam axis. The CMU is made up of  $12.6^\circ$  wedges with four layers of rectangular drift cells. The Central Muon Upgrade detector (CMP) [56], installed in 1992 to reduce false muon background from hadrons that punch through the calorimeter, surrounds the central region of the CDF detector with 630 t of additional steel. Its active

planes consist of four layers of single-wire drift tubes. The Central Muon Extension (CMX), consisting of 1536 proportional drift cells, provides additional pseudorapidity acceptance in the region  $0.65 < |\eta_d| < 1$ .

The forward / backward muon system [57] consist of one spectrometer in both regions, each containing two 1 m-thick steel toroids with outer and inner diameters of 7.8 m and 0.9 m, respectively. Four coils excite the toroid to a magnetic field ranging from 1.6 T (inner radius) to 2.0 T (outer radius). Three layers of drift chambers measure the muon trajectory and two layers of scintillation counters provide trigger information. The  $\eta_d$  range covered by these spectrometers is  $1.96 < |\eta_d| < 3.64$ .

## 2.7 The Trigger and Data Acquisition Systems

During Run I, the Tevatron collider operated with a proton-antiproton bunch-crossing time of  $3.5 \mu\text{s}$ , corresponding to a bunch-crossing frequency of 286 kHz. The maximum rate at which CDF events could be written to tape was approximately 10 Hz. This necessitated a trigger system that was capable of handling the  $p\bar{p}$  interaction rate and at the same time selecting interesting physics events with a reduction factor of almost 30 000 : 1. A system of three consecutive trigger levels [58] was used where each level reduced the data rate transferred to the next-higher level, thereby providing time for a more sophisticated analysis of the events.

Trigger Level 1 required less than the bunch crossing time of  $3.5 \mu\text{s}$  to pass on an event to the next-higher level. It primarily used information from the calorimeters and the muon systems. To use the calorimeter component of the Level 1 trigger, the calorimeters were logically segmented into 'trigger towers', covering ranges of  $\Delta\phi = 15^\circ$  and  $\Delta\eta_d = 0.2$ . To pass the Level 1 calorimeter trigger, an individual trigger tower was required to have an energy of 8 GeV in the central electromagnetic calorimeter, 11 GeV in the central hadronic calorimeter, 11 GeV in the plug electromagnetic calorimeter or 51 GeV in either the plug hadronic or one of the forward calorimeters [59]. At

an instantaneous luminosity of  $\mathcal{L} = 5 \cdot 10^{30} \text{cm}^{-2}\text{s}^{-1}$ , the Level 1 acceptance rate was approximately 1 kHz [47].

The Level 2 trigger required about  $15 \mu\text{s}$  to make a decision about a potential event. With this increased processing time, simple calculations could be performed, essentially using the same information as in Level 1. Level 2 performed transverse energy clustering by applying 'seed' and 'shoulder' thresholds to all trigger towers. Seeds were formed if a trigger tower exceeded an energy of 3 GeV in any single electromagnetic or hadronic calorimeter tower. A nearest-neighbour jet algorithm then searched for energies of more than 1 GeV in any of the four neighbouring towers. If so, the tower was included in the cluster. This process continued until no more contiguous towers were found. The energies of all towers were then summed to give the energy of the cluster. The Run 1B data sample was collected with four jet triggers with threshold energies of 20, 50, 70 and 100 GeV, respectively. These triggers are referred to as the Jet 20, 50, 70 and 100 triggers. The jet trigger required at least one jet with a trigger Level 2 transverse energy that was greater than the  $E_T$  threshold of the respective trigger. Level 1 and 2 also required prescale factors for all but the Jet 100 jet trigger. The prescale factors are discussed in Section 3.2.4. At an instantaneous luminosity of  $\mathcal{L} = 5 \cdot 10^{30} \text{cm}^{-2}\text{s}^{-1}$ , the Level 2 acceptance rate was approximately 12 Hz [47].

The Level 3 trigger system [60] was a software-based 'computer farm' that was capable of parallel processing of the events. The farm consisted of 64 commercially available processors, manufactured by Silicon Graphics. Level 3 ran the same jet clustering algorithm that was used in the offline analysis (see Section 3.1.1). It started by finding 1 GeV seed towers and summed over all towers with an energy of greater than 100 MeV inside a cone of radius 0.7. When a potentially interesting event was accepted by the Level 2 trigger, the data in the channels in the CDF detector were digitized and read out by the data acquisition (DAQ) system and transferred to the Level 3 processor farm. The Level 3 trigger reduced the event rate by a factor of two

to three, depending on the instantaneous luminosity.

Events accepted by the Level 3 trigger were passed on to the 'consumer server', a process running on a dedicated Silicon Graphics Challenge L computer. Several 'consumers' received data from the consumer server, running diagnostic applications and providing the CDF control room with graphical information about the detector performance. Data logger programs, running on the consumer server, wrote accepted events to local disks. Subsequently, these data logger events were written to 8-mm tapes by a tape-staging program.

# Chapter 3

## Measurement of the Dijet Mass Cross Section

### 3.1 Jets and Jet Algorithms

One of the most striking feature of events with hadrons in the final state is the appearance of jets of particles. The study of jets provides an intuitive approach to the analysis of such events. However, a quantitative analysis of jets requires an exact jet definition to determine which particles should be combined into a jet and a suitable algorithm has to be applied to each event. This algorithm generally contains one free parameter and a scheme for recombining the particles. Different jet algorithms lead to different numbers of jets being observed in any given event and as a result, jet cross sections depend on the procedure used to define a jet. Nevertheless, for each jet algorithm any given event contains a precisely defined number of jets. The jet algorithm must be applicable to both the observed data and the theoretical calculations, in order to compare the two.

The two main classes of jet finding routines are cluster and cone algorithms. Whereas cluster algorithms, like the JADE [61] or the  $k_T$  algorithm [62], assign every particle

in an event to one of the jets, cone algorithms assign particles to jets only if they are within a certain spatial distance of the jet axis and leave some particles unclustered. Because of this feature cluster algorithms are used primarily in  $e^+e^-$  collisions, where there is no initial state radiation and no underlying event, whose contributions could wrongly be added to the energies associated with the jets from the primary interaction. Most analyses of jets in  $p\bar{p}$  interactions, including the present one, use cone algorithms. The jet finding procedure according to the cone algorithm is explained in the following section.

Figure 3.1 shows a typical dijet event at CDF. A lego plot of the energy deposited in the calorimeter is shown in Fig. 3.1a). The two jets are back-to-back in azimuth and they balance the transverse energy of the event. The energy shown in this figure is divided into electromagnetic energy (light grey) and hadronic energy (dark grey). A side view of the same event, Fig. 3.1b), shows the reconstructed tracks of the particles and the energy deposited in the calorimeter. The event momentum is balanced by the remnants of the proton and the antiproton that are not observed in the detector in this event.

### 3.1.1 Jet Definition in the Cone Algorithm

In the cone algorithm used in this analysis [63], jets are defined by the energies and scattering angles of the particles in an event. Our jet finding routine, JETCLU [64], defined a cluster by the energy contained within a circle in  $\eta - \phi$  space. This circle has the radius

$$R = \sqrt{\eta^2 + \phi^2}, \quad (3.1)$$

where  $\phi$  is measured in radians. We refer to  $R$  as the *cone size*. A cone size of 0.7 was chosen for this analysis. The choice of  $R = 0.7$  is based partly on the distribution of energy flow with respect to the jet axis. It has been shown that cone size as small as 0.4 or as large as 1.0 yield good resolution [63, 65]. In this context, the choice of

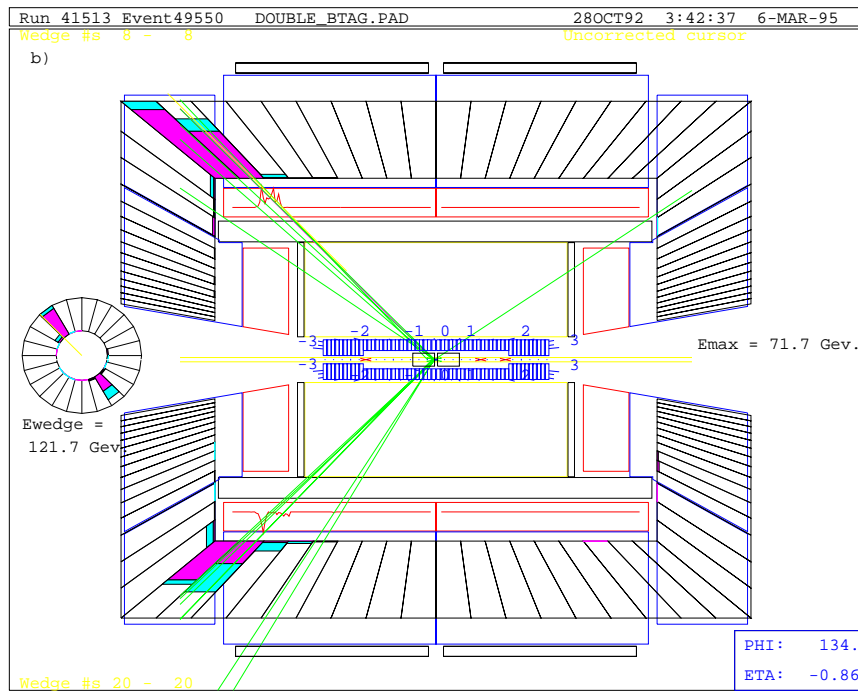
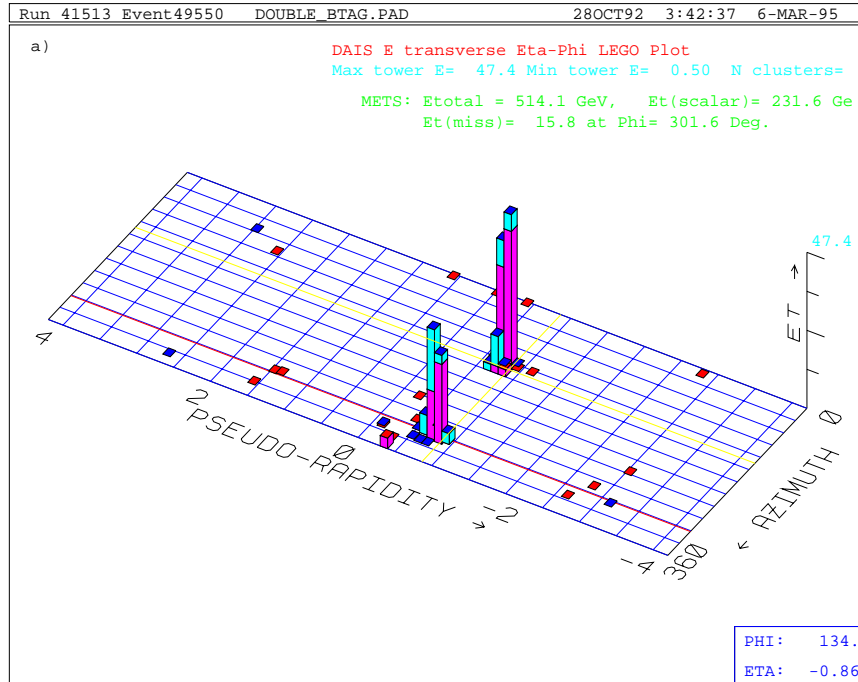


Figure 3.1: A typical dijet event at CDF. a) Lego plot of the energy deposited in the calorimeter. b) Side view of the same event.

$R = 0.7$  falls in the middle of a sensible range. It is important, however, that the QCD calculations used for comparisons reflect the size of the cone.

The basic unit of the JETCLU algorithm is a calorimeter tower. The total transverse energy in each tower was taken as the sum of the transverse electromagnetic energy and the transverse hadronic energy. The transverse electromagnetic energy in each tower was defined as the electromagnetic tower energy times  $\sin\theta_{EM}$ , where  $\theta_{EM}$  was determined by the  $z$  axis, the event  $z$  vertex and a point at the  $\eta$  center of the tower, ten radiation lengths from the event vertex [54]. The transverse hadronic energy was defined similarly, using a point at the  $\eta$  of the hadronic calorimeter tower, three interaction lengths from the event vertex.

The JETCLU algorithm started by finding seed towers, defined as towers containing a transverse energy of more than 1 GeV. Next, adjacent seed towers were combined to form preclusters. Adjacent seed towers in a precluster were required to have monotonically decreasing transverse energies and each precluster had to have a transverse energy of at least 2 GeV. The  $E_T$ -weighted centroids of all preclusters were then calculated. Clusters were formed by including all candidate towers within a circle with radius  $R = 0.7$  around the centroid. A candidate tower was required to have a transverse energy of more than 0.1 GeV. The cluster centroid was re-calculated and only candidate towers within the new circle were included in the new cluster. Seed towers were kept in the cluster, regardless of whether or not they fell into the new circle.

Since, at this stage, each cluster was formed without regard to the possible presence of other clusters, towers could be included in more than one cluster. In order to decide to which cluster a disputed tower should be assigned, the fraction of the shared energy was calculated for each pair of clusters. Two clusters were merged if the total transverse energy of all disputed towers was more than 75% of the transverse energy of either cluster. Otherwise the clusters were separated and each disputed tower was assigned to the closer cluster. The centroids of all clusters were recalculated and the this process was iterated until the list of towers assigned to the clusters no longer

changed. This procedure typically converged after the first iteration. Figure 3.2 shows a flow diagram of the JETCLU algorithm.

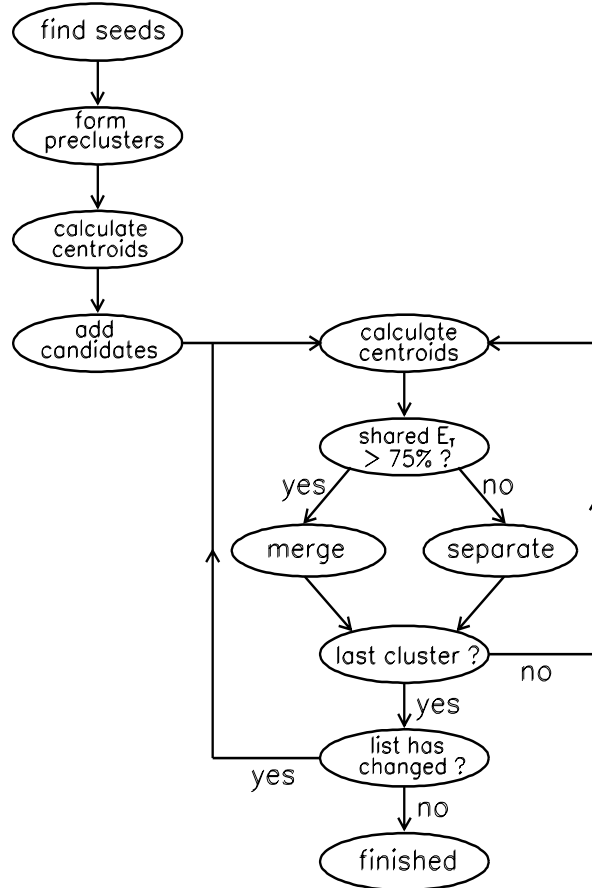


Figure 3.2: Flow diagram of the JETCLU algorithm.

### 3.1.2 Jet 4-Vectors

From the energies in the calorimeter towers and the list of towers assigned to the jets, the following quantities were determined for each jet:

- The energy

$$E = \sum_i E_{EM}^i + E_{HAD}^i, \quad (3.2)$$

with  $E_{EM}$  and  $E_{HAD}$ , the electromagnetic and hadronic energy of the jet, respectively. The sum runs over all calorimeter towers that were assigned to the

jet,

- the 3-momentum

$$p_x = \sum_i (E_{EM}^i \sin \theta_{EM}^i + E_{HAD}^i \sin \theta_{HAD}^i) \cos \phi^i \quad (3.3)$$

$$p_y = \sum_i (E_{EM}^i \sin \theta_{EM}^i + E_{HAD}^i \sin \theta_{HAD}^i) \sin \phi^i \quad (3.4)$$

$$p_z = \sum_i E_{EM}^i \cos \theta_{EM}^i + E_{HAD}^i \cos \theta_{HAD}^i, \quad (3.5)$$

with the polar and azimuthal angles of the towers,  $\theta^i$  and  $\phi^i$ ,

- the total momentum

$$p = \sqrt{p_x^2 + p_y^2 + p_z^2}, \quad (3.6)$$

- the polar angle

$$\theta = \cos^{-1} \left( \frac{p_z}{p} \right), \quad (3.7)$$

- the transverse energy

$$E_T = E \sin \theta, \quad (3.8)$$

- and the pseudorapidity

$$\eta = -\ln \left( \tan \frac{\theta}{2} \right). \quad (3.9)$$

### 3.1.3 Jet Energy Corrections

In general, the measured energy of a jet in the detector is different from its *true* energy. This is due to a variety of *calorimeter response* effects. The non-uniform nature of the calorimeter, e.g. due to the presence of crack regions, leads to a significant variation in the detector response as a function of  $\eta_d$ . Furthermore, the calorimeter exhibited a slight energy non-linearity for very low-energy particles, which resulted in a fragmentation-dependent jet energy measurement. Finally, underlying event particles increased the effective energy found in the jet cones. To correct the data for

these effects, jet energy corrections were applied. These corrections for calorimeter response should not be confused with the unsmearing corrections discussed in Chapter 4.

The jet energy corrections were applied in two stages, the *relative* and the *absolute* energy scale corrections. The relative energy scale is a measure of the response of the non-central regions of the detector, relative to the central region. This relative correction was used to transform the transverse momentum of a given jet into the transverse momentum that would have been measured, had that jet been detected in the central region. This was necessary to compensate for calibration mismatches between the different regions of the detector. Next, the absolute jet corrections were applied, which yielded the corrected jet energy. The jet energy corrections are described in detail in [66].

We did not correct the data for jet clustering effects since the theoretical calculations are performed for quarks and gluons inside the jet cones. Particles that are radiated outside the jet clustering cone, e.g. an extra gluon, lead to similar losses in the theoretical calculations and the data. The energy corrections increased the jet energies, on average, by 20% (16%) for uncorrected jet energies of 100 GeV (400 GeV).

## 3.2 The Data Sample

This analysis is based on data collected during the 1994-95 Tevatron running period, also called Run 1B, when an integrated luminosity of  $86.3 \pm 3.5 \text{ pb}^{-1}$  was recorded. The mean instantaneous luminosity delivered to the CDF experiment during Run 1B was  $8.0 \cdot 10^{30} \text{ cm}^{-2} \text{ s}^{-1}$  with peak instantaneous luminosities of  $2.6 \cdot 10^{31} \text{ cm}^{-2} \text{ s}^{-1}$  [43]. The integrated luminosity of our data sample was measured to be  $85.9 \text{ pb}^{-1}$  by summing up the luminosities of all runs that were used for the analysis.

### 3.2.1 Event Selection

During Run 1B, given a total  $p\bar{p}$  cross section of about 80 mb [29], the CDF detector was spectator to roughly  $7 \cdot 10^{12}$  proton-antiproton collisions. For this analysis only physics events in a selected kinematical range, with two or more jets, were of interest. We selected these from the bulk of events that were irrelevant for this analysis. Since our analysis does not involve any of the muon detection systems, we selected runs that were good for non-muon analyses. Background events were removed by applying the following selection criteria:

- Events containing large amounts of hadronic energy in the calorimeter that was *out-of-time* with the proton-antiproton beam crossing were removed by using timing signals from TDC's on the central and endwall hadron calorimeters. These out-of-time events could stem from cosmic rays, beam-gas interactions or accelerator losses (splashes) from the Main Ring. Events where one or more photomultiplier tubes gave unphysically large signals, due to high voltage discharges (*spikes*) were also removed by this requirement.
- When a cosmic ray traverses the detector, the resulting signature contains a large amount of missing transverse energy,  $\cancel{E}_T$ , defined to be the vector sum of all transverse energy in an event. The missing- $E_T$  significance [67]

$$S_{\cancel{E}_T} = \frac{\cancel{E}_T}{\sqrt{\sum E_T}} \quad (3.10)$$

is a measure for the relative imbalance of  $E_T$  in the detector. To reject cosmic ray events we required  $S_{\cancel{E}_T}$  to be less than  $6\sqrt{\text{GeV}}$  and the total energy,  $\sum E$ , to be less than 2 TeV.

- We required the absolute  $z$  component of the vertex to be less than 60 cm, in order to ensure that the events were fully contained in the calorimeter and to preserve the projective geometry of the calorimeter towers. The vertex was determined by using the information from the tracking chambers, mostly the

VTX.

- Finally, we required at least two jets in each event.

We defined the dijet system according to Eqn. (1.15) and applied the following kinematical selection criteria, based on the corrected jet quantities, to our data sample:

- We required the physics pseudorapidity of the two leading jets to satisfy  $|\eta_1| < 2.0$  and  $|\eta_2| < 2.0$ . If either of the two highest- $E_T$  jets was detected in the region  $|\eta| > 2.0$  we discarded the event. This requirement excluded events with jets that were mainly in the forward / backward calorimeters.
- The jet triggers were based on the transverse energy of the events and, since the transverse energy is a steeply falling spectrum, the trigger efficiencies strongly depended on the jet  $E_T$ . Figure 3.3 shows the dijet system schematically.

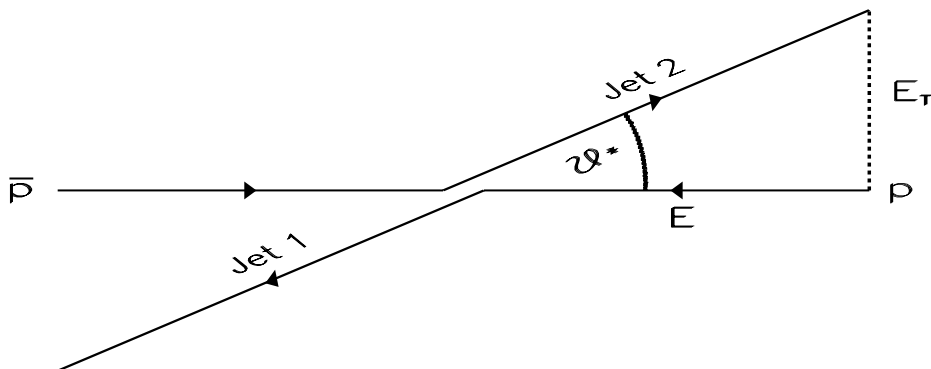


Figure 3.3: Schematic view of the dijet mass system.

To lowest order (2 jets only) and in the zero-mass approximation, the two jets have equal energies and are scattered back-to-back. Their scattering angle,  $\theta^*$ , is given by

$$\sin \theta^* = \frac{E_T}{E} = \frac{2E_T}{M_{jj}}. \quad (3.11)$$

The second equality follows from the definition of the dijet mass (Eqn. (1.15)) and  $\vec{p}_1 = -\vec{p}_2$ . Events with higher values of  $\sin \theta^*$ , corresponding to lower values of  $\cos \theta^*$ , were therefore selected with a higher probability. To ensure a high

trigger efficiency over the whole selected dijet mass range, we required the dijet system to satisfy  $|\cos \theta^*| \equiv \tanh(\eta^*) < 2/3$ , with  $\eta^* = \frac{1}{2}(\eta_1 - \eta_2)$ .

These criteria selected 61 002 events for the analysis.

The pseudorapidity cut and the  $\cos \theta^*$  cut defined our data sample. We did not correct for the acceptance of these two cuts. Instead, we will include these two cuts in the theory calculations of the dijet mass cross section.

### 3.2.2 Trigger Efficiencies

We selected events that were in a kinematical range with high trigger efficiencies to avoid large systematic uncertainties that are associated with low trigger efficiencies.

We measured the efficiency of the Run 1B jet triggers by looking at the next-lower threshold jet triggers and asking how often did the highest- $E_T$  Level 2 cluster pass the lower Level 2  $E_T$  threshold. For example, in order to measure the efficiency of the Jet 70 trigger, we used the Jet 50 trigger sample and measured a) the rate as a function of corrected dijet mass and b) the same rate with the additional requirement that the Level 2  $E_T$  was greater than 70 GeV. The ratio of the latter number divided by the former was the efficiency of the Level 2 Jet 70 trigger. The Level 3 triggers cut less stringently on energy than Level 2 and was thus fully efficient for events that passed the Level 2 trigger.

The efficiencies of the three lowest jet triggers, as a function of the corrected dijet mass, are shown in Fig. 3.4. We used data from the triggers beginning at the mass marked with a dotted line and ending where the next trigger begins.

For the Jet 20 trigger we had no lower threshold trigger to measure the efficiency. Instead, we estimated the dijet mass where the Jet 20 trigger would start to be fully efficient. Figure 3.5 shows the mass thresholds that correspond to full efficiency of the Jet 50, 70 and 100 triggers. The solid line is an extrapolation down to the Jet 20 trigger. To ensure full efficiency of the Jet 20 trigger, we chose a mass threshold of

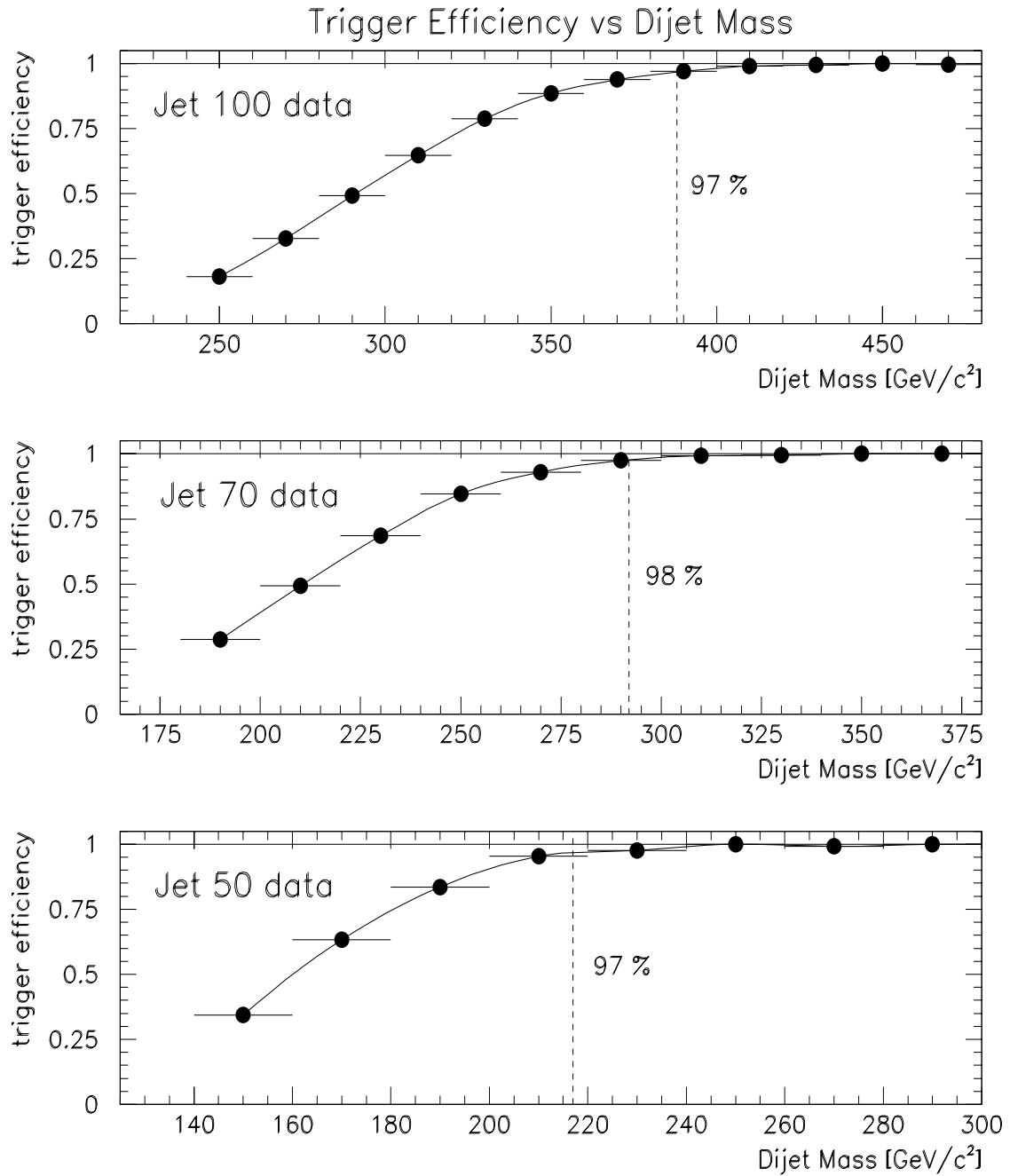


Figure 3.4: The Run 1B trigger efficiencies for the Jet 100 trigger (top), Jet 70 trigger (middle) and Jet 50 trigger (bottom) as a function of the dijet mass. The solid lines are smooth fits. Indicated are the mass cuts for this analysis (dashed lines) and the efficiencies at threshold. The horizontal bars indicate the widths of the dijet mass bins.

$M_{jj} > 180 \text{ GeV}/c^2$ , as indicated by the open circle.

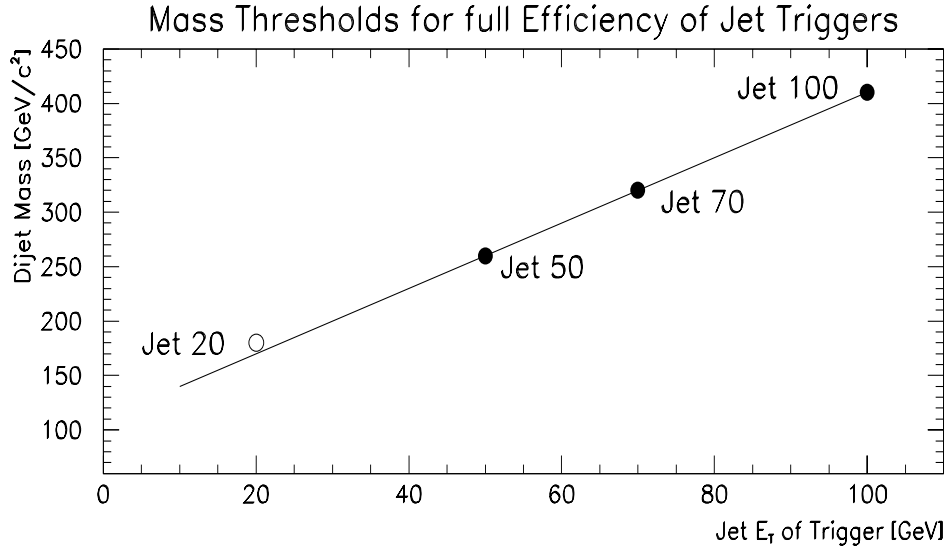


Figure 3.5: Mass thresholds corresponding to full efficiency of the jet triggers. The measured thresholds of the Jet 50, 70 and 100 triggers are indicated by the full circles. The solid line is an extrapolation to the Jet 20 trigger. We chose a mass threshold of  $M_{jj} > 180 \text{ GeV}/c^2$ , as indicated by the open circle.

### 3.2.3 $z$ -Vertex Cut Efficiency

Figure 3.6 shows the  $z$ -vertex cut efficiency for the individual dijet mass bins. To account for the slightly decreasing value of the efficiency at low dijet masses, we used a linear parameterization that increases from 92.5% for the lowest mass bin to 94.2% for the mass bin starting at  $388 \text{ GeV}/c^2$ . Above a dijet mass of  $388 \text{ GeV}/c^2$  we used a constant value of 94.2%. The solid line indicates the values used in this analysis. The data have been corrected for the  $z$ -vertex cut efficiency.

### 3.2.4 Jet Trigger Prescale Factors

The Run 1B data sample was collected with four jet triggers with threshold energies of 20, 50, 70 and 100 GeV, respectively. The three lowest jet triggers were prescaled

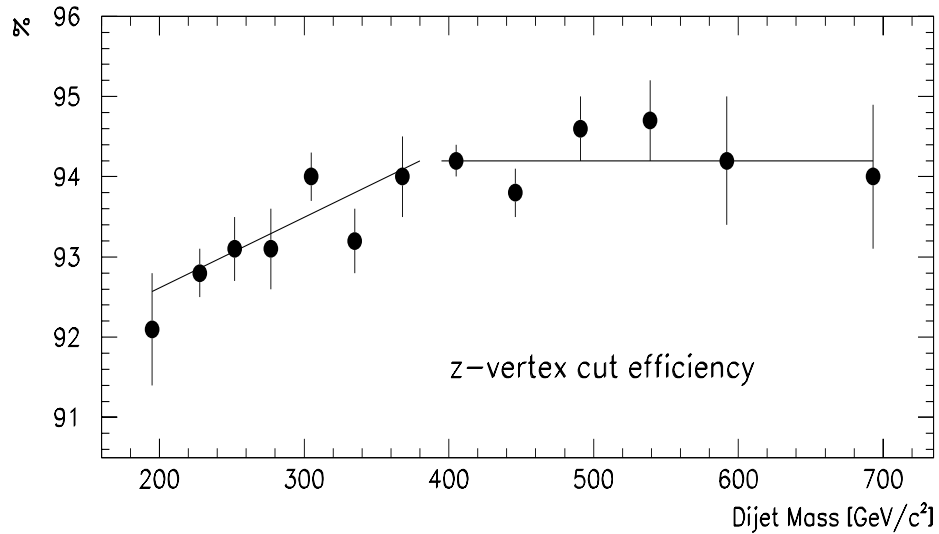


Figure 3.6: The  $z$ -vertex cut efficiencies for the individual dijet mass bins. The values we used in this analysis are indicated by the solid line.

to limit statistics for more common event signatures. The prescaling was done on the first two trigger levels. Level 1 required the Jet 20 and 50 triggers to pass the prescale 40 trigger, which randomly passes on one out of every 40 events to the next-higher trigger level. Similarly, Level 2 involved a prescale 25 trigger for the Jet 20's and a prescale 8 trigger for the Jet 70's.

We measured the prescale factors of the jet triggers by comparing the dijet mass cross sections in the overlap region between adjacent jet triggers. Using the Jet 100 trigger (which is not prescaled) as our reference sample, we first measured the prescale factor of the Jet 70 sample. Next we determined the prescale factor of the Jet 50 sample, relative to the Jet 70 sample and finally the prescale factor of the Jet 20 sample with respect to the Jet 50 sample. Table 3.1 lists our measured values with their statistical uncertainties and the nominal prescale factors.

Whereas the prescale factors of the Jet 20 and Jet 70 triggers are in agreement with their nominal values, the prescale factor for the Jet 50 sample is lower than its nominal value. Since the Jet 50 trigger is the only one that was prescaled exclusively by the Level 1 trigger, this is an indication of a problem with the Level 1 prescale factor.

Level 2 Triggers	Measured Prescale Factor	Nominal Value
Jet 70 / Jet 100	$8.03 \pm 0.15$	8
Jet 50 / Jet 70	$4.81 \pm 0.08$	5
Jet 20 / Jet 50	$24.6 \pm 0.8$	25

Table 3.1: Measured and nominal values for prescale factors of the jet trigger bits.

Although we did not see similar problems with the the Level 2 trigger, which prescales the Jet 70 and the Jet 20 triggers, we decided to use our measured values for all three jet triggers. Our values agree well with the ones from the inclusive jet- $E_T$  analysis [68] of 24.66 and 'exactly 8' for the Jet 20 and the Jet 70 sample, respectively. No measured value for the Jet 50 trigger is given in [68]. The trigger efficiencies at threshold and the total prescale factors are listed in Table 3.2.

Level 2 Trigger	Mass Cut (GeV/ $c^2$ )	Efficiency	Prescale Factor
Jet 20	180	1.00	949
Jet 50	217	0.97	38.6
Jet 70	292	0.98	8.03
Jet 100	388	0.97	1.00

Table 3.2: Level 2 triggers, mass cuts, efficiencies at threshold and prescale factors.

### 3.2.5 Properties of the Data Sample

Figures 3.7 and 3.8 show the distributions of some of the kinematic and angular variables of our data sample. The distributions are compared to the ones of the Monte Carlo sample. The Monte Carlo events were generated with the PYTHIA Monte Carlo program [69]. Because of the different prescale factors of the three jet triggers, we

chose not to plot the distributions of the complete sample. All distributions shown are for the events that passed the Jet 100 trigger, after the application of all selection cuts, including the kinematical cuts. Since the comparisons are for illustrative purposes only, the number of entries in each histograms for both the data and the Monte Carlo events were normalized to one.

The  $p_T$  distributions, shown in Fig.3.7a) and b), turn on steeply at low transverse momenta and then approximately fall with  $dN/dp_T \sim 1/p_T^6$ . This rapid fall-off is the result of many factors: the decrease of the parton distribution functions with increasing  $x$ , the fall-off of the subprocess cross section proportional to  $1/\hat{s}$  and, to a lesser degree, the slight decrease of  $\alpha_s$  with increasing  $Q^2$ . The dijet mass distribution is plotted in Fig.3.7c). The Monte Carlo distribution reproduces the shape of the data well. The  $\cos\theta^*$  distribution (Fig.3.7d)) is symmetrical around zero and peaks at values of  $\pm 1$ , corresponding to the poles of  $2 \rightarrow 2$  Rutherford scattering.

Figure 3.8 shows the  $\eta_d$  and  $\phi$  distributions of the two leading jets. As expected, the  $\eta_d$  distributions are symmetrical around zero. The slightly coarse structure between  $\eta_d = 0$  and  $\pm 0.2$  reflect the imperfect jet energy corrections in the region of the  $90^\circ$  crack that is not completely modeled. The  $\phi$  distributions are flat across the whole range of  $2\pi$  and are consistent with the expectation of azimuthally symmetric distributions.

A scatter plot of the  $\phi$  values of the first two jets is shown in Fig.3.9. To leading order, all jets are back-to-back in  $\phi$ . However, higher-order radiation effects, resulting in three or more jets in the final state, cause deviations from the leading order expectation.

### 3.3 The Dijet Mass Distribution

Figure 3.10 shows the partially corrected dijet differential cross section as a function of the dijet mass. Over the kinematical range of the selected events the cross section

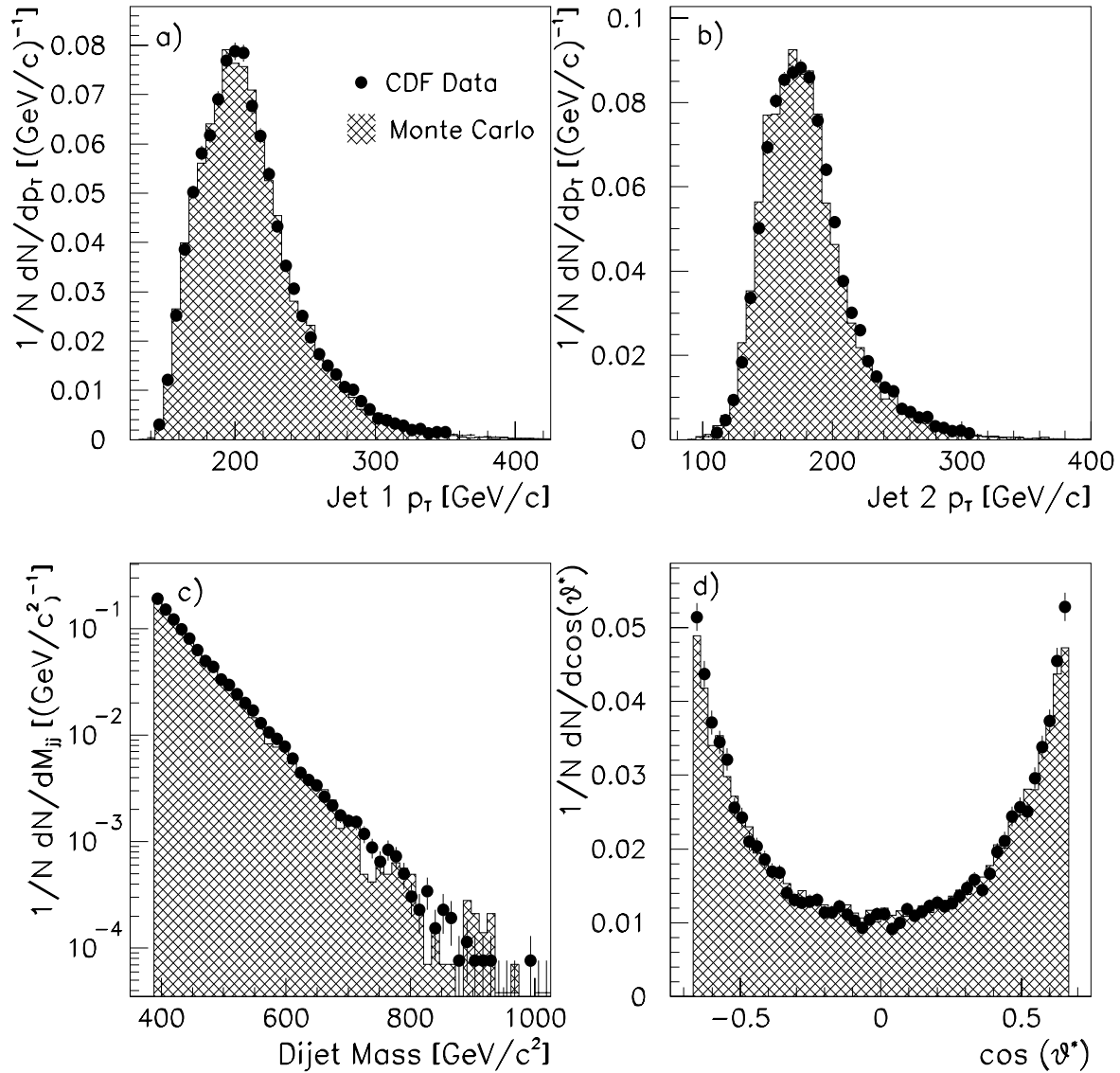


Figure 3.7: Comparison of kinematic variables of our data set (full circles) and the Monte Carlo events (histograms). a) and b) the transverse momenta of the two highest-energy jets, c) the dijet invariant mass and d)  $\cos \theta^*$ . The number of entries for both the data and the Monte Carlo events were normalized to one.

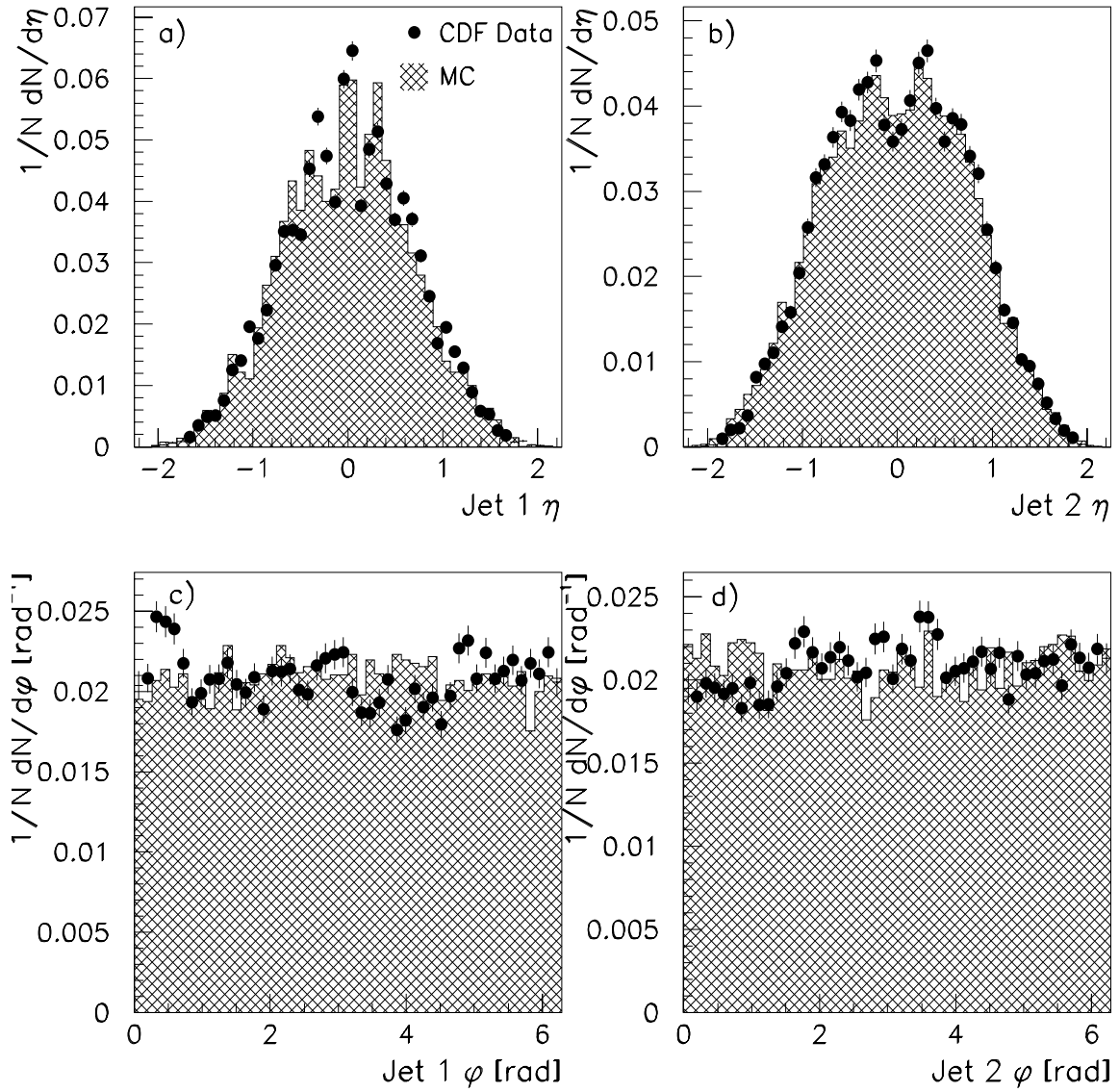


Figure 3.8: Comparison of the angular variables of the two highest-energy jets. a) and b) detector  $\eta$ , c) and d) the azimuthal angle,  $\phi$ . The number of entries for both the data and the Monte Carlo events were normalized to one.

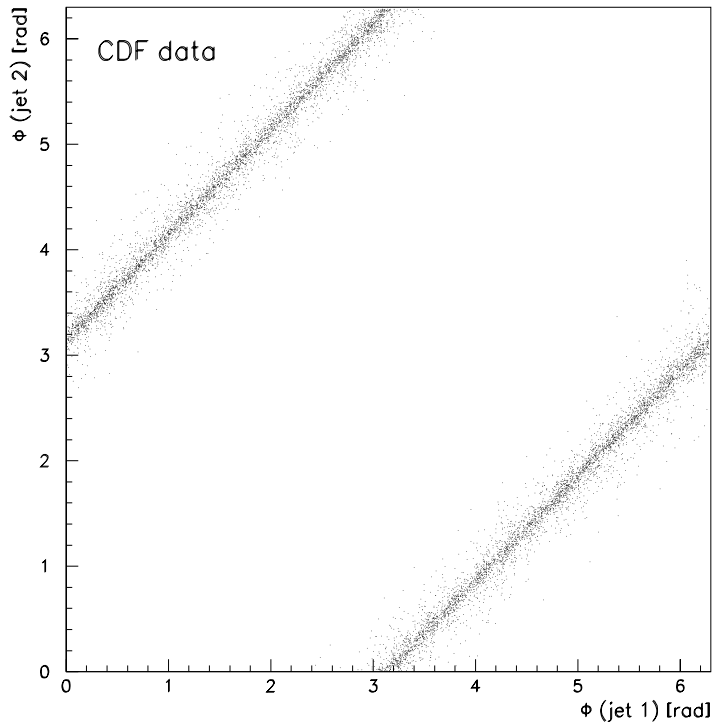


Figure 3.9: Scatter plot of the  $\phi$  distributions of the two leading jets.

falls by six orders of magnitude. Here the data are corrected for trigger efficiencies,  $z$  vertex cut efficiency, and calorimeter response, but are not yet corrected for detector resolution effects. The error bars represent the statistical uncertainties in bins of dijet mass. The bins are approximately 10% wide, reflecting the resolution of the detector.

Throughout this analysis we use the functional form

$$f(m) = \frac{A(1 - \frac{m}{\sqrt{s}} + C\frac{m^2}{s})^N}{m^P}, \quad (3.12)$$

to parameterize the dijet mass distribution. The parameters  $A$ ,  $C$ ,  $N$  and  $P$  are determined by a fit to the data. The term in parentheses imitates the parton distribution fall-off at high  $x \sim m/\sqrt{s}$  and the term  $1/m^P$  models the drop-off of the matrix element with  $m$ . In order to ensure that Eqn. (3.12) is an appropriate description of the dijet mass spectrum, we show the fractional differences between the data and this parameterization in Fig. 3.11.

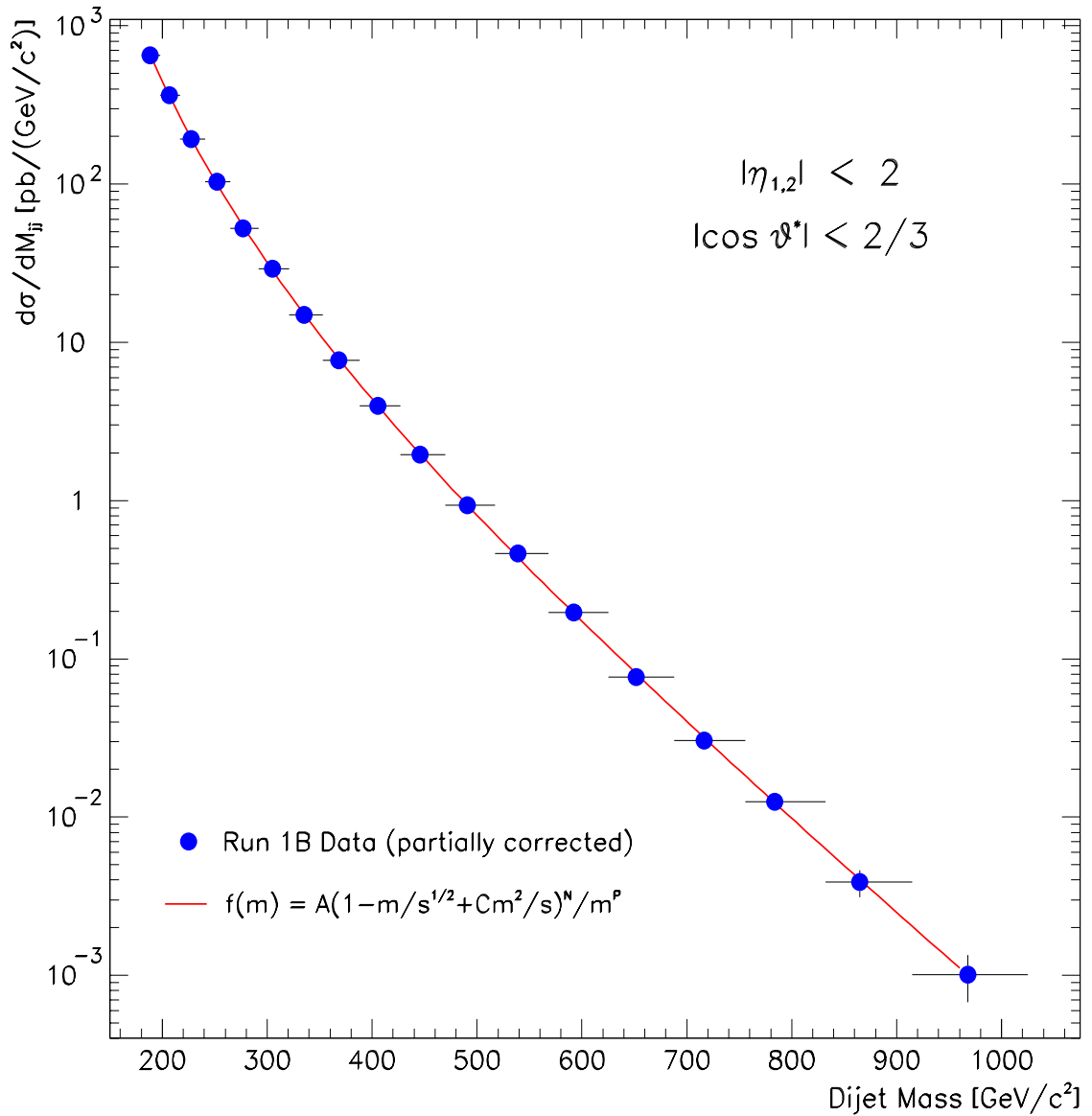


Figure 3.10: The partially corrected differential dijet mass cross section. The data have not yet been corrected for detector resolution effects. The vertical bars represent the statistical errors and the horizontal bars represent the widths of the dijet mass bins. The solid line is a fit of a parameterization to the data.

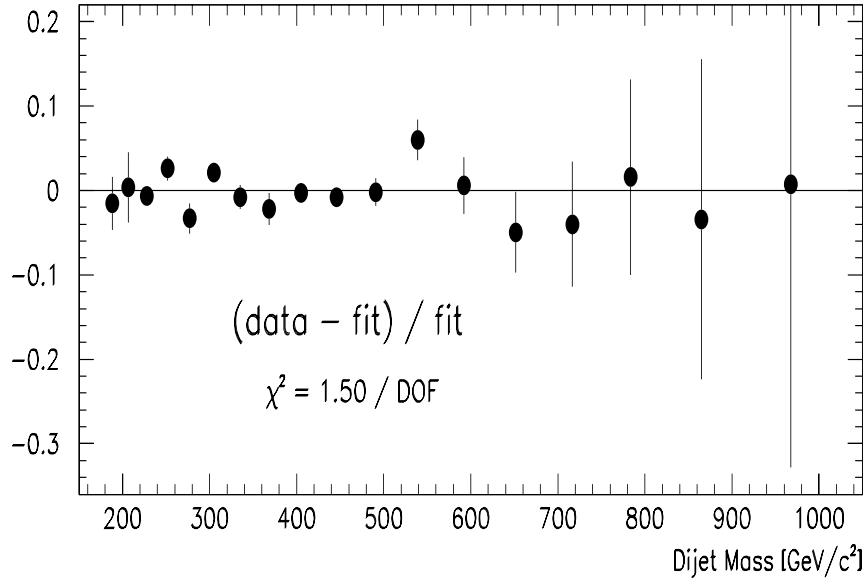


Figure 3.11: Fractional differences between the partially corrected data and the parameterization.

The fit to the data returned the following values for the parameters:  $A = 6.67 \cdot 10^{17}$ ,  $C = 2.95$ ,  $N = -6.98$  and  $P = 6.70$ . The  $\chi^2$  of this fit was 21.0 / 14 DOF or 1.50 / DOF. We also used this functional form to parameterize the true and measured distributions in both the analytical unsmearing procedure and the Monte Carlo method (see below).

# Chapter 4

## The Unsmearing Procedure

### 4.1 Calorimetry

Conceptually, a calorimeter is a block of matter that intercepts the primary particle and causes it to interact and to deposit all its energy in the subsequent cascade or *shower* of increasingly lower-energy particles. Eventually, all the incident energy is deposited and some fraction of it is detected in the form of scintillation light (or, in the case of gas calorimeters, in form of ionization charge), which is proportional to the incident particle energy.

Calorimeters offer many attractive capabilities, among them:

1. They are sensitive to neutral and charged particles;
2. their different responses to muons, electrons and hadrons can be exploited for particle identification;
3. segmented calorimeters provide information on the shower development, allowing precise measurements of the positions and angles of the incident particles;
4. while the size of electromagnetic spectrometers scales with the momentum,  $p$ , as  $\sqrt{p}$ , the length of calorimeters scales only logarithmically with the particle

energy, making calorimeters the more compact and more economical device to measure particle energies at collider experiments;

5. the fast time response of scintillator-based calorimeters allows operation at high particle rates.

In the following sections electromagnetic and hadronic shower developments are discussed.

### 4.1.1 Electromagnetic Showers

The principal energy loss mechanisms for electrons (and positrons) are ionization loss and radiation loss or *bremstrahlung*. While the rate of ionization loss for fast electrons is approximately constant, the average radiation loss is roughly proportional to the electron energy. Radiation is therefore the dominant source of energy loss for high-energy electrons. The critical energy,  $E_c$ , at which the two rates are equal is approximately given by [40]

$$E_c \approx \frac{600}{Z} \text{MeV} \quad (Z \geq 6), \quad (4.1)$$

where  $Z$  is the atomic number.

When discussing electromagnetic showers, it is useful to introduce a quantity called the *radiation length*,  $X_0$ . One radiation length is the distance over which the incident electron energy,  $E_0$ , is reduced by a factor of  $1/e$  due to radiation losses only. In the high-energy limit, where processes other than radiation loss can be ignored and where the rate of radiation loss is independent of the electron energy, the particle energy can be expressed as [70]

$$E(x) = E_0 \exp\left(\frac{-x}{X_0}\right), \quad (4.2)$$

where  $x$  is the distance traveled.

There are three processes responsible for the attenuation of  $\gamma$ -rays in matter: photo-

electric absorption, Compton scattering and  $e^+e^-$  pair production. For photons with energies of a few MeV or more, the process of pair production is the dominant source of energy loss. The attenuation of a beam of high-energy photons of intensity  $I_0$  by pair production is given by [40]

$$I(x) = I_0 \exp\left(\frac{-7x}{9X_0}\right), \quad (4.3)$$

so that the intensity is reduced by a factor  $1/e$  after a distance of  $9/7$  of a radiation length.

For high-energy electrons and photons, the result of the combined phenomena of bremsstrahlung and pair production is the occurrence of showers. The development of an electromagnetic shower can be discussed according to the following very simplified model. A parent electron of incident energy  $E_0$ , in traversing one radiation length, radiates half its energy as one photon. Within the next radiation length the photon converts to an  $e^+e^-$  pair, transferring half its energy to the electron and positron each, while the original electron radiates off another photon. Thus, after two radiation lengths, a single electron of energy  $E_0$  is replaced by two electrons, one positron and one photon, each particle carrying the energy  $E_0/4$ . After  $t$  radiation lengths, the number of particles produced will be  $N = 2^t$ , with roughly equal number of electrons, positrons and photons, all with the energy  $E(t) = E_0/2^t$ . The shower development continues until the energy per particle becomes equal to the critical energy  $E_c$ , at which point ionization losses become important and no further radiation occurs. Thus the shower reaches a maximum and then ceases abruptly. The shower maximum occurs at

$$t_{max} = \frac{\ln(E_0/E_c)}{\ln 2} \quad (4.4)$$

and the maximum number of particles produced is given by

$$N_{max} = 2^{t_{max}} = \frac{E_0}{E_c}. \quad (4.5)$$

In a more realistic model, the shower development consists of an initial geometric rise, followed by a broad maximum and a gradual decline. The characteristic shape of electromagnetic showers can be parameterized according to [71]

$$dE/dt = N \cdot t^\alpha e^{-\beta t}, \quad (4.6)$$

where  $\alpha$  and  $b$  are energy dependent parameters and  $N$  is the normalization factor, given by

$$N = E_0 \cdot \beta^{\alpha+1} / (\alpha + 1). \quad (4.7)$$

A rigorous analytical description of the longitudinal electromagnetic shower profile can be found in [72].

The two parameters  $\alpha$  and  $\beta$  determine the longitudinal shape of an electromagnetic shower. Figure 4.1 shows the typical longitudinal shower shape. The start of the shower and the steepness of the rising part of the curve are controlled by  $\alpha$ , whereas the steepness of the fall-off and the length of the tail of the curve are determined by  $\beta$ .

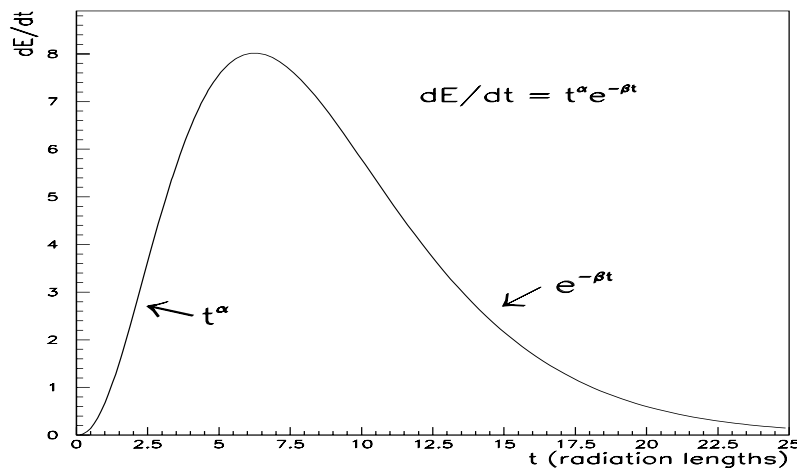


Figure 4.1: The longitudinal shape of an electromagnetic shower.

It is clear from this qualitative discussion of electromagnetic showers that the shower development, the production of secondary and tertiary particles, is a stochastic pro-

cess. The signal that is detected in a calorimeter depends on the actual number of particles produced, which varies from case to case. In other words, particles of the same type and of identical energies and incident angles produce signals that are distributed according to a Gaussian probability distribution. In general, the distribution gets narrower with increasing particle energies because particles of higher energies produce greater numbers of secondary particles. Since the number of secondary particles is proportional to the energy of the incident particle, the resolution of a calorimeter improves with  $\sqrt{E_0}$ .

As an illustrative example, Fig. 4.2 shows the electromagnetic response of a GEANT-based [73] Monte Carlo simulation of the CDF Plug Upgrade Calorimeter to positrons [74]. The Plug Upgrade calorimeter will replace the existing Plug Calorimeter for the Tevatron Run 2 [75], scheduled to start in April 2000. Figure 4.2a) and b) show the values of  $E/p$ , where  $E$  is the energy detected in the calorimeter simulation and  $p$  is the momentum of the simulated particles, for two different momenta, 11 and 150 GeV/c. Fits to the calorimeter responses are indicated to show that they follow a Gaussian distribution. The detector resolution, shown in Fig. 4.2c), improves with  $\sqrt{E}$ , as indicated by the solid line.

### 4.1.2 Hadronic Showers

Conceptually, the development of hadronic showers is the same as that of electromagnetic showers. However, the much greater variety and complexity of hadronic processes complicate its detailed understanding and no straightforward analytical description of hadronic processes is available. Nonetheless, the elementary physical processes that cause the propagation of hadronic showers are empirically studied.

A hadronic particle loses energy mainly via the process of ionization until it interacts strongly with a nucleus in the absorber material. In a hadronic interaction about half the incident hadron energy is passed on to additional fast secondary particles. The remainder is consumed in multi-particle production of slow pions and other processes.

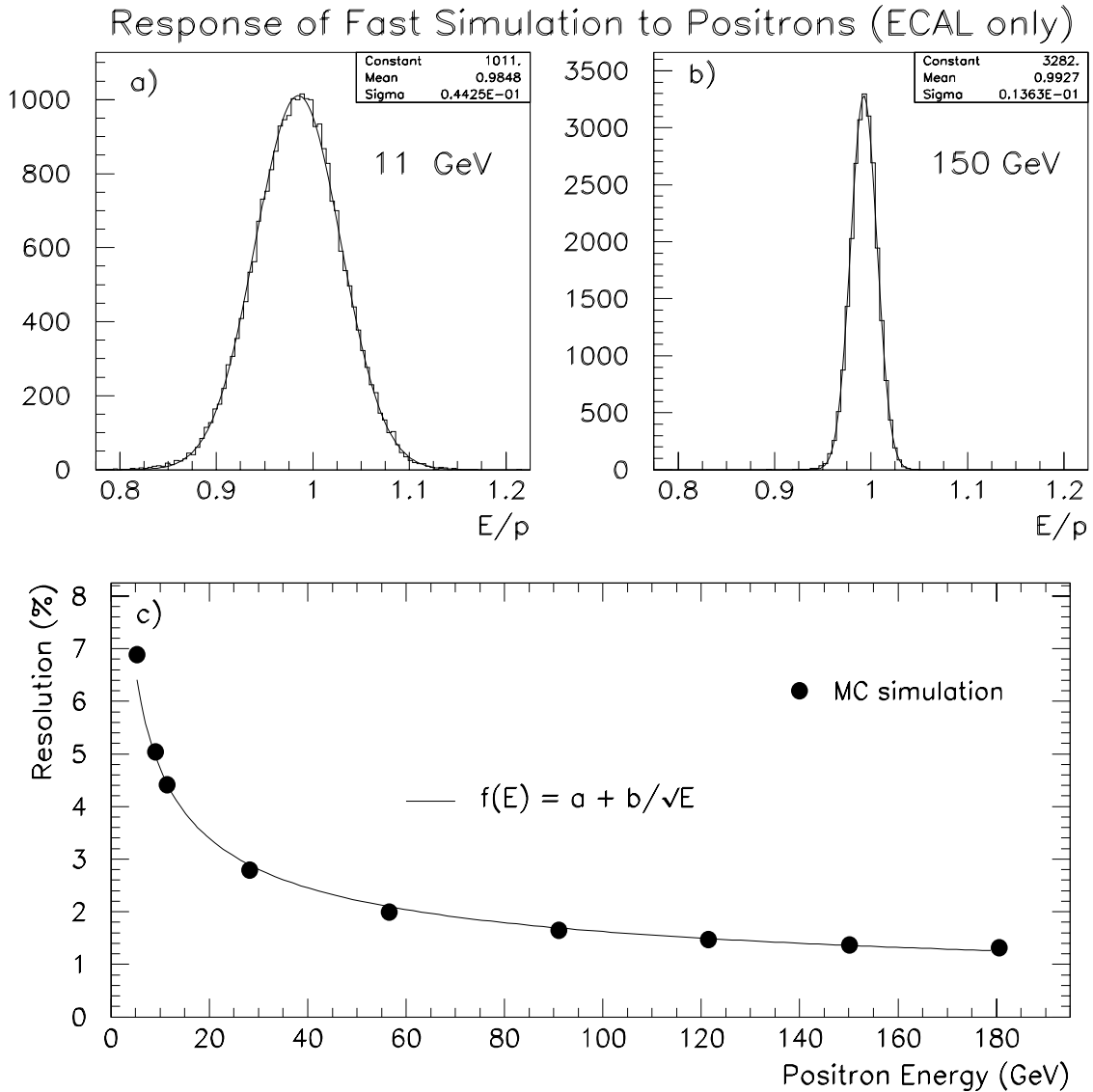


Figure 4.2: The response of a detector Monte Carlo simulation to positrons. a) and b) The values of  $E/p$ , where  $E$  is the energy detected and  $p$  is the momentum of the incident particles, for  $p = 11 \text{ GeV}/c$  and  $p = 150 \text{ GeV}/c$ . The solid lines represent Gaussian fits to the histograms. c) The resolution of the simulation as a function of the incident positron energy.

A typical secondary hadron is produced with a transverse momentum of  $0.35 \text{ GeV}/c$  [71]. As a result, hadronic showers are usually more spread out laterally than their electromagnetic counterparts.

Most of the energy is dissipated by ionization losses of secondary particles [76]. The next-largest sources of energy loss, the production of  $\pi^0$ 's from nuclear interactions and the breakup of nuclei, are also responsible for the physics limitations to the energy resolution of hadronic calorimeters.

1. A considerable number of the secondary particles are  $\pi^0$ 's that immediately decay into two photons and thus give rise to electromagnetic showers inside a hadronic one. The average fraction of energy converted into  $\pi^0$ 's is given approximately by  $0.1 \ln E(\text{GeV})$  for energies in the range of a few hundred GeV [71], typical of the jets in this measurement.
2. In a hadronic cascade roughly 30% of the incident energy is lost through processes that do not produce detectable signals, e.g. the breakup of nuclei or nuclear excitation [40]. One successful method of compensating for this effect is the use of  $^{238}\text{U}$  as absorber material. The extra energy released by fast neutron and photon fission of  $^{238}\text{U}$  makes up for the undetectable energy from nuclear breakups.

These two (correlated) processes lead, for a given hadron, to large fluctuations in the shower composition and very different detectable calorimeter responses. Together, they impose the intrinsic limitation on the performance of hadronic calorimeters, resulting in generally considerably poorer energy resolutions than for electromagnetic calorimeters.

In conclusion, the response of a calorimeter to a particle (or jet) of given energy is intrinsically limited by statistical fluctuations, resulting in a finite energy resolution of the detector. In the following section we explain how this leads to a smearing of the measured dijet mass cross section.

## 4.2 Jet Energy Smearing

The detector responds to jets of a given energy with a Gaussian-like distribution, rather than with a  $\delta$ -function distribution. This leads to a smearing of the true jet energies and a shift of the measured differential dijet mass cross section, see Fig. 4.3.

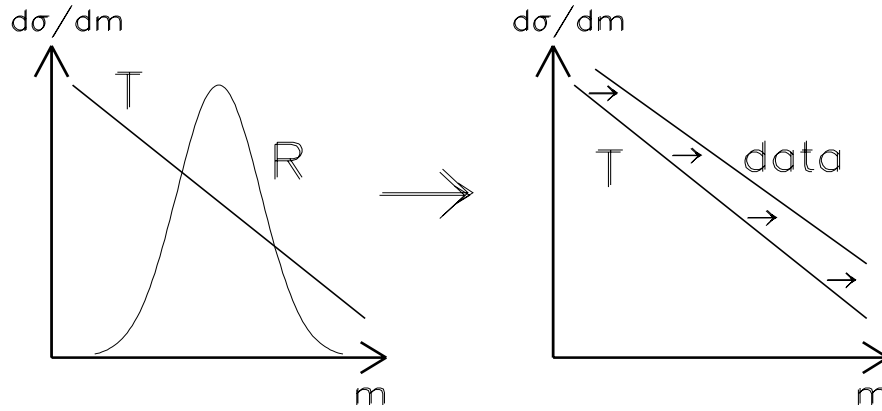


Figure 4.3: The finite detector resolution leads to a *smearing* of the true differential cross section. The observed distribution (the data) is shifted with respect to the true distribution.

The actual shape and magnitude of this shift depends on the detector resolution and the shape of the true distribution. In order to compare the data with predictions from QCD calculations, the data are corrected for these effects.

The observed spectrum can be described as a convolution of the true spectrum and the detector resolution function:

$$\frac{d\sigma^{bin}}{dM_{jj}} = \frac{\int^{bin} dm_{meas}}{\text{bin width}} \int_0^\infty R(m_{meas}, m_{true}, X) T(m_{true}, A, C, N, P) dm_{true}, \quad (4.8)$$

where  $\frac{d\sigma^{bin}}{dM_{jj}}$  is the cross section measured in a dijet mass bin. The detector response function,  $R$ , is dependent on the measured dijet mass,  $m_{meas}$ , the true dijet mass,  $m_{true}$ , and a set of parameters,  $X$ . The parameterized true spectrum,  $T$ , is dependent on the true mass and the four parameters  $A$ ,  $C$ ,  $N$  and  $P$ .

The integration over the true mass takes into account the contributions to the cross section in a certain data bin from all true dijet masses. In principle, this integration should be performed from 0 to  $\infty$ . Practically, a lower limit must be imposed on the integration because the parameterization of the true spectrum we use increases without bound at low dijet masses. In this analysis the lower limit of integration has been set to  $50 \text{ GeV}/c^2$ . The result of the integration did not change if this limit was lowered any further.

The integration over the measured mass takes into account the fact that the events are distributed over the whole bin and are not confined to the center of the bin. It was performed over the respective data bins and the result was divided by the width of the bin.

In order to deconvolute the data we applied the following procedure.

1. We parameterized the detector resolution and the true spectrum. The parameterization of the detector response is described in Section 4.6. The true spectrum was parameterized with the 4-parameter function of Eqn. (3.12).
2. By minimizing the  $\chi^2$  between the values of the convolution integral and the data in the 18 bins, we found the values of the parameters of the true spectrum. This was done using the fit program MINUIT [77].
3. For this particular choice of parameters we then calculated the values of the true spectrum and the corresponding values of the smeared spectrum  $S$  (the values of the convolution integral). Ideally, the smeared spectrum should reproduce the data perfectly.
4. We defined the correction factor,  $K$ , by

$$K(m_{meas}) = \frac{S(m_{meas})}{T(m_{meas})} \quad (4.9)$$

and divide the data by  $K$  in order to get the unsmeared, fully corrected values

of the dijet mass distribution

$$\text{corrected data}(m_{meas}) = \frac{\text{data}(m_{meas})}{K(m_{meas})}. \quad (4.10)$$

In the following, we distinguish between the *true* and the *measured* dijet mass. Before we proceed with parameterizing the detector resolution function, we explain how the true and the measured distributions were defined.

### 4.3 True and Measured Dijet Masses

In order to relate the true and measured dijet masses to obtain  $R$  from Eqn. (4.8), we generated Monte Carlo events with the PYTHIA Monte Carlo program and, using a cone size of 0.7, clustered all final state particles into jets. The true dijet mass was then defined as the mass of all particles in the two leading jet cones, see Fig. 4.4a). Note that this was done at the parton level, before the detector simulation was applied. The measured dijet mass was defined as the mass of the same two jet cones after the detector simulation program, QFL<sup>1</sup>, was applied, see Fig. 4.4b).

### 4.4 True Level Clustering Routines

The handling of the true level clustering is crucial to this analysis since it affects the result of the unsmearing procedure as well as that of the internal consistency check. To ensure that this was done correctly, we have used two independent routines, PYTTOW and TRUECLUS. The two routines take independent approaches to perform the true level clustering.

---

<sup>1</sup>QFL is a detector simulation which uses parameterized detector responses instead of deriving them from detailed models, thus saving considerable CPU time.

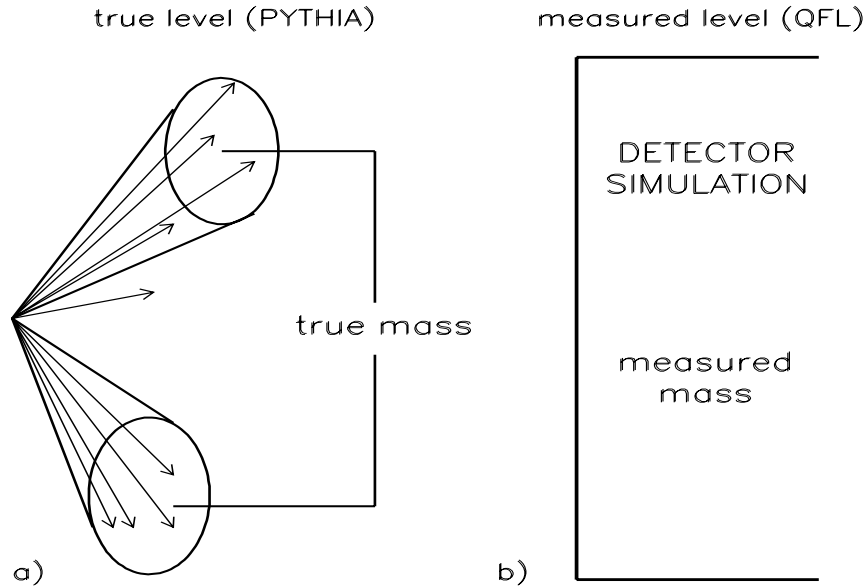


Figure 4.4: Definitions of the true and measured dijet masses: a) The true dijet mass is defined as the invariant mass of all final state PYTHIA particles in the two leading jet cones. b) The measured dijet mass is the mass of the same jet cones after the detector simulation.

PYTTOW uses the generator level particle information from PYTHIA to create data banks, on which the standard jet algorithm (JETCLU), can then be applied. The PYTTOW routine is part of the standard CDF offline software and has been used in previous analyses [13].

TRUECLUS was written specifically for this study. It was modeled after the JETCLU algorithm. Whereas JETCLU operates on calorimeter cells as input, TRUECLUS takes the PYTHIA 4-vectors as input and clusters them directly. TRUECLUS finds seeds, forms preclusters and merges jets in an iterative procedure, equivalent to the one in JETCLU.

Figure 4.5 shows a comparison of results from TRUECLUS and PYTTOW. The values of  $\eta$  and  $\phi$  from both routines are compared for the highest- $p_T$  jet in each event (Figs. 4.5a) and b)). Figures 4.5c) and d) show the fractional differences between the jet  $p_T$  of the two routines for two highest- $p_T$  jets.

The jets in these figures are unmatched. For example, in Fig.4.5a) the  $\eta$  of the

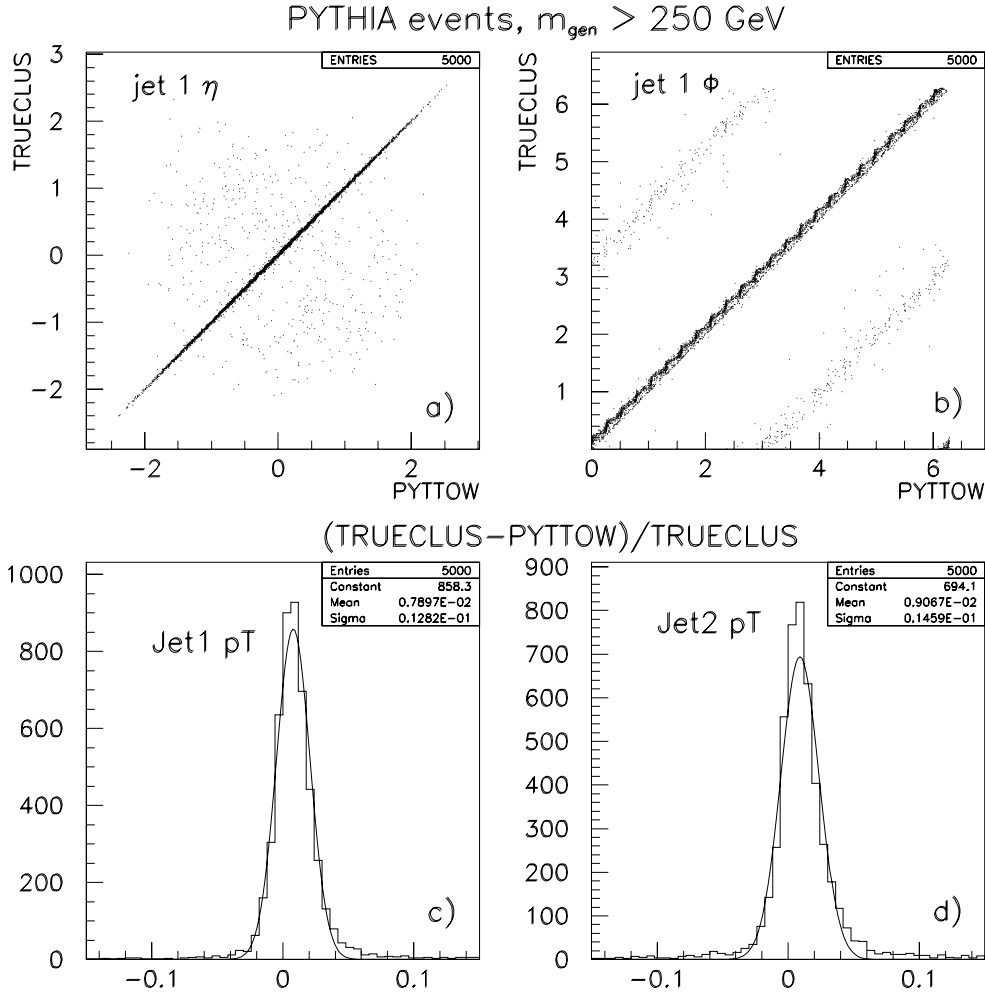


Figure 4.5: Comparison between the two true level clustering routines, TRUECLUS and PYTTOW. a) Detector  $\eta$  of jet 1 as measured by PYTTOW and TRUECLUS ( $x$  and  $y$ -axis, respectively). b) The same for  $\phi$ . c) and d) Fractional differences of the jet  $p_T$  for jet 1 and 2, respectively.

jet with the highest  $p_T$  in TRUECLUS is compared with the  $\eta$  of the highest- $p_T$  jet in PYTTOW. The fact that there was not necessarily a one-to-one correspondence between the jets can be seen in Fig. 4.5b): The bands above and below the central band correspond to events in which the two highest-energy jets were swapped between the routines. This happened in less than 10% of the events. It should be noted that the definition of the dijet mass does not depend on the  $p_T$ -order of the two highest jets. In less than 1% of the events a third jet in one routine was assigned as one of the

two highest jets in the other routine. Figures 4.5c) and d) show that the two routines are in good agreement, with the average difference in  $p_T$  being less than 1% for the two highest- $p_T$  jets. For the remainder of this analysis we used PYTTOW for the true level clustering, because it was computationally faster than TRUECLUS. Remaining differences between the two routines have no significant impact on the analysis, since we required the true-level jet  $p_T$ , on average, to reproduce the measured-level jet  $p_T$  (see below).

## 4.5 QFL Energy Scale Corrections

Before parameterizing the detector resolution function and performing the unsmearing, we ensured that the absolute energy scale in QFL was set correctly. The jet corrections were originally obtained with a version of QFL that is much older than the version used in this analysis<sup>2</sup>. The original version of QFL was checked extensively to ensure that it agreed with CDF test beam data and *in situ* calibration data. There have been many changes to the offline package and to QFL since these checks were done. It was therefore not necessarily true that the jet corrections were still valid for our version of QFL. In the past, a discrepancy between the true and measured level jet energies has been observed at least twice [13, 78], indicating that the QFL jet corrections were not up-to-date.

In order to re-establish the QFL energy scale, we repeated the study [66] that determined the jet energy corrections in the first place. Following this work, we used the PYTHIA program to generate a spectrum that was flat in the generated  $p_T$  of the jets. We then performed the jet clustering on the true and measured levels and plotted the fractional differences between the true and the measured jet  $p_T$  in 10 GeV-wide bins of measured jet  $p_T$ . This was done for the region of the Central Calorimeter only ( $0.2 < |\eta| < 0.7$ ). Single Gaussian functions were then fit to these histograms and the

---

<sup>2</sup>We used QFL version 3.59.

jet corrections were obtained by parameterizing the mean values of these Gaussians as a function of the measured jet  $p_T$ .

Our results are shown in Fig. 4.6 for six selected bins of measured jet  $p_T$ . In this figure true and measured jets are matched, as was done in [66]. The single Gaussian functions only describe parts of the distributions. However, this is what was done originally and our objective was to duplicate the original analysis, despite its limitations, to update the absolute energy scale of QFL.

The mean values of the single Gaussians as a function of the measured jet  $p_T$  and a third-order polynomial fit to these values are displayed in Fig. 4.7. It can be seen that the measured jet  $p_T$  is lower than its true counterpart by between 4% and 2%, depending on the jet  $p_T$ . In order to re-set the QFL energy scale, we added the amount indicated by the fit to each of the components of the measured 4-vectors of the jets. It should be stressed that this additional correction was applied to the jets in the Monte Carlo sample only; the data jets were not affected.

## 4.6 Parameterization of the Detector Response

In order to find a parameterization of the detector resolution function we generated several PYTHIA Monte Carlo samples. To obtain the detector response for a particular true dijet mass, we selected events with true dijet masses (PYTTOW) within 0.5% of the nominal mass, applied the detector simulation (QFL + JETCLU) and plotted the measured mass distribution. This distribution represented the response of the detector to dijets of a particular true dijet mass.

To parameterize the whole range of the dijet masses in our analysis, we selected six different true dijet masses, ranging from 50 to 1000 GeV/ $c^2$ . By fitting the measured mass distributions for each of the six samples, we determined the detector response for these input values of true mass. Figures 4.8 and 4.9 show the measured mass distributions of the Monte Carlo samples on a linear and a logarithmic scale, respec-

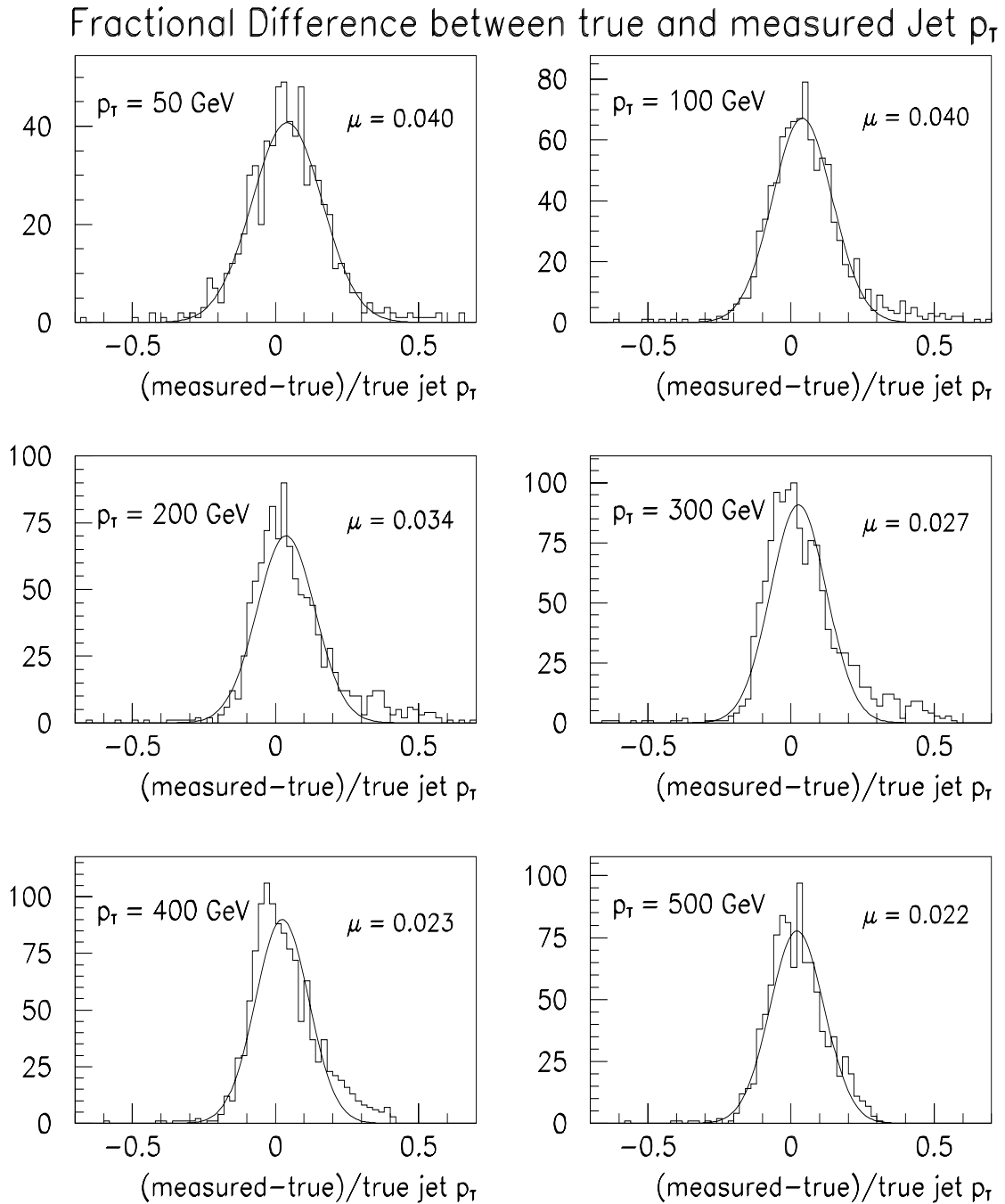


Figure 4.6: Single Gaussian fits to the fractional differences between the true and measured jet  $p_T$  for jets in the region  $0.2 < |\eta| < 0.7$ . The mean values,  $\mu$ , of the Gaussians are used to update the QFL energy scale.

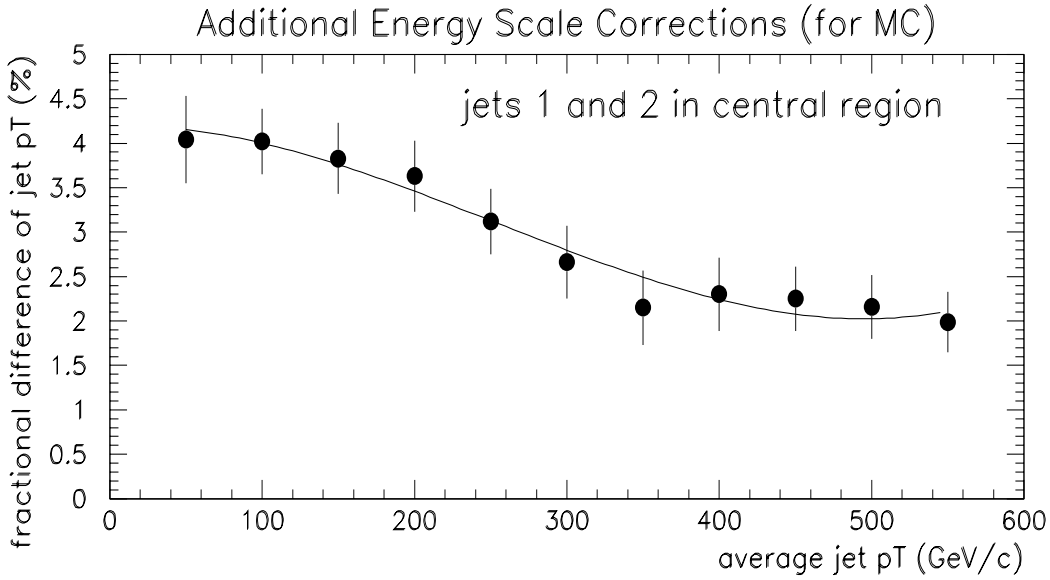


Figure 4.7: The mean values of the Gaussian functions from the fits to the fractional differences between the true and measured jet  $p_T$ . The solid line is a third-order polynomial fit. It indicates the additional correction (in %) that was added to the measured 4-vectors of the jets in order to re-set the QFL energy scale.

tively. Also shown in the two plots are fits of the parameterized detector response to the histograms. The parameterized detector response used in this fit is a sum of three Gaussian functions. Each individual Gaussian was normalized to unity and then multiplied with a relative weight  $n_i$ :

$$R(m_{true}, m_{meas}, X) = \sum_i \frac{n_i}{\sqrt{2\pi}\sigma_i} \exp \frac{-(\mu_i - m_{meas})^2}{2\sigma_i^2}, \quad i = 1, 2, 3, \quad (4.11)$$

where each of the nine parameters,  $\mu_i, \sigma_i$  and  $n_i$  was further parameterized as a function of true dijet mass according to

$$p = a m_{true}^2 + b m_{true} + c, \quad p = \mu_i, \sigma_i, n_i, \quad (4.12)$$

so that 27 parameters in total were used to parameterize the detector resolution.

The detector response histograms were normalized to unit area since the detector smears the dijet energies but does not create or destroy events, e.g. the integrated

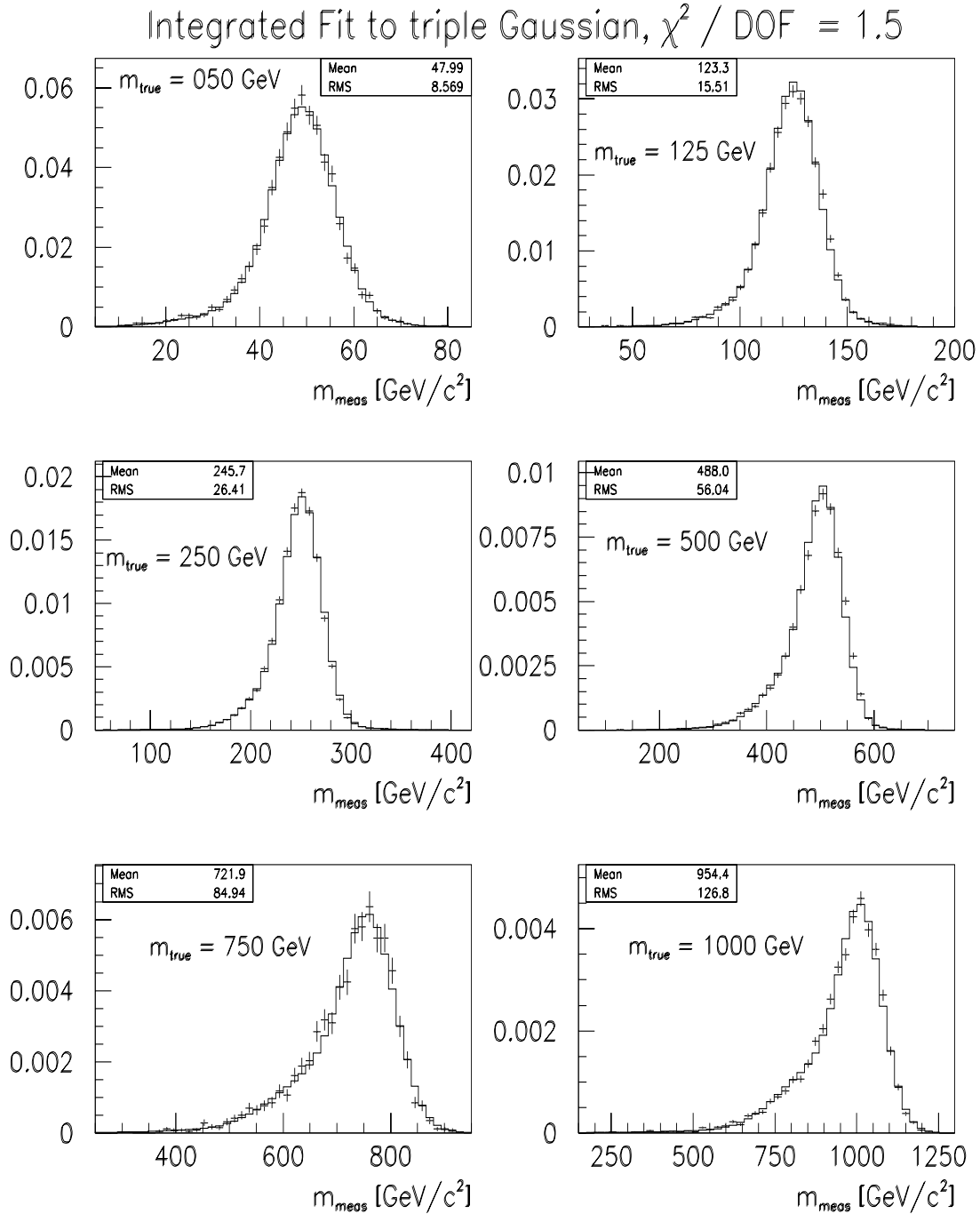


Figure 4.8: Detector responses to dijets with true masses of 50, 125, 250, 500, 750, and 1000 GeV/c<sup>2</sup>, respectively. The histograms are a fit of the parameterized detector resolution function used in the unsmearing procedure. All histograms are normalized to unit area.

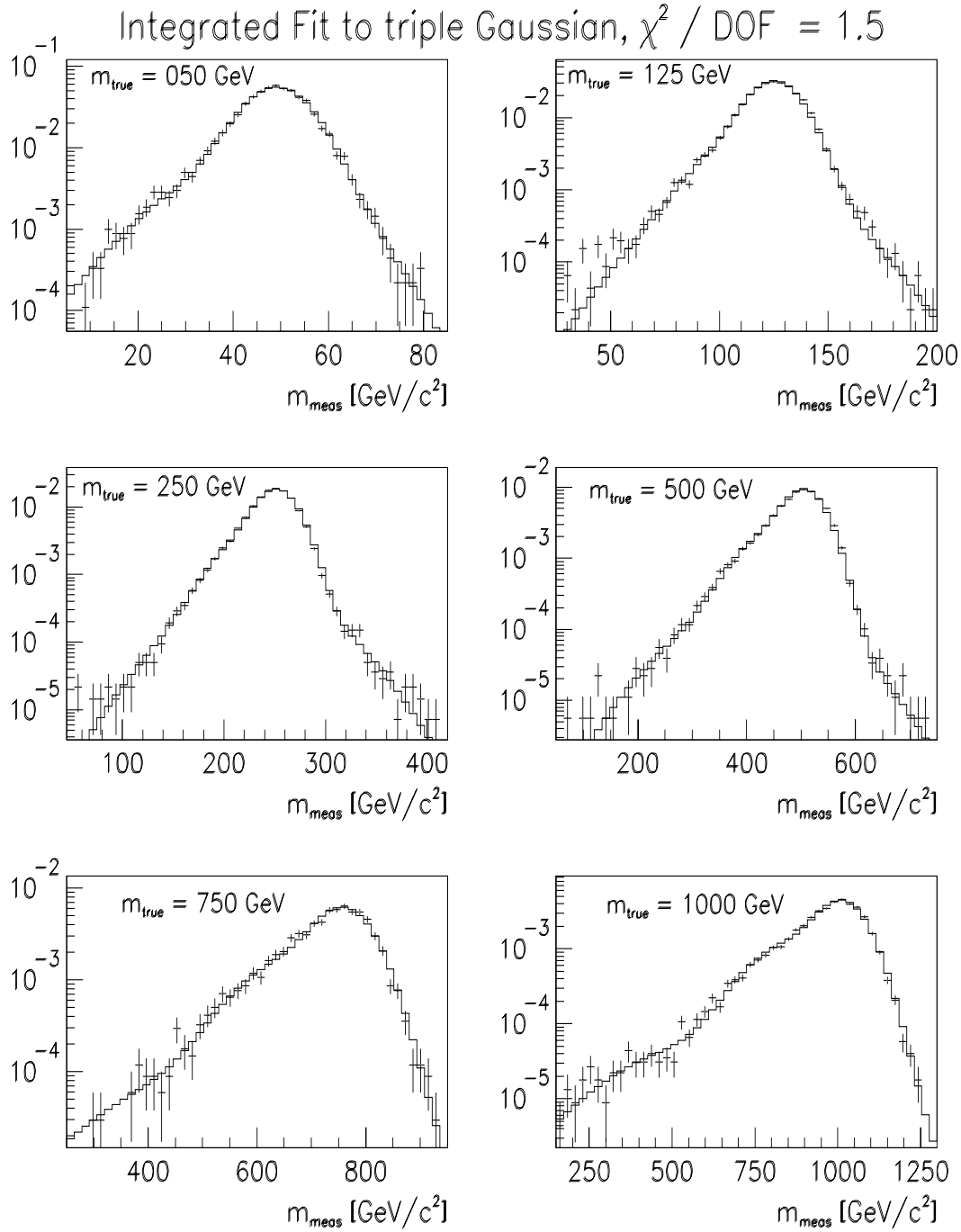


Figure 4.9: Detector responses to dijets. The information of the previous figure is shown on a logarithmic scale.

probability of finding a dijet of any given true mass at some measured mass had to be one. A simultaneous fit to all six histograms with a total of 278 non-zero entries was performed using MINUIT. The  $\chi^2$  of this fit was 365 / 251 DF or 1.45 / DF. The parameterized response reproduces both the high and low-end tails of the histograms. The low-end tails of the distributions are more pronounced at high masses. This can be explained by the fact that the jets are more collimated at higher energies, leading to a larger mismeasurement of the energies of jets that are detected in one of the crack regions, where the response of the detector is less well simulated.

In Fig. 4.10 the parameters of the detector resolution function are shown. As a result of the low-side tails at high masses, the relative mean value of the detector response function,  $\mu_{tot}/m_{true} \equiv (n_1\mu_1 + n_2\mu_2 + n_3\mu_3)/m_{true}$ , decreases slightly with the dijet mass. The dijet mass resolution,  $\sigma_{tot}/m_{true} \equiv (n_1\sigma_1 + n_2\sigma_2 + n_3\sigma_3)/m_{true}$ , of the detector improves from 11% for low dijet masses to about 8.5% for high masses (see Fig. 4.10b)). The definitions of  $\mu_{tot}$  and  $\sigma_{tot}$  have no impact on the physics of this analysis and are defined for illustrative purposes only. Figure 4.10c) shows the sum of the relative weights,  $n_{tot} \equiv n_1 + n_2 + n_3$ , of the three Gaussians. As required by the fitting procedure,  $n_{tot}$  is equal to one over the whole range of the dijet mass.

## 4.7 Results of the Unsmearing Procedure

Figure 4.11 shows the correction factor,  $K$ , the ratio of smeared and true distributions, as a function of the dijet mass. Considering the steepness of the differential cross section, the correction factor is rather flat, changing by less than 10% over the whole range of dijet masses.

The qualitative behavior of the correction factor can be explained by the increasing steepness of the dijet mass differential cross section. This increase can clearly be seen in Fig. 4.12, which shows the same data as Fig. 3.10, but plotted on a doubly-logarithmic scale. The dijet mass cross section falls approximately  $\sim 1/M_{jj}^6$  at the

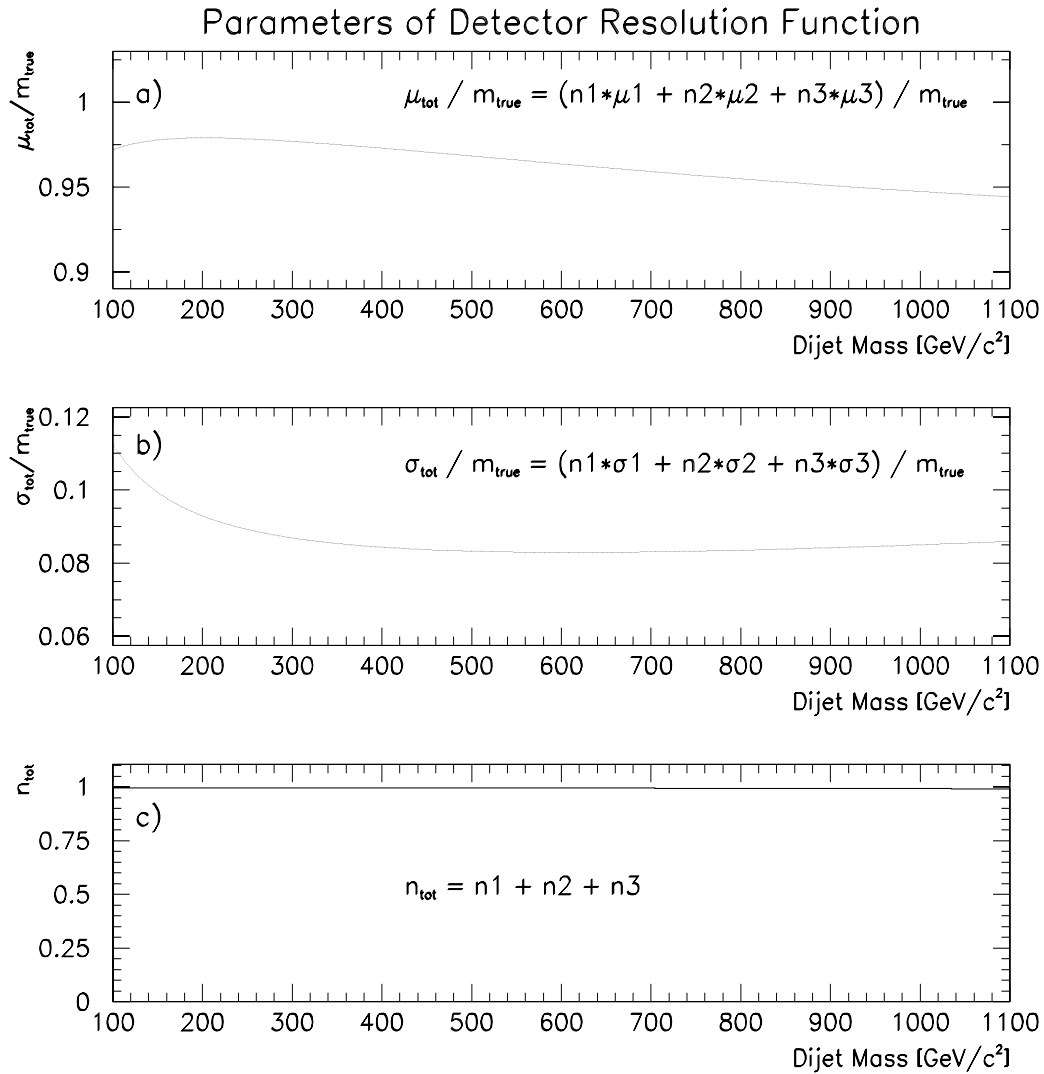


Figure 4.10: The parameters of the detector resolution function as a function of the dijet mass: a)  $\mu_{tot}/m_{true}$ , b)  $\sigma_{tot}/m_{true}$  and c)  $n_{tot}$ . The definitions of  $\mu_{tot}$  and  $\sigma_{tot}$  have no impact on the physics of this analysis and are defined for illustrative purposes only. The unsmearing procedure requires  $n_{tot}$  to be one.

low end of the measured spectrum and  $\sim 1/M_{jj}^{12}$  at the high end of the selected dijet mass range.

The  $\chi^2$ -minimization between the data and the values of the convolution integral (Eqn. (4.8)) returned a  $\chi^2$  of 20.1 / 14DF or 1.43 / DF. Graphical comparisons of the smeared spectrum and the data are shown in Fig. 4.13.

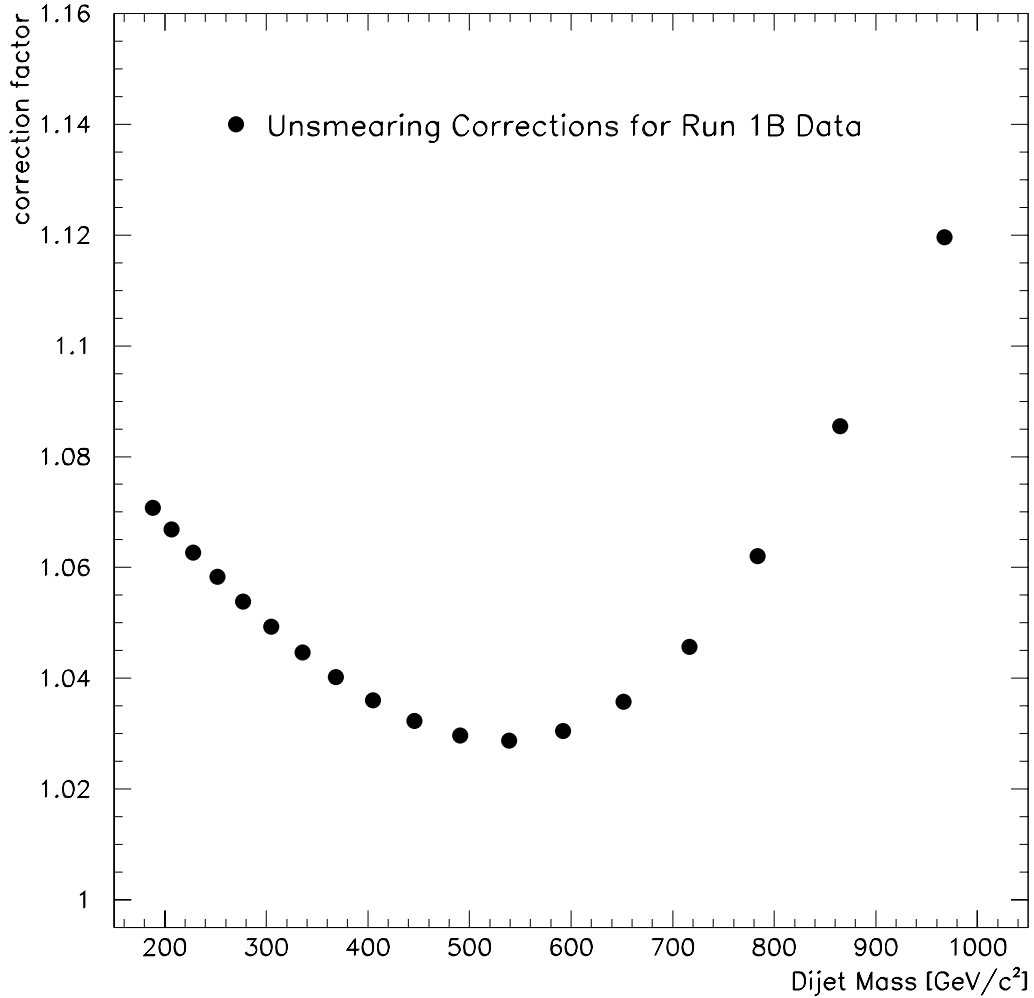


Figure 4.11: The unsmearing correction factor,  $K$ , the ratio of smeared and true distributions, as a function of dijet mass.

## 4.8 Check of the Unsmearing Procedure

To check the internal consistency of the unsmearing procedure, we compared the correction factors from the analytic unsmearing procedure with those obtained from an independent method, to which we refer to as the *Monte Carlo procedure*. The Monte Carlo procedure involves generating a full Monte Carlo dijet mass spectrum, using PYTHIA. With the definitions for the true and measured dijet mass of Section 4.3, we formed the true and measured dijet mass distributions and obtained the corrections

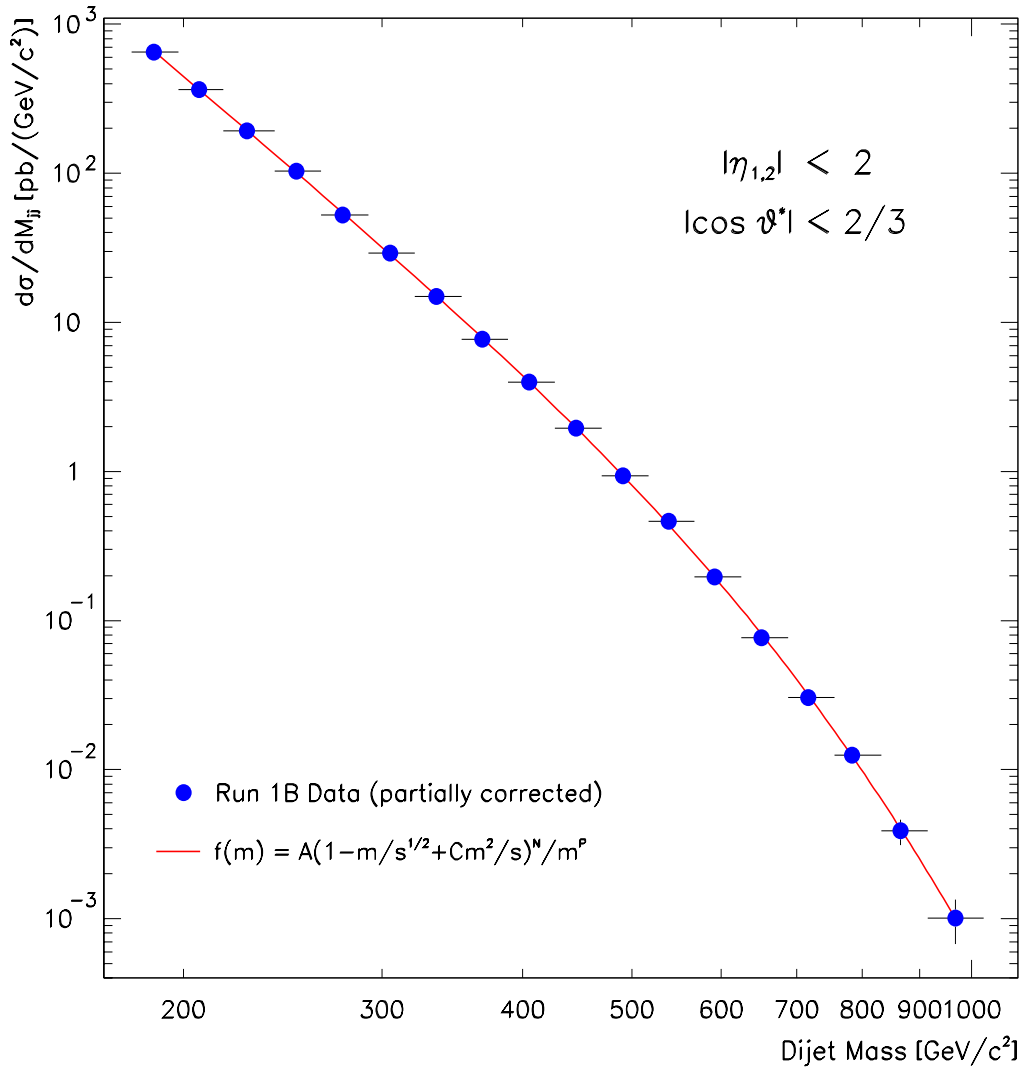


Figure 4.12: The partially corrected differential dijet mass cross section plotted on a doubly logarithmic scale. The steepness of the distribution increases with the dijet mass, leading to larger unsmearing corrections at higher dijet masses.

factors by comparing the cross sections of the two distributions as a function of the dijet mass.

#### 4.8.1 Efficiencies of the Monte Carlo Samples

The kinematical range of the PYTHIA events is controlled by minimum values for the generated dijet mass,  $m_{gen} \equiv \hat{s}$ , and the generated transverse momentum of

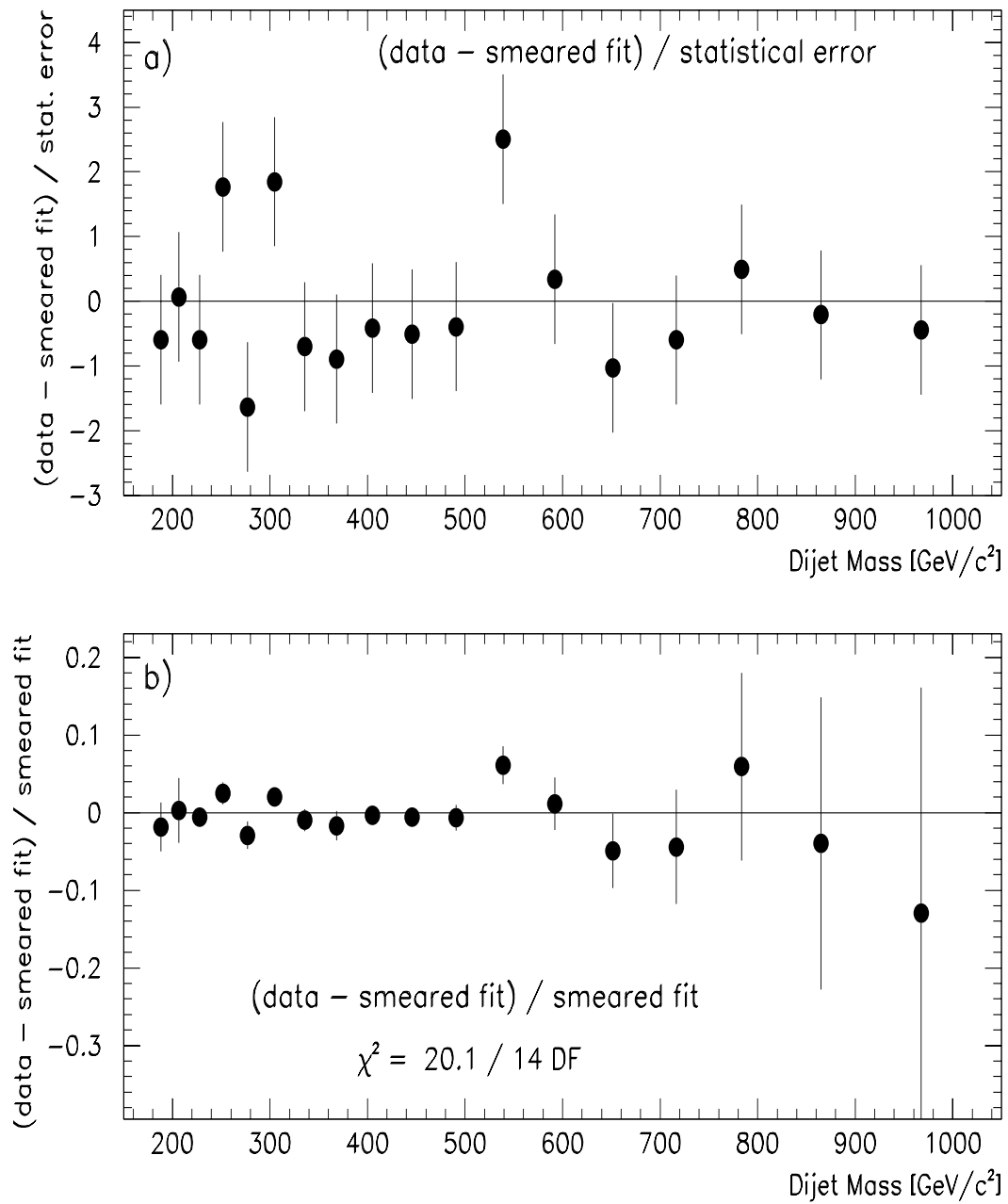


Figure 4.13: Comparison of the smeared fit to the data. a) Residuals of the fit  $(\text{data} - \text{smeared fit}) / (\text{statistical uncertainty})$ . The error bars are of unit length in terms of the statistical uncertainties. b) Fractional differences between the data and the smeared fit  $((\text{data} - \text{smeared fit}) / \text{data})$ . The error bars represent statistical uncertainties only.

the events. Due to the steepness of the dijet mass cross section, the Monte Carlo distributions used could not be generated in one sample. Instead, combined seven subsamples, each starting at a higher generated mass than the next-lower one, to form the complete distributions, similar to the data sample, which is built up from four different jet triggers. The simulated samples start at generated masses of 70, 100, 150, 210, 275, 360 and 450 GeV/c<sup>2</sup>, respectively. Except for different generated mass cuts these samples were identical. Care was taken when the subsamples were combined to reconstruct the full sample to ensure that each was fully efficient in the dijet mass range for which it was used. Since the true and the measured distributions were to be constructed, we ensured that the selection criteria were fully efficient for both. Figures 4.14 and 4.15 show the efficiencies of the true and measured distributions. The sample starting at a generated mass of 50 GeV/c<sup>2</sup> was used exclusively to measure the efficiency of the 70 GeV/c<sup>2</sup> sample.

### 4.8.2 True and Measured Monte Carlo Distributions

The reconstructed distributions, built up from the seven subsamples (Fig. 4.16), shows the fractional differences between the Monte Carlo distributions and the 4-parameter function of Eqn.(3.12). These plots show that the reconstructed distributions are smooth and that remaining inefficiencies in the subsamples are small. The error bars represent the statistical uncertainties only.

Whereas the fit of the 4-parameter function to the measured level cross section is good ( $\chi^2/\text{DF} = 1.0$ ), the fit to the true level cross section returns a higher value of  $\chi^2/\text{DF} = 1.8$ . We believe that the imperfect fit is due to residual inefficiencies in the Monte Carlo subsamples, which could, in principle, be removed by generating larger Monte Carlo samples. However, the existing sample required the generation of about  $10^7$  events. Considering the fact that these samples are used as a consistency check of the analytic unsmearing procedure only, we consider the quality of the fits to be sufficiently high.

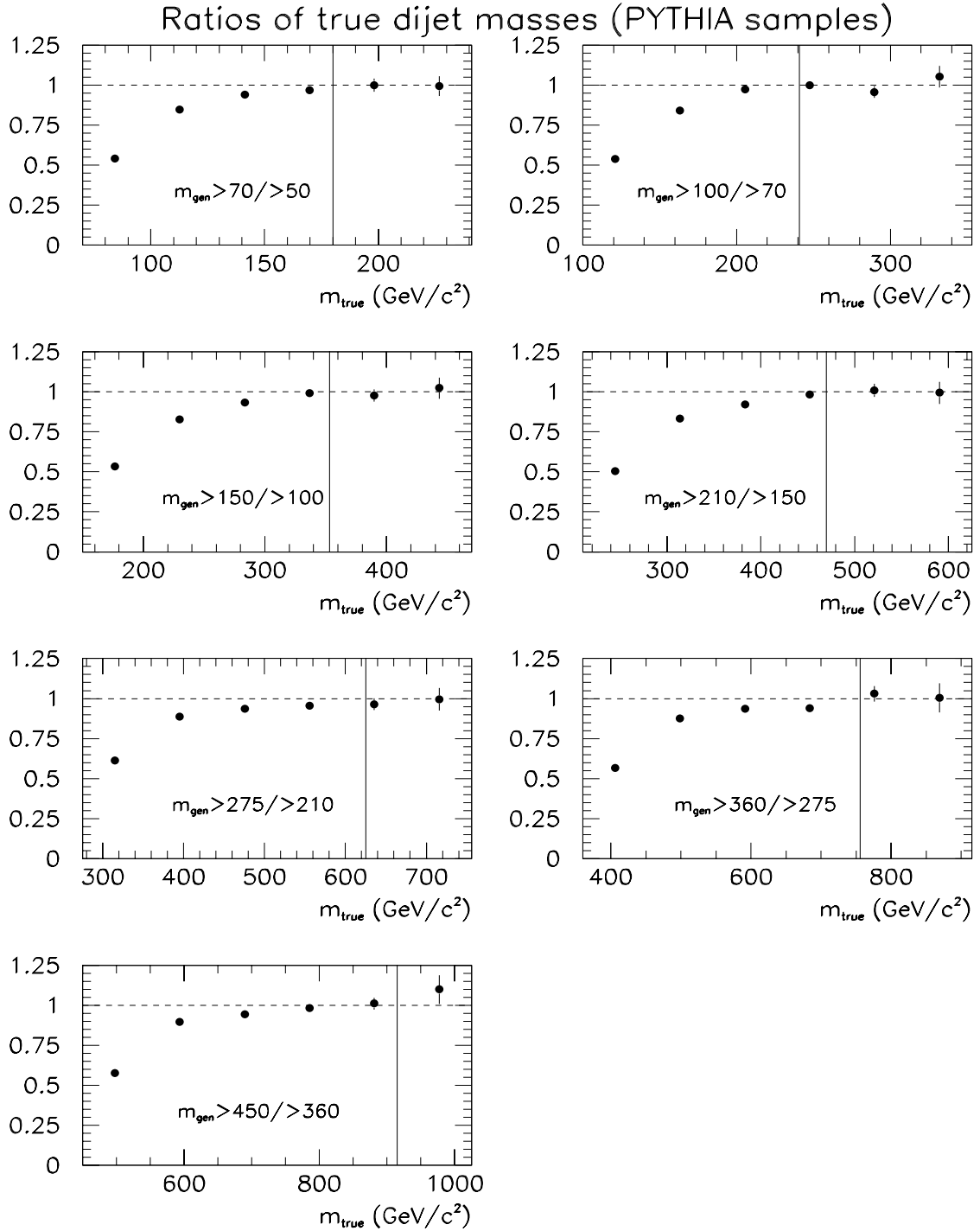


Figure 4.14: The true dijet mass efficiencies of the Monte Carlo samples, used to form the full Monte Carlo distributions. Shown are the ratios of the cross sections of each of the subsamples and the next-lower sample. The vertical lines indicate the dijet mass above which a particular sample was used to build up the full distribution. The range of a particular sample ends where the next one begins.

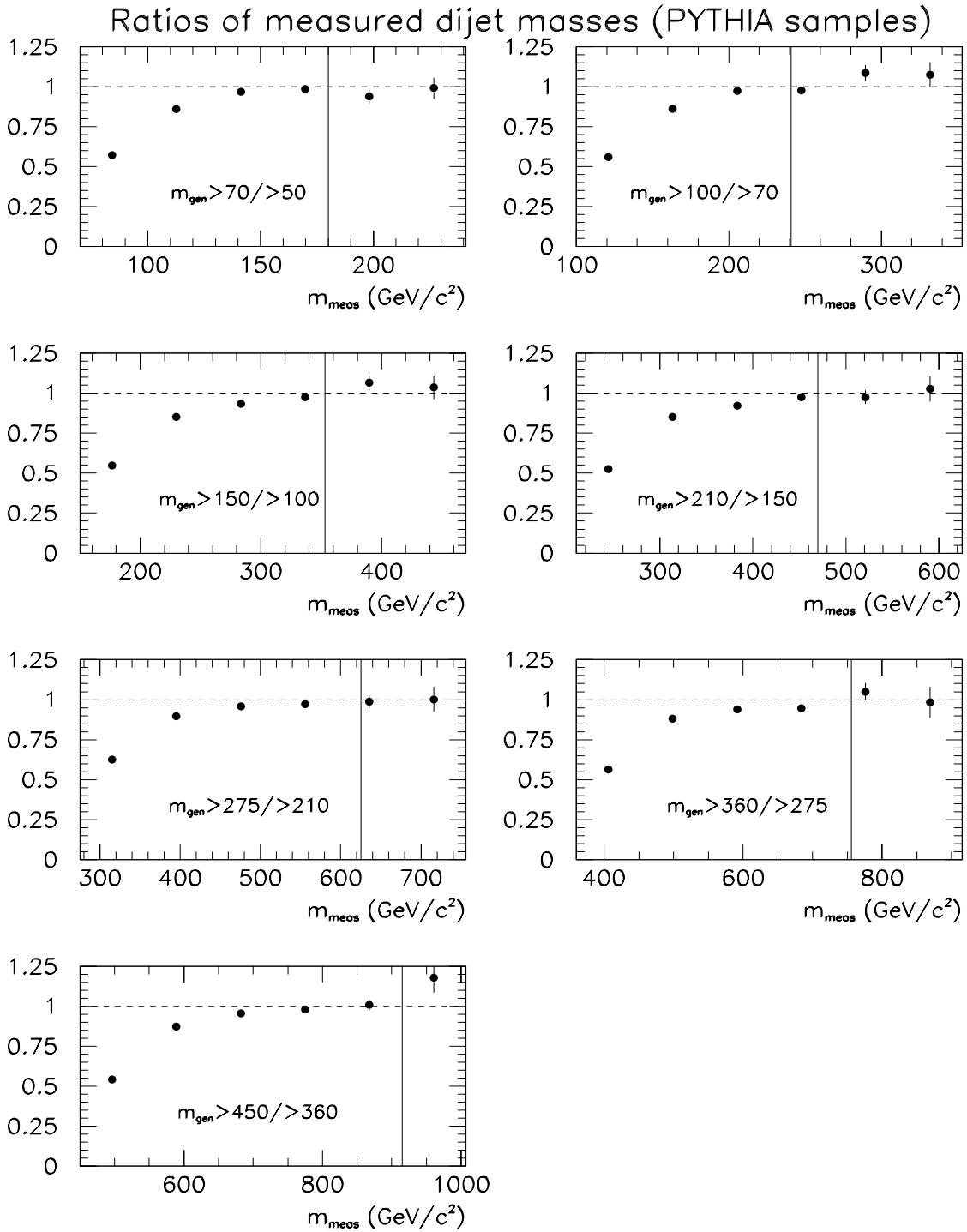


Figure 4.15: The measured dijet mass efficiencies of the Monte Carlo samples that were used to form the full Monte Carlo distribution.

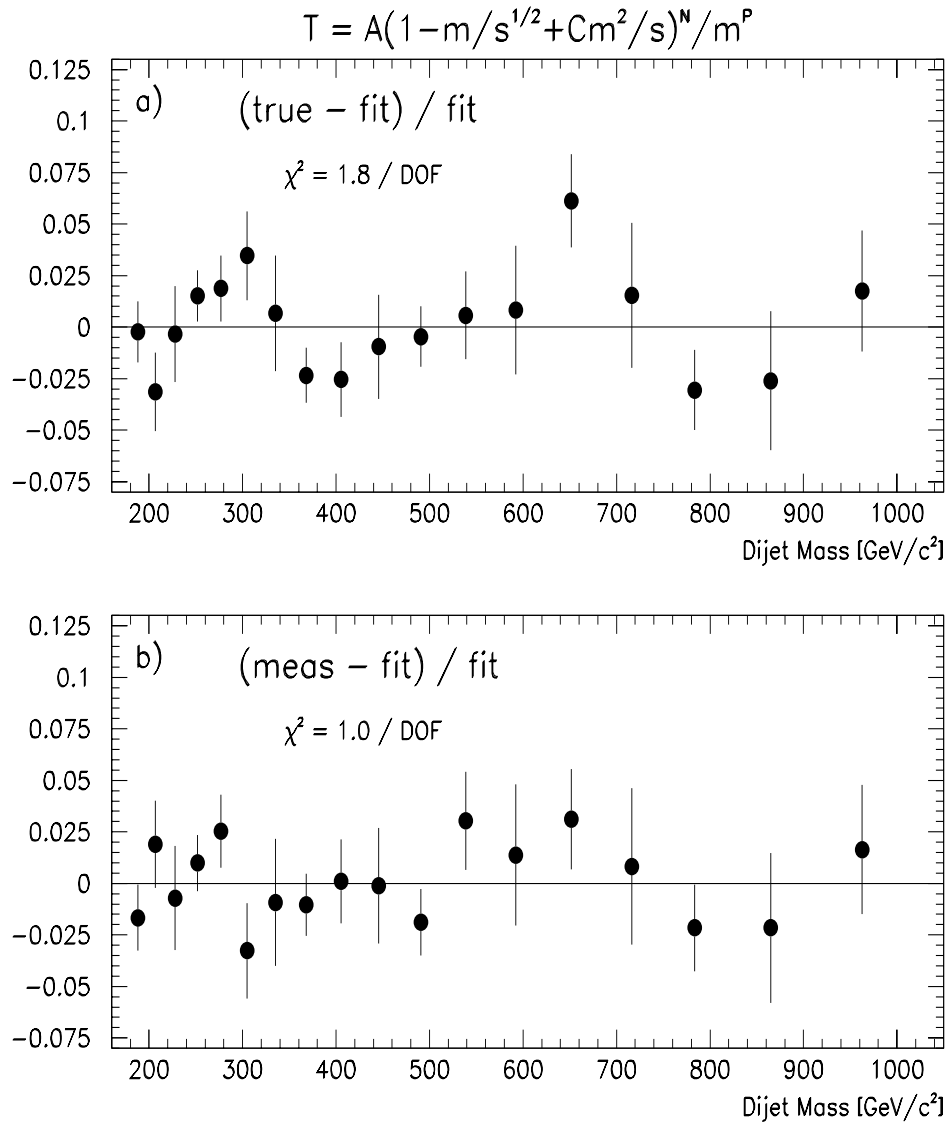


Figure 4.16: The full Monte Carlo distributions. Plotted are the fractional differences between the 4-parameter function, which was used to parameterize the data, and the Monte Carlo cross sections. a) True level b) Measured level.

### 4.8.3 Results of the Consistency Check

The result of the internal consistency check is shown in Figs. 4.17 and 4.18. Figure 4.17 shows a comparison of the correction factors from the analytic method (applied to the Monte Carlo sample) with the ones from the Monte Carlo method, the ratios of the cross sections in the mass bins on the measured and the true level. The solid

line is a polynomial fit to the Monte Carlo data points, which is used as an estimate of the systematic uncertainty of the unsmearing procedure.

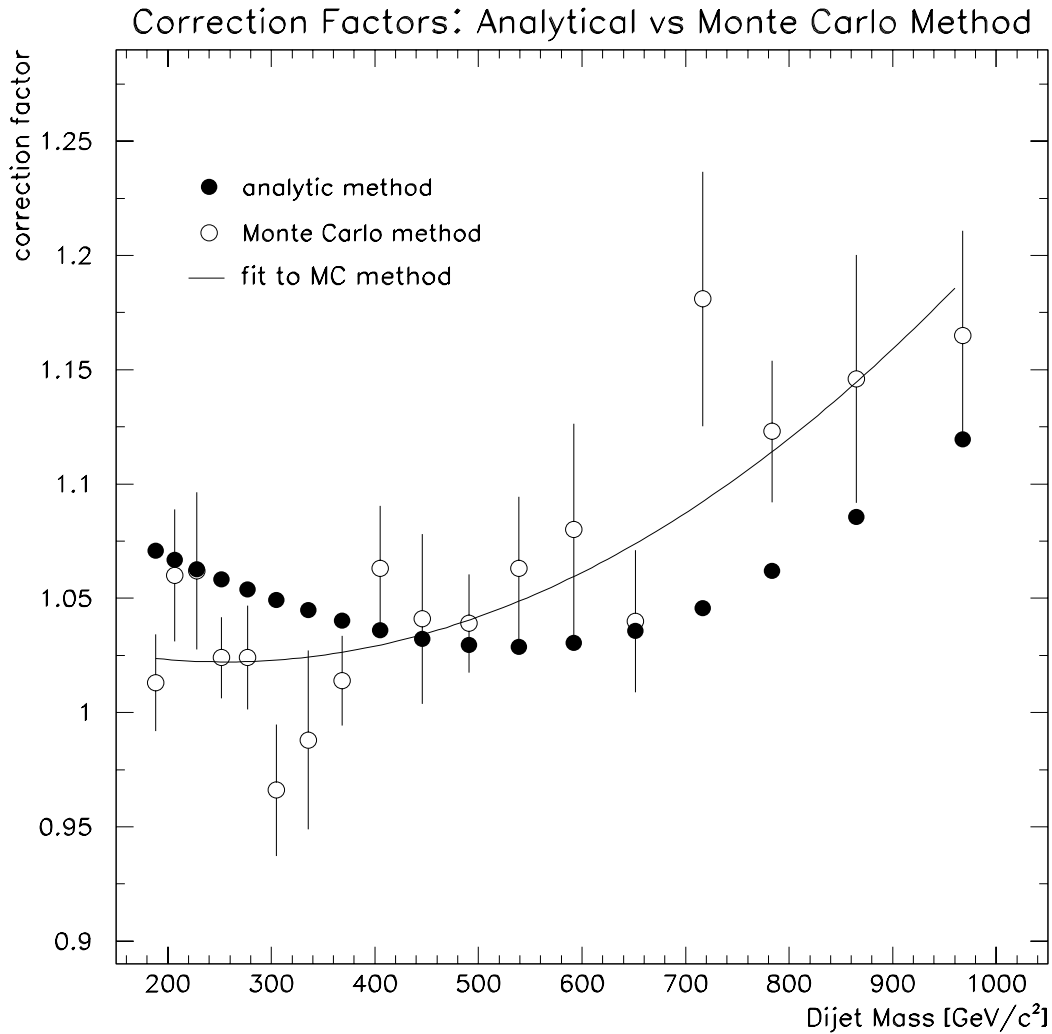


Figure 4.17: Comparison of the correction factors from the analytic method (full circles) and the Monte Carlo method (open circles). The solid line is a smooth fit to the Monte Carlo data points, which is used as an estimate of the systematic uncertainty.

Another way of looking at the same data is to plot a comparison of the true Monte Carlo distribution with the analytically unsmearred measured distribution, which is shown in Fig.4.18. In principle, the two distributions should be identical. Given the imperfect input true distribution (Fig.4.16a)), the agreement between the two methods is good and we conclude that the analytic unsmearing procedure is internally

consistent. Differences between the two methods will be quantified in Section 5.2.2.

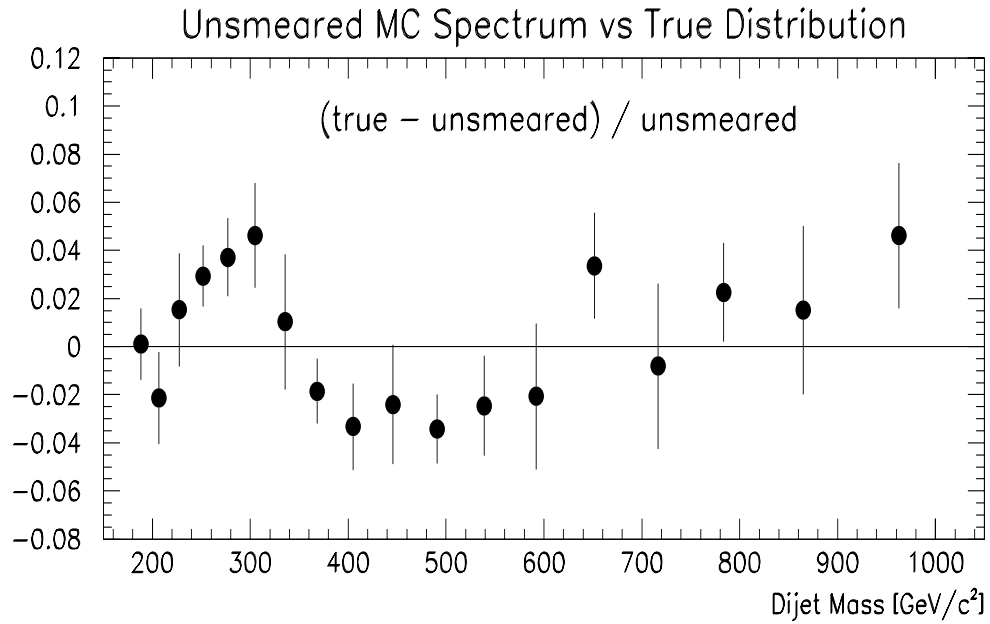


Figure 4.18: Fractional differences between the true Monte Carlo distribution and the analytically unsmeared Monte Carlo cross section.

# Chapter 5

## Systematic Uncertainties

In this Chapter we will discuss the systematic uncertainties on the fully corrected dijet mass cross section. We treat uncertainties on the cross section measurement and the unsmearing procedure separately.

### 5.1 Uncertainties on the Cross Section

We consider six sources of systematic uncertainty associated with the measurement of the dijet mass cross section: the absolute energy scale, the relative ( $\eta$ -dependent) energy scale, the integrated luminosity, the relative normalizations of the jet triggers, the  $z$ -vertex cut efficiency and the trigger efficiency.

#### 5.1.1 Absolute Jet Energy Scale

The absolute energy scale is by far the largest source of systematic uncertainty on the dijet mass cross section. We identify four components that all contribute individually [79].

##### 1. The Absolute Energy Calibration

This is the uncertainty on the response of the central calorimeter to single pions.

Two sources contribute to this uncertainty. The first is our ability to properly model the variation of the single-pion response over the face of a calorimeter tower. The second is from the agreement of test beam and *in situ* calibrations for pions of the same momentum, which provides a check of the reproducibility of the energy scale calibration. The resulting high-side (low-side) uncertainty on the transverse energy of the jets decreases from 1.8 % to 1.7% (1.6 % to 1.3 %) with increasing jet  $E_T$ .

## 2. The Jet Fragmentation Model

Because the calorimeter response to charged hadrons is not perfectly linear at low energies, the observed jet energy is a function not only of the incident parton energy but also of the momentum spectrum of the particles produced in the fragmentation process. Therefore, the response of the calorimeter varies, depending on the details of the jet fragmentation model that was used in the simulation. This uncertainty is slightly asymmetrical as well, with high and low-side uncertainties decreasing from 1.7% to 1.2% with increasing jet  $E_T$ .

## 3. The Stability of the Calorimeter with Time

Variations in the response of the central calorimeter with time were estimated to be 1% of the jet energy [80], independent of the energy.

## 4. The Underlying Event Corrections

The underlying event is the ambient energy produced in hadron collisions associated with the soft interactions of spectator partons. The energy from the underlying event will increase the energy found in the jet cone. In this analysis, the underlying event energy was subtracted from the jet energy. The uncertainty associated with the energy from the underlying event was estimated to be 1 GeV of the jet  $E_T$ . Taking the average angle between the jets in the dijet system into account, this corresponds to an uncertainty on the dijet mass of 2.2 GeV.

In order to get an upper (lower) limit on the dijet mass cross section, we added (subtracted) the  $1\text{-}\sigma$  value for each of the four uncertainties from the jet 4-momentum and re-computed the differential cross section in each case. As the high-side and low-

side uncertainties on the dijet mass cross section, we took the differences between the central value and the upper and lower limits, respectively. Figure 5.1 shows the uncertainties on the dijet mass cross section, due to the uncertainties on the absolute energy scale. The contributions from the four sources are shown separately.

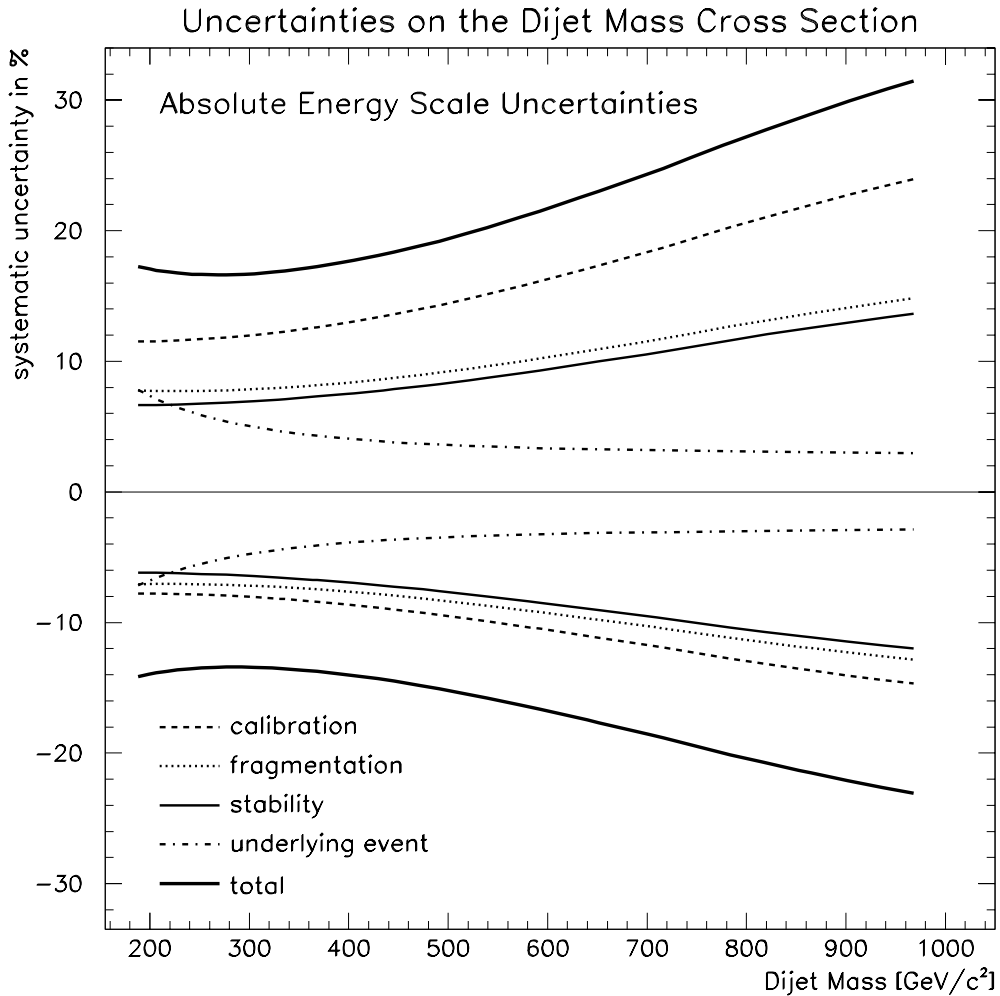


Figure 5.1: The systematic uncertainties on the dijet mass cross section, due to uncertainties on the absolute energy scale, broken down into the components: calibration (dashed), fragmentation (dotted), stability (thin solid), underlying event (dash-dotted) and total (thick solid). The uncertainties shown were obtained by using the parameterization of the data.

These uncertainties were obtained using the parameterization of the data. When the data themselves were used, values for the uncertainties were in the same range, but included large bin-to-bin variations, due to the statistical fluctuations in the data.

The uncertainties on the dijet mass cross section were much larger than the uncertainties on the jet energies themselves, because of the steepness of the dijet mass spectrum. The total absolute energy scale uncertainties, the squared sum of the four individual contributions, range from  ${}^{+17}_{-14}\%$  for low masses to  ${}^{+32}_{-24}\%$  for high masses. It should be noted that this large uncertainty on the cross section is a result of uncertainties on the transverse jet energies of at most 2.6%. The increase of the systematic uncertainty with the dijet mass is due to the increasing steepness of the differential dijet mass cross section (see Fig. 4.12).

### 5.1.2 Relative Jet Energy Scale

In addition to the uncertainty on the absolute jet energy scale, we assigned additional uncertainties associated with the detector response as a function of  $\eta_d$ . These uncertainties were estimated using the method of *dijet balancing* [81], a procedure that uses events with exactly two jets where at least one jet was detected in the central region. Momentum conservation requires that the two jets in a dijet are back-to-back to balance the transverse momentum of the event. By comparing the energies of the two jets, the detector response as a function of  $\eta_d$ , with respect to the central region, was determined. The jet resolutions in the crack regions were typically 30 – 50% worse than in the central calorimeter [82].

In order to establish the relative uncertainties on the jet energies, we identified three regions of the detector where we assigned uncertainties in addition to the absolute energy scale uncertainties:

- the ninety degree crack ( $|\eta_d| < 0.15$ ),
- the thirty degree crack ( $0.9 < |\eta_d| < 1.4$ ) and
- the Plug Calorimeter ( $|\eta_d| > 1.4$ ).

Depending on the dijet invariant mass and the region of  $\eta_d$ , we assign the symmetrical uncertainties of Table 5.1 to the jet energies.

	$ \eta_d  < 0.15$	$0.9 <  \eta_d  < 1.4$	$ \eta_d  > 1.4$
$M_{jj} < 517 \text{ GeV}/c^2$	3%	4%	2%
$M_{jj} > 517 \text{ GeV}/c^2$	6%	4%	2%

Table 5.1: The relative jet energy scale uncertainties.

For each region, we changed the 4-momentum of any jet in that region by the amount specified in Table 5.1 and recorded the resulting change in the differential cross section. The total uncertainty on the cross section from the  $\eta$ -dependent uncertainties ranges from 5% (9%) for dijet masses of 230  $\text{GeV}/c^2$  (970  $\text{GeV}/c^2$ ).

### 5.1.3 Integrated Luminosity and Trigger Normalizations

The luminosity at CDF was measured by two sets of scintillation counters, one set upstream and one set downstream from the interaction point. The coincidence rate of the two sets was proportional to the luminosity and its uncertainty was mainly due to the uncertainty on the cross section of the counters. We assign an uncertainty on the integrated luminosity of 4.1%, the value quoted by the most recent study of the luminosity [83], independent of the dijet mass.

In addition to the uncertainty on the luminosity, we assigned uncertainties on the relative normalizations of the jet triggers. These uncertainties were given by the statistics in the overlap region where the trigger prescale factors were measured. Using the Jet 100 trigger (which was not prescaled) as our reference trigger, we assign uncertainties of 3.5, 1.7 and 1.9% to the relative normalizations of the Jet 20, Jet 50 and Jet 70 trigger samples, respectively.

### **$z$ -Vertex Cut and Trigger Efficiencies**

In Fig. 3.6 we plotted the  $z$ -vertex cut efficiency as a function of the dijet mass. Based on this figure we estimate the uncertainties associated with the  $z$ -vertex cut efficiency to be 1%. Given the size of the other systematics, this uncertainty was disregarded.

Uncertainties on the trigger efficiency were determined by the statistics in the onset regions of the jet triggers. These uncertainties are estimated to be lower than 1% and were also neglected.

## **5.2 Uncertainties on the Unsmearing Corrections**

We consider three sources of systematic uncertainty that are associated with the unsmearing procedure: our description of the tails of the detector resolution function, the differences between the analytic and the Monte Carlo procedure and the size of the additional energy corrections that we assigned to re-establish the QFL energy scale.

### **5.2.1 Parameterization of the Detector Resolution**

In order to estimate the systematic uncertainty due to our imperfect knowledge of the tails of the detector resolution, we approximated the detector resolution with single Gaussian functions and repeated the unsmearing procedure. The fit of the simpler function to the detector response histograms is shown in Fig. 5.2. This fit reproduces the core of the detector response but does not fit the tails of the distributions well.

The resulting correction factors for the single Gaussian parameterization of the detector response are shown in Fig. 5.3. The difference between the correction factors from the two different parameterizations ranges from 1% at the low end to about 9% at the high end. The differences between the single Gaussian fit and our default analysis is bigger at high masses because the single Gaussian fit overestimates the

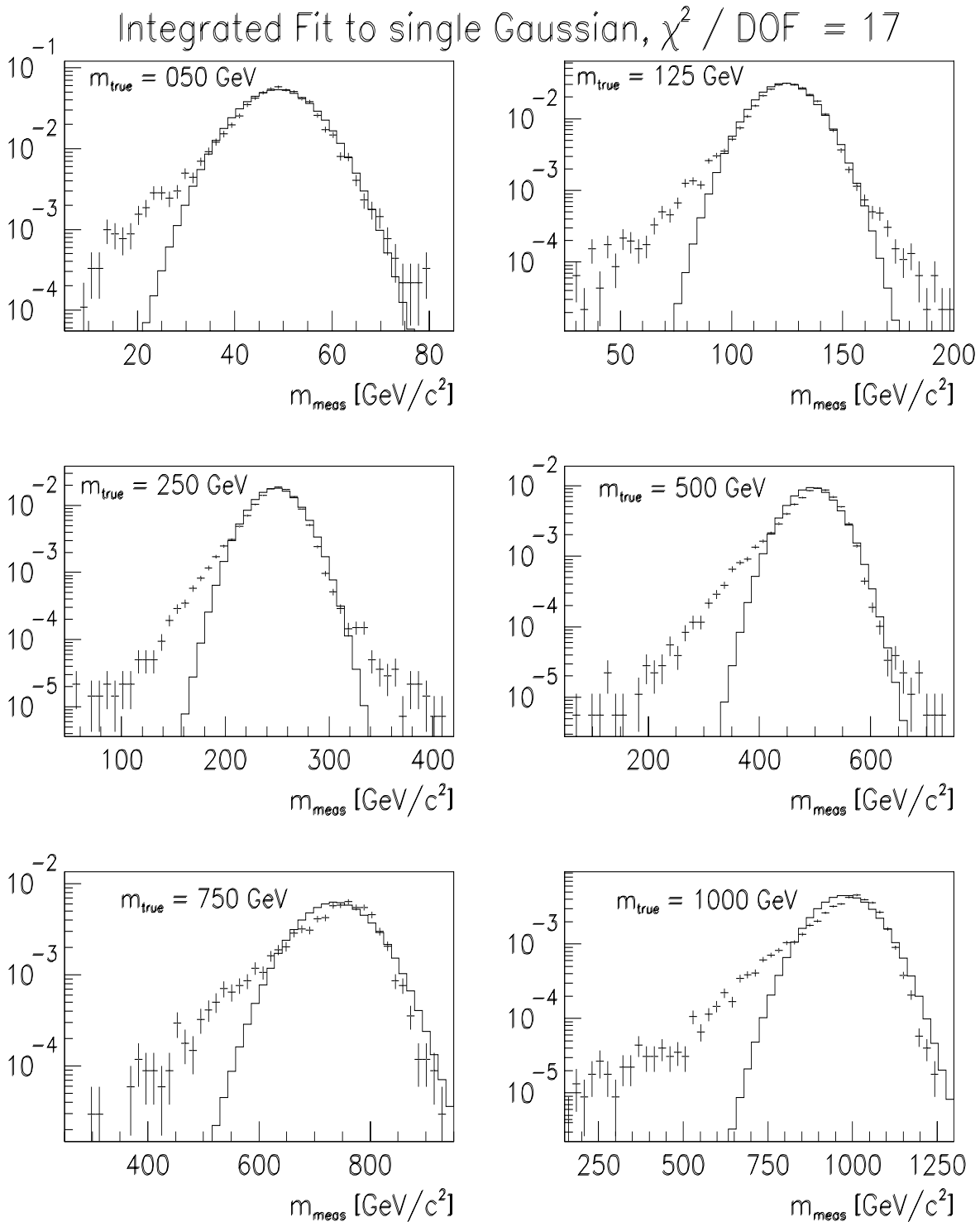


Figure 5.2: The fit of a single Gaussian function to the detector response histograms. This simpler fit, used for systematic uncertainty determination, reproduces the core of the detector response but does not fit the tails of the distributions well.

high-end tail of the detector response at high masses, leading to a larger smearing effect. We conservatively assigned a smoothly varying symmetrical uncertainty to the dijet mass cross section that ranged from  $\pm 1\%$  for low dijet masses to  $\pm 9\%$  for the highest mass bin.

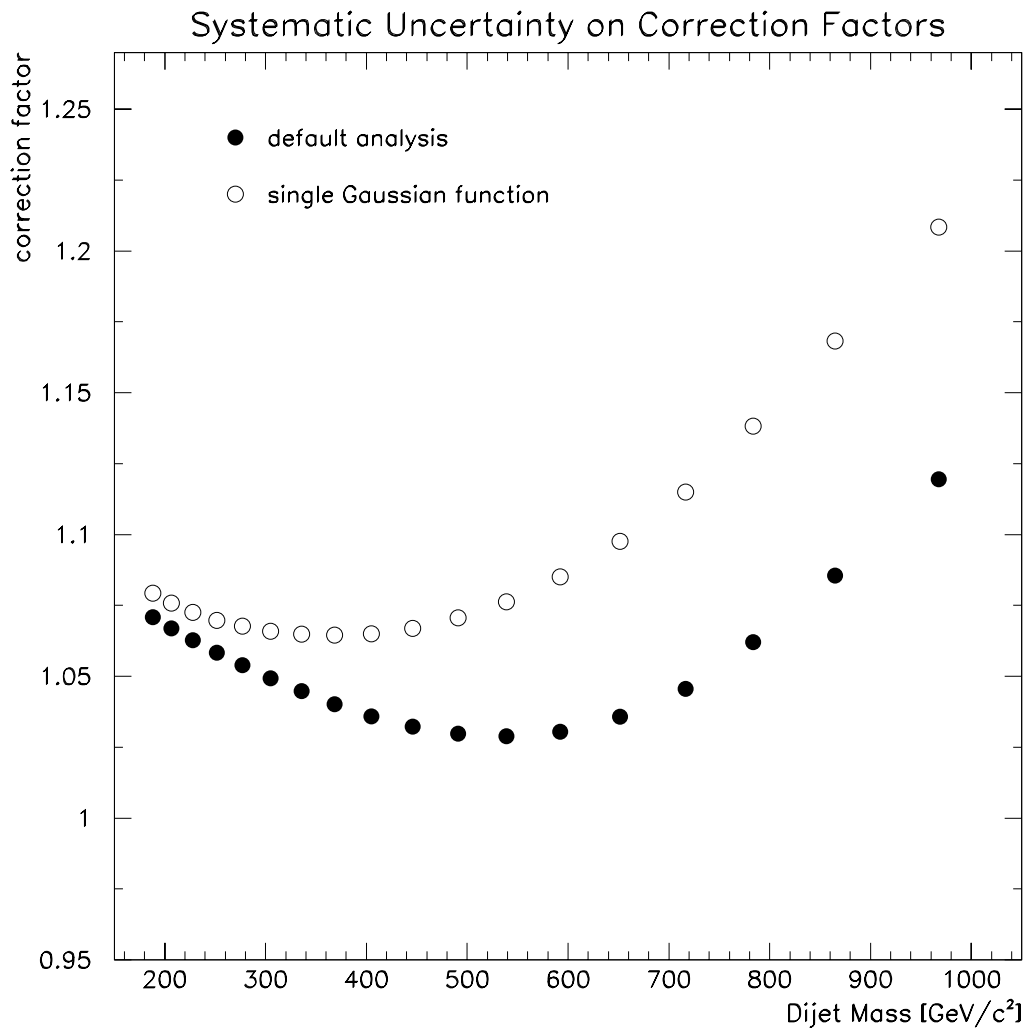


Figure 5.3: The unsmearing correction factors from the central analysis (full circles), compared to the ones obtained from the single Gaussian fit (open squares). The difference between the correction factors from the two different parameterizations ranges from 1 to 9%.

### 5.2.2 Difference between the Analytic and MC Procedure

The correction factors from the analytic procedure and the Monte Carlo method were shown in Fig. 4.17. The difference between the smooth curve and the values from the analytic method are at most 4%. We conservatively assigned a symmetrical, mass independent uncertainty of  $\pm 4\%$  to the dijet mass cross section.

### 5.2.3 QFL Energy Scale Corrections

In order to estimate the systematic uncertainty associated with the additional corrections that were applied to re-set the QFL energy scale, we varied these corrections by the size of their statistical uncertainties. Figure 5.4 shows the corrections along with the variations of plus and minus the statistical uncertainty of the default corrections. The changes of the unsmearing factors with the variation of the energy scale corrections are shown in Fig. 5.5. We assign a systematic uncertainty, ranging from  $^{+2}_{-4}\%$  for low masses to  $^{+2}_{-8}\%$  for high masses. Note that negative changes in the correction factor correspond to positive changes in the dijet mass cross section.

## 5.3 Combined Systematic Uncertainties

The systematic uncertainties on the dijet mass cross section are shown in Fig. 5.6. We assume the individual components to be independent. The total systematic uncertainty is therefore given by the squared sum of the individual uncertainties. For presentation purposes the three uncertainties associated with the unsmearing procedure were combined into one. Similarly, we combined the uncertainties on the integrated luminosity and the relative jet trigger normalizations. The absolute jet energy scale uncertainties dominate over the whole dijet mass range. The overall systematic uncertainty ranges from  $^{+19}_{-17}\%$  for low masses to  $^{+34}_{-28}\%$  for the highest dijet mass bin.

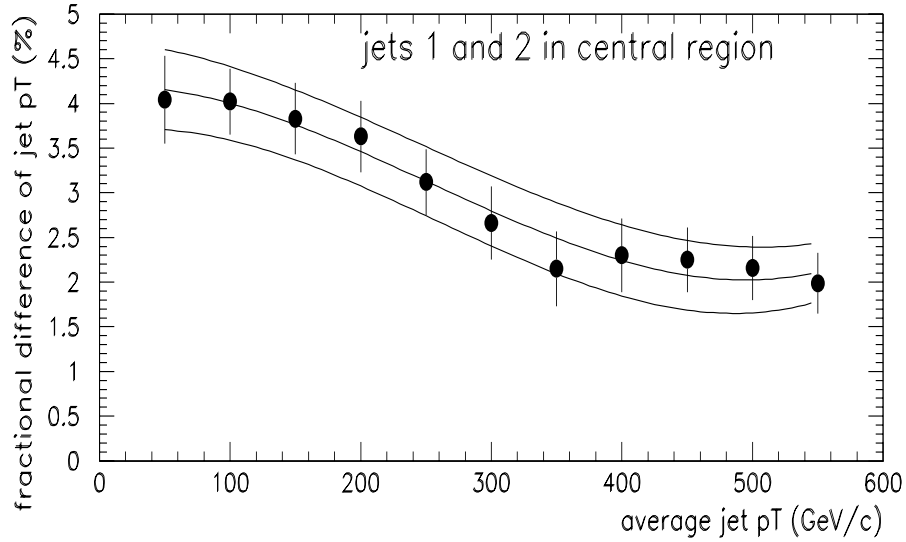


Figure 5.4: The additional corrections to the QFL energy scale and  $1\text{-}\sigma$  variations of the statistical uncertainty.

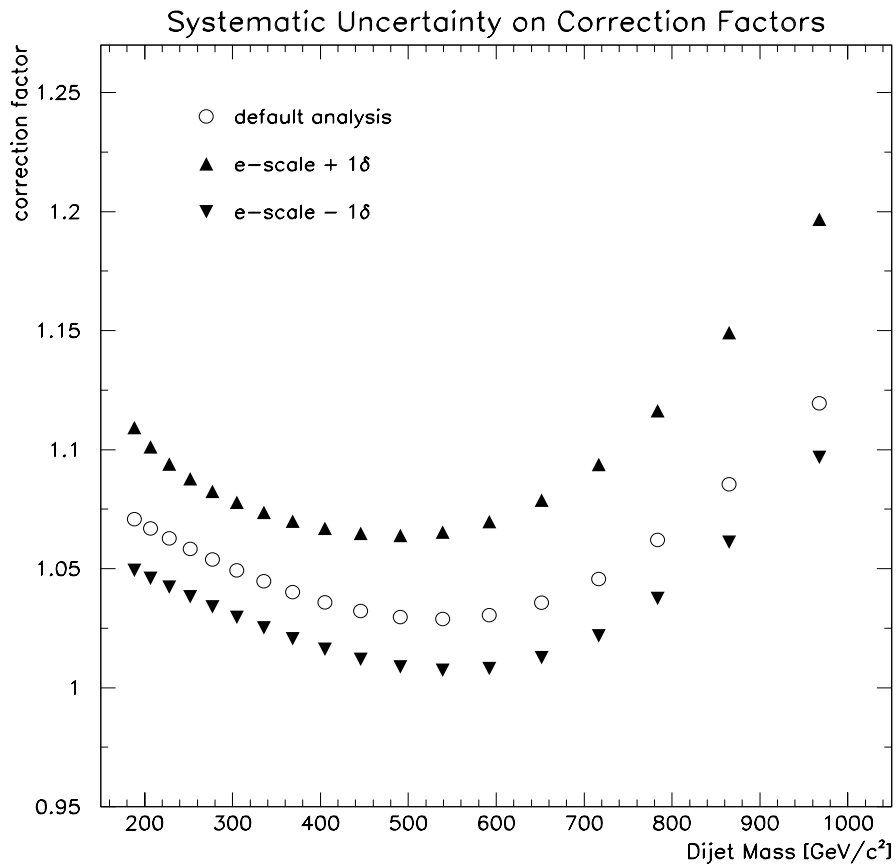


Figure 5.5: Unsmearing corrections as a function of the dijet mass: Default analysis (open circles), QFL scale corrections  $+1\sigma$  and  $-1\sigma$  (triangles).

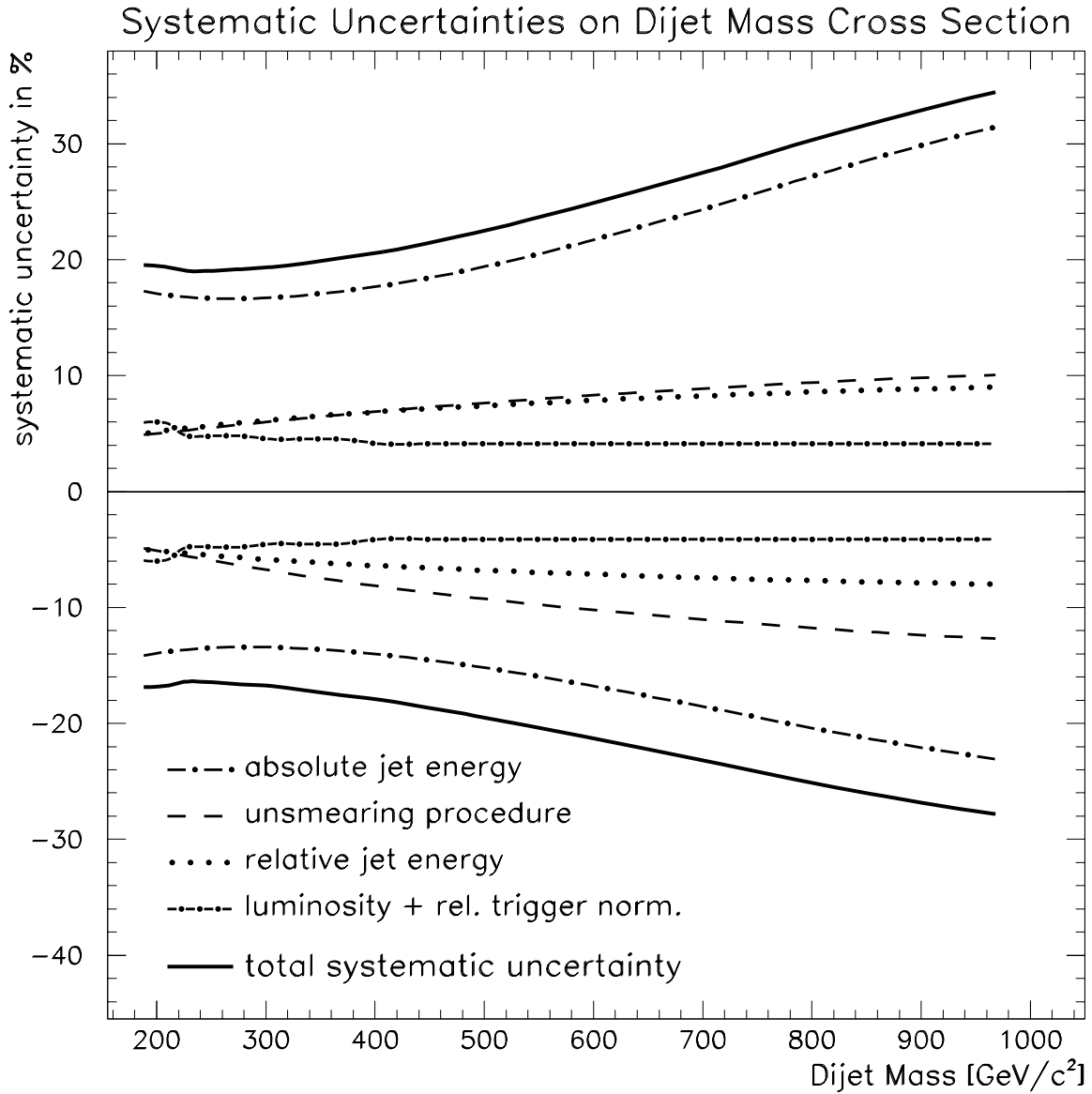


Figure 5.6: The systematic uncertainties on the dijet mass cross section as a function of the dijet mass. We show the total systematic uncertainty (thick solid), the absolute jet energy scale (widely dash-dotted), the relative jet energy scale (dotted), the combined uncertainties on the unsmearing procedure (dashed) and the combined uncertainties on the total luminosity and the relative jet trigger normalizations (narrowly dash-dotted).

# Chapter 6

## Results

In this Chapter we compare the fully corrected dijet mass cross section with predictions of next-to-leading order (NLO) QCD calculations. We quantify the differences between our data and the calculations for different choices of parton distribution functions and different values of the renormalization scale. We also compare our measurement with results from the DØ collaboration.

### 6.1 The Fully Corrected Cross Section

The values of the fully corrected dijet mass cross section, together with the statistical and systematic uncertainties, are listed in Table 6.1. The differential cross section in each dijet mass bin is given by

$$d\sigma/dM_{jj} = N/(K \Delta M_{jj} \mathcal{L} \epsilon), \quad (6.1)$$

where  $N$  is the number of events in the bin,  $K$  is the unsmearing correction factor,  $\Delta M_{jj}$  is the width of the mass bin,  $\mathcal{L}$  is the integrated luminosity and  $\epsilon$  is the efficiency of the trigger and  $z$ -vertex selections.

Across the range of measured dijet masses, the cross section falls by almost six orders

$M_{jj}$ bin (GeV/c <sup>2</sup> )	Trigger	average $M_{jj}$ (GeV/c <sup>2</sup> )	number of events	$d\sigma/dM_{jj}$ (pb/GeV/c <sup>2</sup> )	statistical uncertainty	systematic uncertainty
180 - 198	Jet 20	188	979	$6.07 \cdot 10^2$	3.2%	$+^{20}_{-17}\%$
198 - 217		207	581	$3.42 \cdot 10^2$	4.1%	$+^{19}_{-17}\%$
217 - 241	Jet 50	228	9343	$1.81 \cdot 10^2$	1.0%	$+^{19}_{-16}\%$
241 - 265		252	5131	$9.81 \cdot 10^1$	1.4%	$+^{19}_{-16}\%$
265 - 292		277	2943	$4.98 \cdot 10^1$	1.8%	$+^{19}_{-17}\%$
292 - 321	Jet 70	305	8366	$2.78 \cdot 10^1$	1.1%	$+^{19}_{-17}\%$
321 - 353		335	4785	$1.43 \cdot 10^1$	1.4%	$+^{20}_{-17}\%$
353 - 388		368	2714	$7.41 \cdot 10^0$	1.9%	$+^{20}_{-18}\%$
388 - 427	Jet 100	405	12342	$3.83 \cdot 10^0$	0.9%	$+^{21}_{-18}\%$
427 - 470		446	6781	$1.89 \cdot 10^0$	1.2%	$+^{21}_{-19}\%$
470 - 517		491	3551	$9.07 \cdot 10^{-1}$	1.7%	$+^{22}_{-19}\%$
517 - 568		539	1910	$4.50 \cdot 10^{-1}$	2.3%	$+^{23}_{-20}\%$
568 - 625		592	904	$1.90 \cdot 10^{-1}$	3.3%	$+^{25}_{-21}\%$
625 - 688		652	392	$7.42 \cdot 10^{-2}$	5.1%	$+^{26}_{-22}\%$
688 - 756		716	168	$2.92 \cdot 10^{-2}$	7.7%	$+^{28}_{-23}\%$
756 - 832		784	77	$1.18 \cdot 10^{-2}$	11%	$+^{30}_{-25}\%$
832 - 915		865	26	$3.57 \cdot 10^{-3}$	20%	$+^{32}_{-26}\%$
915 - 1025		968	9	$9.03 \cdot 10^{-4}$	33%	$+^{34}_{-28}\%$

Table 6.1: The fully corrected dijet mass cross section and the statistical and systematic uncertainties.

of magnitude. The experimental uncertainties on the cross section are dominated by the systematic uncertainties, except at the highest dijet masses.

## 6.2 QCD Calculations

For this analysis we selected high transverse momentum events where soft radiation has been removed by a cut on the minimum transverse energy of the jets. At the

same time, all individual hadrons within a jet cone were replaced by a single jet axis. Because the hadronic behaviour was averaged out, we can relate the hadronic jet axis and energy observed in the experiment to a jet constructed from a parton shower, calculated with perturbative QCD predictions.

We obtained theoretical predictions from JETRAD, version 2.0 [84], a parton level Monte Carlo program for inclusive one and two-jet production at hadron colliders. The calculations have been performed to next-to-leading order (NLO) in QCD. At leading order, the jet is modeled by a single parton and this lone parton's direction and energy are taken as the jet's axis and energy. The addition of NLO effects provides important improvements over leading order calculations. Firstly, the dependences on the unphysical renormalization and factorization scales are reduced, because the truncation of the perturbative series is postponed to one higher order. As a result, the normalization is more certain. Secondly, the sensitivity to the jet algorithm is reduced, because three partons are now admitted in the final state. A jet may now be formed by the merging of two partons. And thirdly, by admitting radiation into the final state, kinematic constraints due to the  $2 \rightarrow 2$  nature of the leading order prediction are relaxed.

The JETRAD program computes the lowest order matrix elements for the lowest order  $2 \rightarrow 2$  scattering processes and then uses Monte Carlo techniques to integrate over the phase space for the final state partons to obtain the two-jet cross section. A jet finding algorithm is then applied to the final state partons. Two partons are merged if they are within a spatial distance  $R_{sep} = 1.3R$ . The value of  $R_{sep}$  has been determined to ensure best correspondence between experimental jets and those from the calculations. Contributions from the underlying event are not included in the calculations. Details on the theoretical calculations of the two-jet cross section can be found in [84, 85].

### 6.3 Comparison of Data and QCD

In the following, we compare our fully corrected data with predictions from the JETRAD program. There are several uncertainties associated with NLO QCD calculations, the most important ones being the input parton distribution function (PDF) and the choice of the renormalization scale,  $\mu$ .

The parton distributions,  $f_i$ , are determined from a global fit to a wide range of deep inelastic scattering data. The basic procedure is to parameterize the  $f_i(x, Q^2)$  at a low value of  $Q^2 = Q_0^2$ , so that the  $f_i(x, Q^2)$  can be calculated at higher  $Q^2$  by using the next-to-leading-order DGLAP evolution equations. The data points are fitted for all  $Q_2^2 > Q_1^2$ , where  $Q_1^2 > Q_0^2$  is a value of  $Q^2$  where perturbative QCD is believed to be the dominant contribution. The results of the fitting procedure (and, therefore, of the parameterization) are sensitive mainly to the minimum  $Q^2$  value of the data that are included in the fit, the uncertainty on the determination of the gluon density at high  $x$  and the value of  $\alpha_s(M_Z^2)$ .

The two sets of parameterizations most commonly used are those of the CTEQ Collaboration and the group of A.D. Martin, R.G. Roberts and W.J. Stirling (MRS). We chose the CTEQ4M [86] parameterization as our default theory. Other parameterizations we used included CTEQ4HJ [86], MRST, MRST( $g \uparrow$ ) and MRST( $g \downarrow$ ) [87]. The difference between CTEQ4M and CTEQ4HJ is that the gluon density of the latter is higher at high  $x$ . It was adjusted to fit the data from the CDF inclusive jet- $E_T$  analysis [12], for which, at high jet- $E_T$ , the CTEQ4M prediction underestimated the data. Similarly, MRST( $g \uparrow$ ) and MRST( $g \downarrow$ ) are variations of the default MRST parameterization with higher and lower gluon densities, respectively. The MRST family are the most recent PDF's available. We also tested older versions of the above parameterizations, CTEQ3M [88], MRS(R2) [89] and MRS(D0') [90].

As our default normalization scale we chose  $\mu = 0.5E_T^{max}$ , where  $E_T^{max}$  is the energy of the highest-energy jet in the event. The value of the renormalization scale should

reflect the  $Q^2$  scale of the events. For inclusive measurements with two more jets  $\mu = 0.5E_T^{max}$  is the value most commonly used [91].

Figure 6.1 shows a comparison of the fully corrected data with our default theory, CTEQ4M with  $\mu = 0.5E_T^{max}$ , on a logarithmic scale. The error bars in this figure represent the statistical and systematic uncertainties, added in quadrature. The overall agreement between data and QCD predictions over almost six orders of magnitude is excellent.

Figure 6.2 shows the same comparison on a linear scale. We plot the fractional differences,  $(\text{data} - \text{theory}) / \text{theory}$ , between the data and the CTEQ4M prediction as a function of dijet mass. To compare other theories with CTEQ4M, the values of  $(\text{QCD} - \text{CTEQ4M}) / \text{CTEQ4M}$ , where QCD stands for CTEQ4HJ, MRST, MRST( $g \uparrow$ ) and MRST( $g \downarrow$ ), respectively, are also shown. The error bars indicate the statistical uncertainties and the shaded area represents the combined systematic uncertainty on the data. Note that the systematic uncertainties in Fig. 6.2 are correlated as a function of dijet mass (see below).

We see a trend towards an excess in the data over QCD calculations at high dijet masses. The CTEQ4 parameterizations generally reproduce the data within one standard deviation of the systematic uncertainties. As expected, at high dijet masses, CTEQ4HJ reproduces the data better than CTEQ4M. We observe a normalization difference between data and QCD of between 5 and 10% for the CTEQ4 family. The MRST parameterizations exhibit a larger normalization difference of about 20%. While MRST( $g \downarrow$ ) has the worst overall normalization, its shape describes the data better than MRST and MRST( $g \uparrow$ ).

As a check of the dependence of the calculations on the choice of  $\mu$ , we varied the value of  $\mu$  between  $0.5E_T^{max}$  and  $2.0E_T^{max}$  for the CTEQ4M parameterization, see Fig. 6.3. While the differences between the choices  $0.5E_T^{max}$  and  $E_T^{max}$  are small, compared to differences between different parameterizations, changing the value from  $0.5E_T^{max}$  to  $0.25E_T^{max}$  results in a change of the normalization of about 25%.

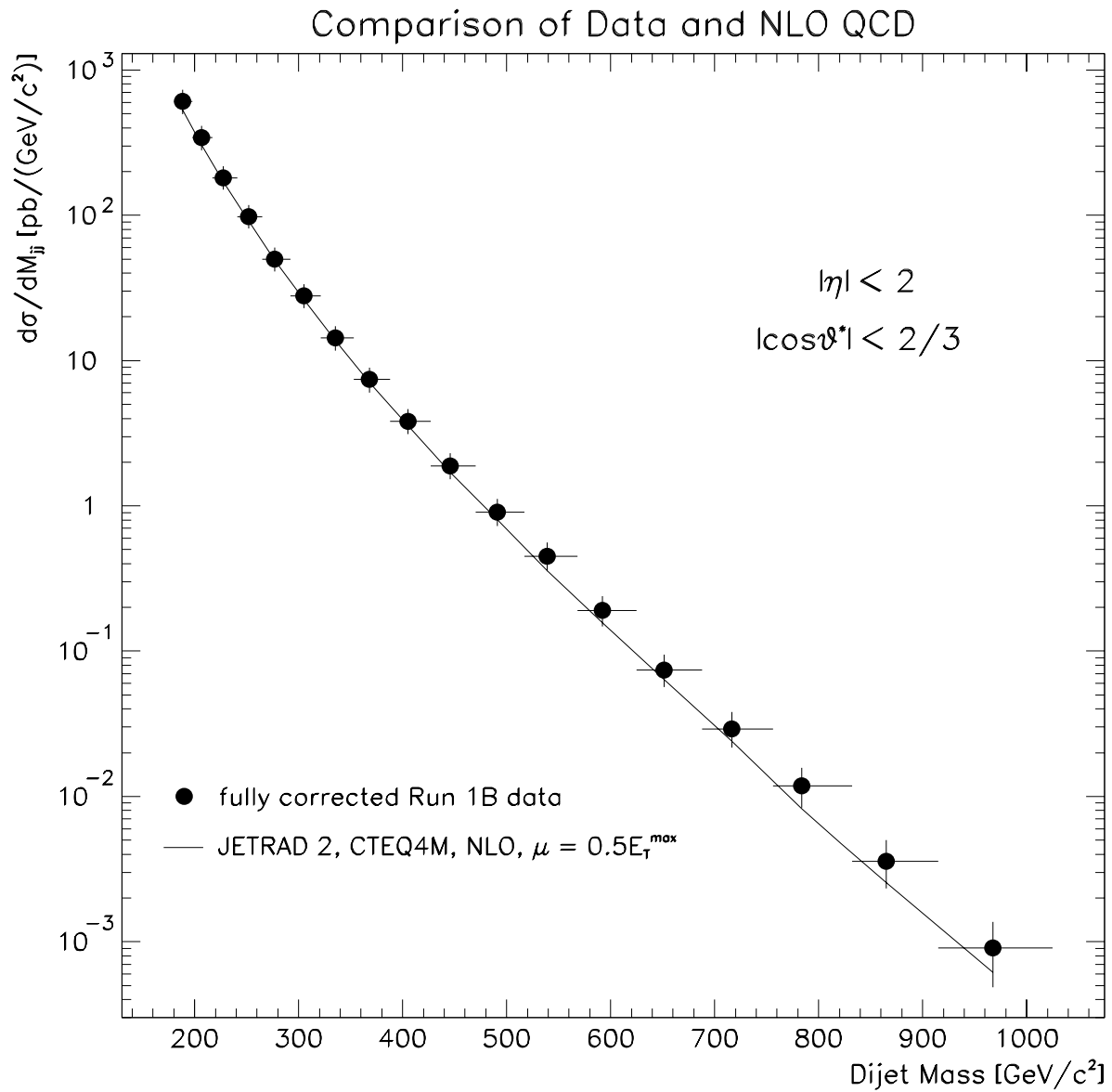


Figure 6.1: A comparison of the fully corrected data (full circles) with predictions from the JETRAD Monte Carlo program, using CTEQ4M and  $\mu = 0.5E_T^{\text{max}}$  (solid line). The bars represent the statistical and systematic uncertainties, added in quadrature.

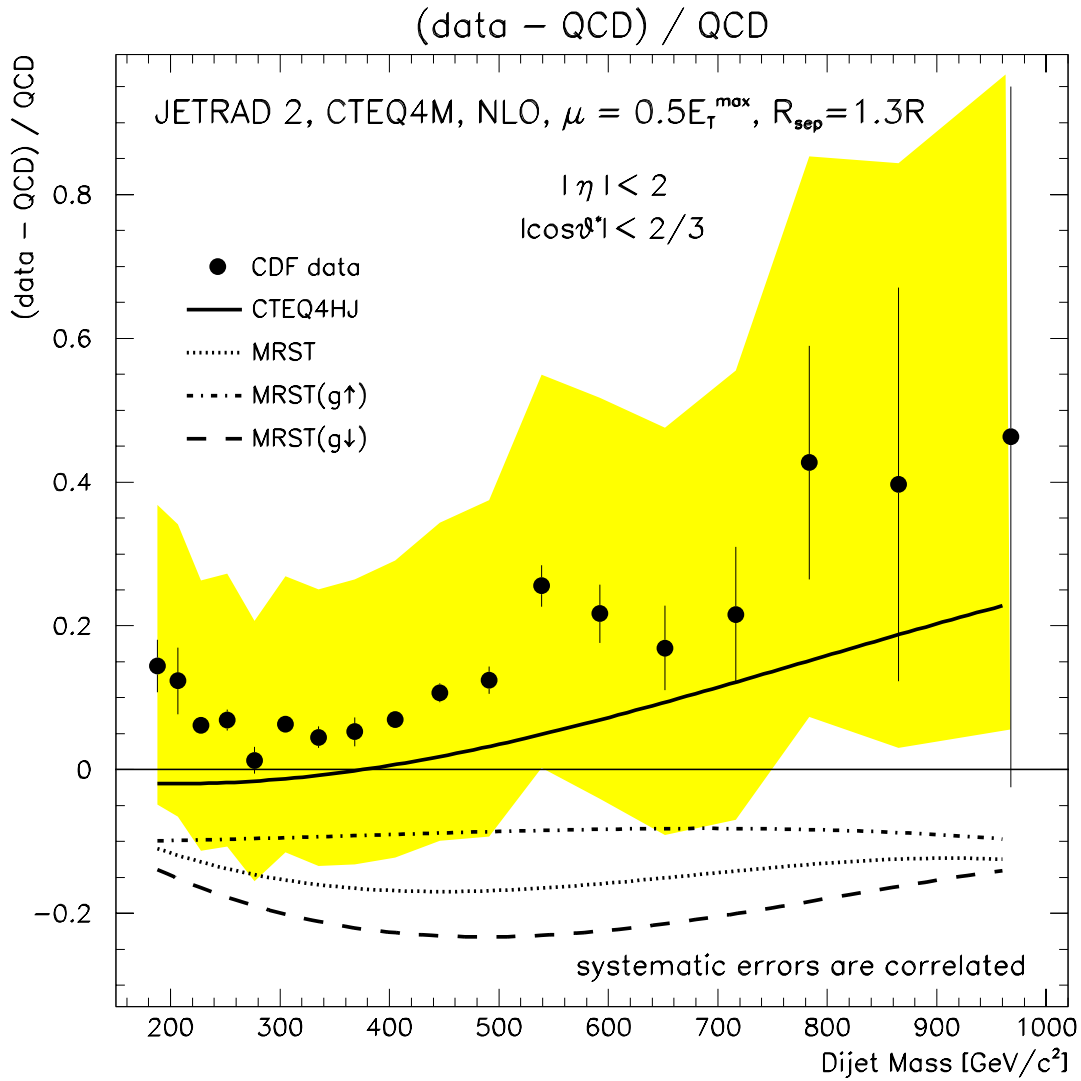


Figure 6.2: A comparison of our data with predictions from the JETRAD program for CTEQ4M (full circles) and comparisons of other parameterizations with CTEQ4M: CTEQ4HJ (solid), MRST (dotted), MRST( $g \uparrow$ ) (dash-dotted) and MRST( $g \downarrow$ ) (dashed). All QCD calculations were performed with  $\mu = 0.5E_T^{\max}$ . The error bars indicate the statistical uncertainties and the shaded area represents the combined systematic uncertainty.

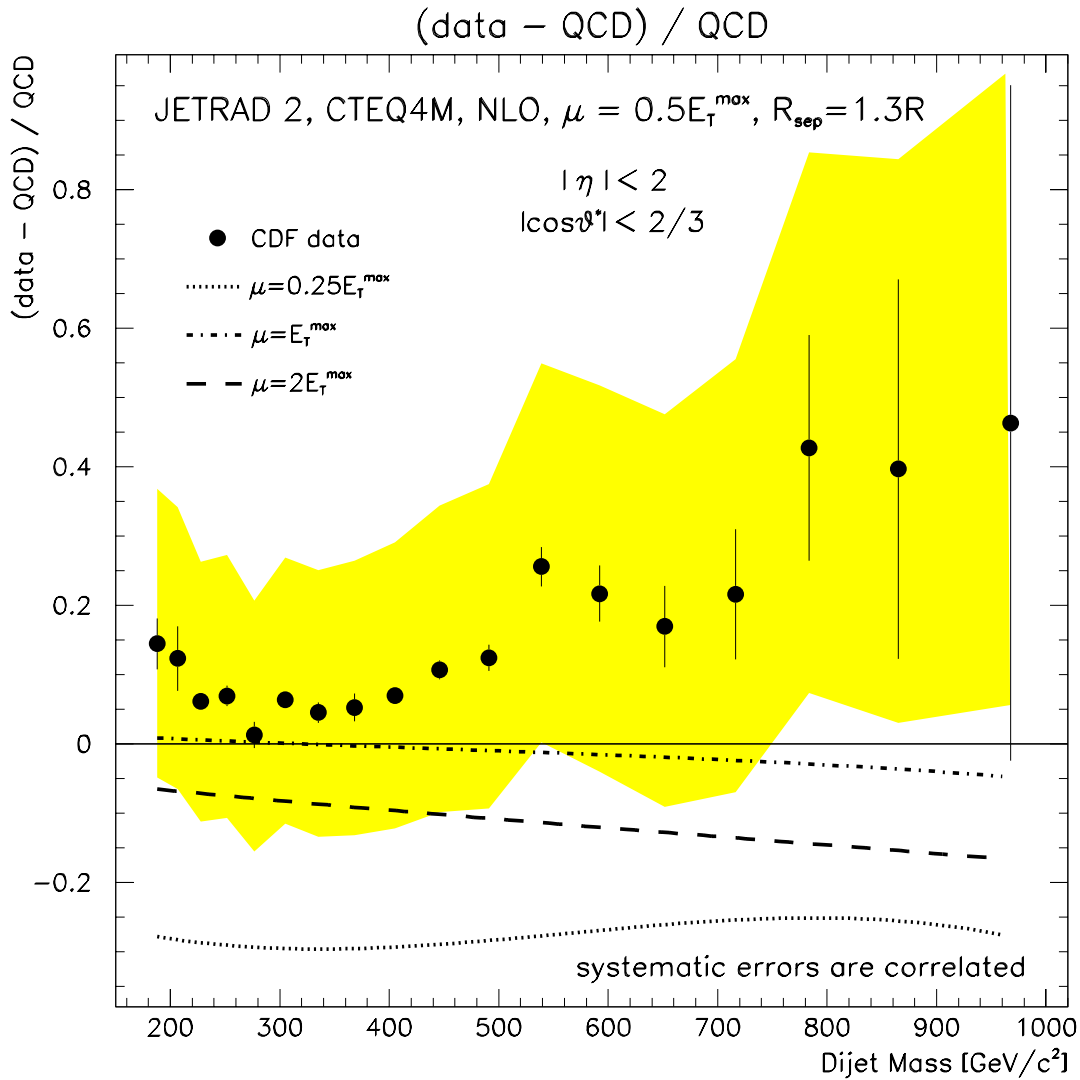


Figure 6.3: A comparison of our data with predictions from the JETRAD program for CTEQ4M,  $\mu = 0.5E_T^{\max}$  (full circles) and other choices of  $\mu$ :  $\mu = 0.25E_T^{\max}$  (dashed),  $\mu = E_T^{\max}$  (dotted) and  $\mu = 2E_T^{\max}$  (dash-dotted). The error bars indicate the statistical uncertainties and the shaded area represents the combined systematic uncertainty.

QCD calculations with other parton distribution functions and other choices of  $\mu$  are not plotted, but are quantitatively compared to the data in Section 6.4.

## 6.4 $\chi^2$ Evaluation between Data and Theories

To quantify the differences between the data and the theoretical predictions, we have chosen a  $\chi^2$  method [92]. To take the correlations of the individual systematic uncertainties into account, we made the following assumptions:

1. Each of the components of the total systematic uncertainty are 100% correlated as a function of dijet mass. For instance, if the luminosity is mismeasured by one standard deviation of the systematic uncertainty, it is mismeasured by the same amount in all bins.
2. The individual components of the systematic uncertainty, e.g. the integrated luminosity and the calibration of the absolute energy scale, are uncorrelated and can fluctuate independently.

To first order, the  $\chi^2$  is defined by the matrix equation

$$\chi^2 = \Delta^T V^{-1} \Delta, \quad \Delta = \begin{pmatrix} \Delta_1 \\ \Delta_2 \\ \cdot \\ \cdot \\ \Delta_n \end{pmatrix}, \quad (6.2)$$

where  $\Delta$  is the column vector of the differences between the data and the theory in the 18 dijet mass bins. It has the entries

$$\Delta_i = \frac{d\sigma_i^{data}}{dM_{jj}} - \frac{d\sigma_i^{theory}}{dM_{jj}}, \quad i = 1, 18. \quad (6.3)$$

The matrix  $V^{-1}$  is the inverse of the variance matrix

$$V = \begin{pmatrix} \sigma_{11}^2 & \sigma_{12}^2 & \cdot & \cdot & \sigma_{1n}^2 \\ \cdot & \sigma_{22}^2 & \cdot & \cdot & \cdot \\ \cdot & \cdot & \cdot & \cdot & \cdot \\ \sigma_{n1}^2 & \sigma_{n2}^2 & \cdot & \cdot & \sigma_{nn}^2 \end{pmatrix} \quad (6.4)$$

and the  $\sigma_{ij}^2$  are given by

$$\sigma_{ij}^2 = \sum_{k=1}^{12} \rho_{ij}^k \sigma_i(\text{sys}^k) \sigma_j(\text{sys}^k) + \delta_{ij} \sigma_i(\text{stat})^2, \quad (6.5)$$

where  $\sigma_i(\text{stat})$  is the statistical uncertainty and  $\sigma_i(\text{sys}^k)$  is the contribution to the systematic uncertainty from the individual component,  $k$ , in the  $i^{\text{th}}$  mass bin. Taking the sum over all twelve individual uncertainties, rather than the total systematic uncertainty, accounts for the fact that the individual components are uncorrelated. All correlation coefficients,  $\rho_{ij}^k$ , are defined to be one, since all components of the systematic uncertainty are taken to be 100% correlated. A variation of this assumption is discussed in Appendix A.

The systematic uncertainties on the dijet mass cross section are slightly asymmetrical. Since all data points are above the theoretical predictions, we used the low-side systematic uncertainties in our  $\chi^2$  evaluation. The individual values for the 18 dijet mass bins are listed in Table 6.2.

Table 6.3 summarizes the results of the  $\chi^2$  evaluation. We list the  $\chi^2$  values (for 18 degrees of freedom) and the corresponding probabilities for all theories we tested.

That the MRST( $g \downarrow$ ) produces a better  $\chi^2$  than MRST( $g \uparrow$ ) is due to the correlation of the systematic uncertainties. Because the individual components of the systematic uncertainties are completely correlated, the  $\chi^2$  contribution arising from a normalization difference is much smaller than the contributions from a shape difference between two curves. Similarly, in the case of CTEQ4M, the lowest  $\chi^2$  is realized with the choice

$M_{jj}$ (GeV/c <sup>2</sup> )	Individual Systematic Uncertainties on the Cross Section (%)												
	cal	frag	uevt	stab	rel	QFL	lum	uns	tails	J20	J50	J70	tot
188	7.8	7.1	7.2	6.2	5.0	2.0	4.1	4.0	2.0	3.5	1.7	1.9	16.9
207	7.8	7.1	6.6	6.2	5.2	2.4	4.1	4.0	2.4	3.5	1.7	1.9	16.8
228	7.8	7.1	6.0	6.2	5.4	2.7	4.1	4.0	2.8	–	1.7	1.9	16.4
252	7.9	7.1	5.5	6.3	5.5	3.1	4.1	4.0	3.2	–	1.7	1.9	16.5
277	7.9	7.1	5.1	6.4	5.7	3.4	4.1	4.0	3.7	–	1.7	1.9	16.6
305	8.1	7.2	4.7	6.5	5.9	3.8	4.1	4.0	4.1	–	–	1.9	16.8
335	8.2	7.3	4.4	6.6	6.1	4.1	4.1	4.0	4.5	–	–	1.9	17.1
368	8.4	7.5	4.1	6.8	6.2	4.5	4.1	4.0	4.9	–	–	1.9	17.6
405	8.7	7.7	3.9	7.0	6.4	4.8	4.1	4.0	5.3	–	–	–	18.0
446	9.0	8.0	3.7	7.3	6.6	5.2	4.1	4.0	5.7	–	–	–	18.6
491	9.4	8.3	3.5	7.6	6.8	5.5	4.1	4.0	6.1	–	–	–	19.3
539	9.9	8.7	3.4	8.0	7.0	5.9	4.1	4.0	6.5	–	–	–	20.2
592	10.5	9.2	3.2	8.5	7.1	6.2	4.1	4.0	6.9	–	–	–	21.2
652	11.2	9.8	3.2	9.1	7.3	6.6	4.1	4.0	7.4	–	–	–	22.3
716	11.9	10.5	3.1	9.7	7.5	6.9	4.1	4.0	7.8	–	–	–	23.5
784	12.8	11.2	3.0	10.3	7.7	7.3	4.1	4.0	8.2	–	–	–	24.8
865	13.7	12.0	3.0	11.1	7.8	7.7	4.1	4.0	8.6	–	–	–	26.3
968	14.7	12.8	2.9	12.0	8.0	8.0	4.1	4.0	9.0	–	–	–	27.8

Table 6.2: The individual low-side systematic uncertainties (in %) for the 18 dijet mass bins. The shorthand notations in the header stand for the following: *cal*: calibration of the central calorimeter, *frag*: jet fragmentation, *uevt*: underlying event, *stab*: stability of the central calorimeter, *rel*: relative energy scale, *QFL*: QFL energy scale shift, *lum*: integrated luminosity, *uns*: unsmearing procedure, *tails*: parameterization of the tails of the detector response, *J20*, *J50* and *J70*: relative normalizations of the Jet 20, 50 and 70 triggers, *tot*: total systematic uncertainty.

PDF	$D$ (where $\mu = DE_T^{max}$ )	$\chi^2$ (18 DOF)	probability
CTEQ4M	0.5	41	$0.16 \cdot 10^{-2}$
CTEQ4HJ	0.5	26	$0.99 \cdot 10^{-1}$
MRST	0.5	22	0.24
MRST( $g \uparrow$ )	0.5	25	0.13
MRST( $g \downarrow$ )	0.5	17	0.56
CTEQ4M	0.25	28	$0.67 \cdot 10^{-1}$
CTEQ4M	1.0	40	$0.22 \cdot 10^{-2}$
CTEQ4M	2.0	33	$0.16 \cdot 10^{-1}$
CTEQ4HJ	1.0	22	0.22
CTEQ3M	0.5	39	$0.30 \cdot 10^{-2}$
CTEQ3M	1.0	45	$0.38 \cdot 10^{-3}$
MRST	1.0	18	0.48
MRS(R2)	0.5	40	$0.21 \cdot 10^{-2}$
MRS(D0')	1.0	37	$0.58 \cdot 10^{-2}$

Table 6.3: The  $\chi^2$  values between the data and the theories and the corresponding probabilities. The first theory, CTEQ4M with  $\mu = 0.5E_T^{max}$ , is our default theory. The second and third groups of theories are graphically compared to the default theory in Figs.6.2 and 6.3, respectively. The predictions of the last group are not shown graphically.

of  $\mu = 0.25E_T^{max}$ , because for this choice of  $\mu$  the shape describes the data better than for any other value of  $\mu$ . More details of the  $\chi^2$  procedure are given in Appendix A.

In conclusion, for the assumption of completely correlated systematic uncertainties, the MRST family and the CTEQ4HJ parameterization describe our data best. The lowest value of  $\chi^2$  is realized with MRST( $g \downarrow$ ) and  $\mu = 0.5E_T^{max}$ . All older versions of the above parameterizations, CTEQ3M, MRS(R2) and MRS(D0'), return higher  $\chi^2$  values than their modern counterparts. The above ranking holds for plausible values of the correlation coefficients (see Appendix A). However, since the absolute values of

$\chi^2$  depend on the assumption of completely correlated systematic uncertainties, we refrain from excluding any of the theories we tested.

## 6.5 Comparison of CDF and DØ Data

A comparison of our results with those of the DØ experiment [93] is shown in Fig. 6.4. Here, data from both experiments are compared to calculations from JETRAD, using the CTEQ4M parton distribution function and a normalization scale of  $\mu = 0.5E_T^{max}$ . However, the kinematical ranges for the two measurements are different. The CDF measurement was performed in the region  $|\eta| < 2$  and  $|\cos\theta^*| < 2/3$ , whereas the DØ measurement was made in the region  $|\eta| < 1$ , with no requirement on  $\cos\theta^*$ . The DØ collaboration also used a slightly different definition of the dijet mass. Assuming that the jets are massless, the dijet mass can be measured as

$$M_{jj} = \sqrt{2E_T^{jet1} E_T^{jet2} [\cosh(\Delta\eta) - \cos(\Delta\phi)]}, \quad (6.6)$$

where  $\Delta\eta$  and  $\Delta\phi$  are the differences in  $\eta$  and  $\phi$  between the two jets, respectively.

Given the statistical and systematic uncertainties, the data from the two experiments are in very good agreement. Both measurements are dominated by systematic uncertainties. Both experiments find that the QCD predictions are generally lower than the data at high dijet masses but QCD reproduces the data for both within the experimental uncertainties.

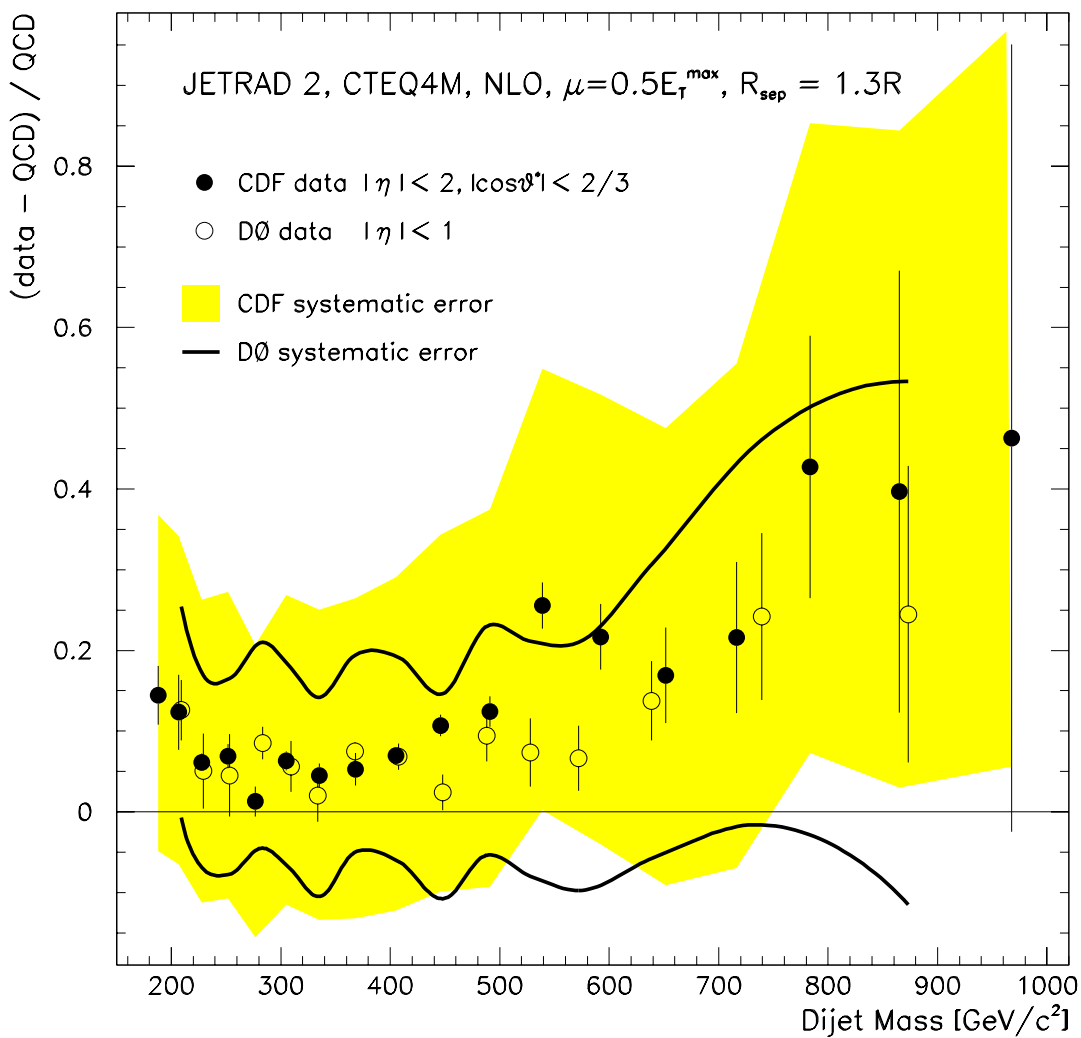


Figure 6.4: A comparison of our data (solid circles) with results from the DØ collaboration (open circles). The systematic uncertainties are indicated by the shared area (CDF) and the solid lines (DØ), respectively. Note that the kinematical ranges are different for the two experiments.

# Conclusions

We have used the CDF Run 1B data sample of  $86\text{pb}^{-1}$  to measure the fully corrected dijet mass cross section in the kinematical region  $|\eta| < 2$  and  $|\cos\theta^*| < 2/3$ . The data have been corrected for calorimeter response and for detector resolution effects, using an analytic unsmearing procedure. The internal consistency of this procedure has been demonstrated.

We have compared the fully corrected data with predictions from next-to-leading order QCD calculations, obtained with the JETRAD Monte Carlo program. We see the same trend towards an excess in the data at high dijet masses as in the jet- $E_T$  distribution at high  $E_T$ . A  $\chi^2$  evaluation of the differences between the data and the calculations for different parton distribution functions and for different choices of the renormalization scale has been performed. Assuming 100%-correlated systematic uncertainties, the MRST family and the CTEQ4HJ parameterization describe our data best. The above ranking holds for plausible values of the correlation coefficients. However, since the absolute values of  $\chi^2$  depend on the assumption of completely correlated systematic uncertainties, we do not exclude any of the theories we tested. Finally, we have compared our data with results from the DØ collaboration and find the data from the two experiments to be in good agreement.

Until the Large Hadron Collider (LHC) commences operation in the year 2005, the Tevatron will remain the world's highest-energy accelerator. Currently, preparations for the next Tevatron run (Run 2) are in full swing. Run 2, which is scheduled to begin in April 2000, is expected to collect  $2\text{fb}^{-1}$  of data at a slightly higher center-

of-mass energy of 2 TeV. The increase in statistics by a factor of 20, compared to the present analysis, will decrease the statistical uncertainty significantly.

To handle the higher rate of data taking during Run 2, the gas-based Run 1 Plug Calorimeter has been replaced by a scintillator/absorber sandwich calorimeter with an improved energy resolution. While the hardware upgrade of the CDF detector nears its completion, a significant effort is being made to improve the understanding of the absolute energy scale of the central calorimeter, the source of the largest experimental uncertainty in this analysis. Although this constitutes a challenging task, it is hoped that the Run 2 data sample will enable us to test Quantum Chromodynamics with higher accuracy and that our understanding of the strong interactions will continue to improve.

# Appendix A

## Details of the $\chi^2$ Procedure

In this Appendix we discuss the  $\chi^2$  procedure that was used to quantify the differences between our data and the QCD predictions in more detail. This discussion is motivated by fact that MRST( $g\downarrow$ ), the parameterization whose predictions are furthest away from the data points, produces the best  $\chi^2$  of all the theories we tested.

### A.1 Floating Normalization of the Theory

From Fig. 6.2 it can be seen that, whereas the normalization differences between the CTEQ4M parameterization and the data are only about 5%, the normalization for the MRST( $g\downarrow$ ) prediction underestimates the data by about 20%. Despite this larger normalization difference, MRST( $g\downarrow$ ) provides, according to the  $\chi^2$  method, a better description of our data than CTEQ4M.

We explain this with the correlations of the systematic uncertainties: For correlated uncertainties, normalization differences are less costly, in terms of the overall  $\chi^2$ , than shape differences. To investigate the relative importance of normalization and shape differences further, we calculated the  $\chi^2$  between the data and four of the theories of Fig. 6.2, for freely floating normalizations,  $n$ . In other words, we varied the  $\Delta_i$

according to

$$\Delta_i = \frac{d\sigma^{data}}{dM_{jj}^i} - n \frac{d\sigma^{theory}}{dM_{jj}^i}. \quad (\text{A.1})$$

The total  $\chi^2$  between the data and the theories, as a function of  $n$ , are shown in Fig. A.1. For reasons that will become clear below, we used the total systematic uncertainties, rather than the sum over all individual contributions. This change does not affect the qualitative behaviour of the  $\chi^2$ . Since (for some values of  $n$ ) the theory predictions are above the data, we used the arithmetic mean of the absolute values of the systematic uncertainties. We emphasize that this procedure was performed merely to understand the behaviour of the  $\chi^2$  and that it has no obvious physical interpretation, since there is no physical parameter in the theory that would change the normalization of the cross section uniformly for all dijet masses. Figure A.1 shows that all theories return their lowest  $\chi^2$  for normalizations of  $n < 1$ . Naively, one would expect the  $\chi^2$  to favour a normalization of  $n > 1$ , in order to minimize the differences between the theories and the data.

The following simple numerical example suggests why the  $\chi^2$  procedure might prefer a normalization of  $n < 1$ , even for theoretical predictions that are below the data in every bin. The toy model of Table A.1 has characteristics similar to those of our data sample: Large correlated systematic uncertainties that increase in size and negligible statistical uncertainties. This model is to be compared to predictions of a toy theory, listed in Table A.1 as well.

bin	data	$\sigma(sys)$	$\sigma(stat)$	theory
1	100	20	2	90
2	150	60	10	90

Table A.1: Values and uncertainties of a toy data set and values of a toy theory.

A graphical comparison of data and theory is shown in Fig. A.2. The error bars represent the 100%-correlated systematic uncertainties. Statistical uncertainties not

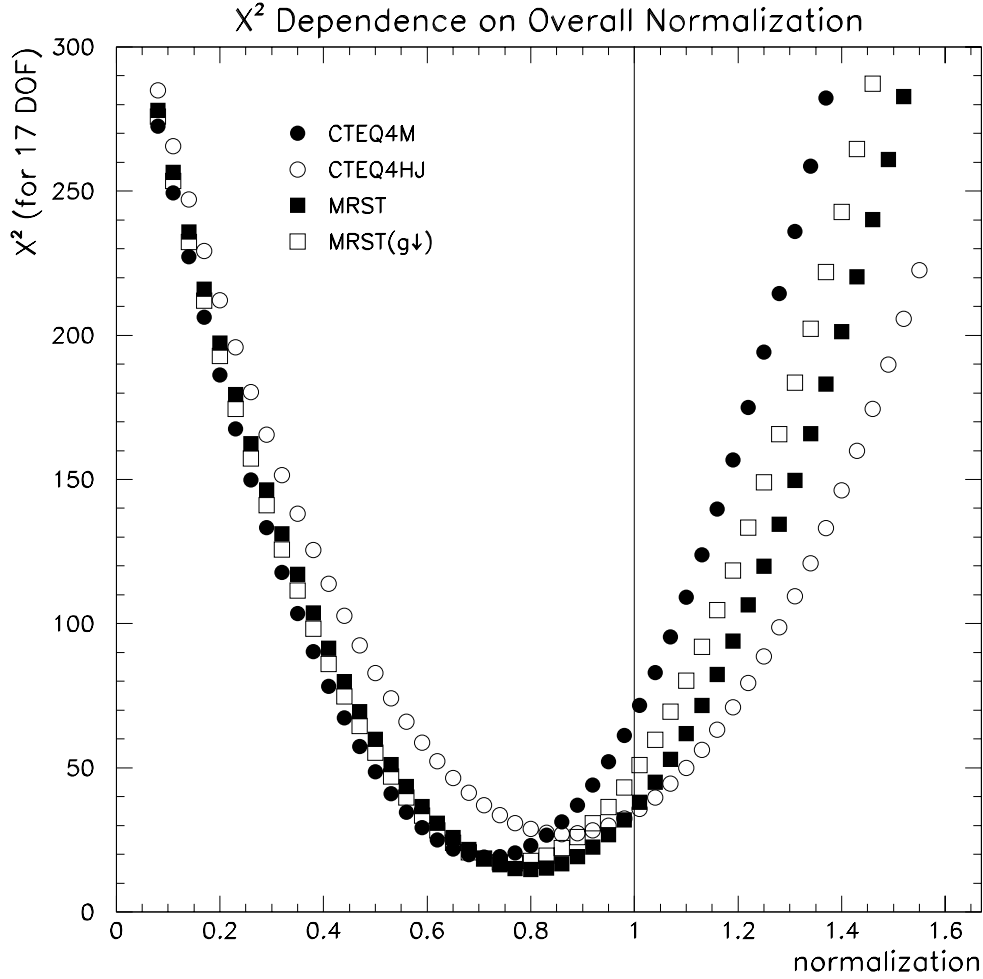


Figure A.1: The total  $\chi^2$  values between the data and the theoretical predictions for freely floating normalizations,  $n$ , of the theories. The default normalization ( $n = 1$ ) is indicated by the vertical line.

are shown. Note that, in both bins, the data points are higher than the theoretical predictions.

In this example, the total  $\chi^2$  between the data and the theory is 7.0. If the normalization of the theory is allowed to float freely, the lowest  $\chi^2$  value of 1.5 is realized for a normalization of  $n = 0.85$ , a value that moves the theory further away from the data. To understand why moving the theory away from the data leads to a lower  $\chi^2$ , it is instructive to look at the terms that contribute to the total  $\chi^2$ . For the simple

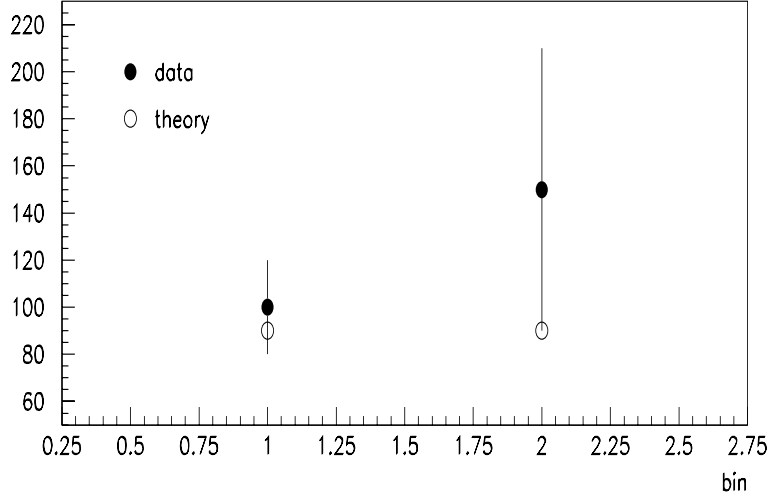


Figure A.2: Graphical comparison of a toy data set with a toy theory. The total  $\chi^2$  can be improved by lowering the normalization of the theory.

case of two data points, the  $\chi^2$  is given by

$$\chi^2 = \frac{\Delta_1^2 [\sigma_2(sys)^2 + \sigma_2(stat)^2] - 2\Delta_1\Delta_2\rho_{12}\sigma_1(sys)\sigma_2(sys) + \Delta_2^2 [\sigma_1(sys)^2 + \sigma_1(stat)^2]}{\sigma_1(sys)^2\sigma_2(stat)^2 + \sigma_2(sys)^2\sigma_1(stat)^2 + \sigma_1(stat)^2\sigma_2(stat)^2 + (1-\rho_{12}^2)\sigma(sys_1)^2\sigma(sys_2)^2}. \quad (\text{A.1})$$

A change of the normalization only affects the values of  $\Delta_1$  and  $\Delta_2$ , which only appear in the numerator. Assuming  $\rho_{12} = 1$  and dividing numerator and denominator of Eqn. (A.1) by  $\sigma_1(sys)^2\sigma_2(sys)^2$  the  $\chi^2$  can be approximated for very small statistical uncertainties by

$$\chi^2 \approx c \left( \frac{\Delta_1^2}{\sigma_1(sys)^2} - \frac{2\Delta_1\Delta_2}{\sigma_1(sys)\sigma_2(sys)} + \frac{\Delta_2^2}{\sigma_2(sys)^2} \right) = c \left( \frac{\Delta_1}{\sigma_1(sys)} - \frac{\Delta_2}{\sigma_2(sys)} \right)^2, \quad (\text{A.2})$$

where all  $\Delta$ -independent terms have been absorbed into the constant,  $c$ . From Eqn. (A.2) it can be seen that the value of  $\chi^2$  does not depend on the absolute values of  $\Delta_1$  and  $\Delta_2$ . Instead, the  $\chi^2$  is minimal for the case  $\frac{\Delta_1}{\sigma_1(sys)} = \frac{\Delta_2}{\sigma_2(sys)}$ . In other words, the  $\chi^2$  procedure prefers constant differences, in terms of the systematic uncertainty, between the data and the theory.

To verify the above hypothesis, we consider the differences between the toy data and the toy theory. Figure A.3 shows the values of  $(\text{data} - \text{theory}) / (\text{systematic})$

uncertainty) for two values of  $n$ :  $n = 1$  and  $n = 0.85$ , the value of  $n$  for which the  $\chi^2$  is at its absolute minimum.

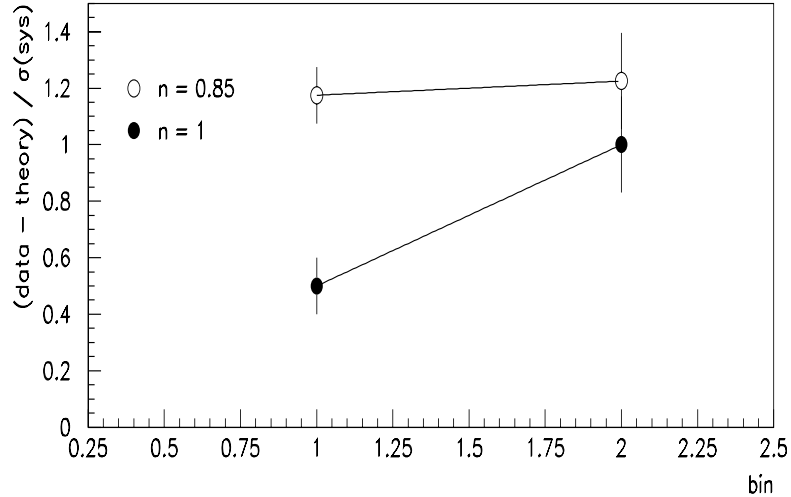


Figure A.3: The differences between the toy data set and a theory in terms of the systematic uncertainties. Although the theory is further away from the data points for a normalization of  $n = 0.85$ , the resulting  $\chi^2$  is lower than for  $n = 1$ . The error bars indicate the statistical uncertainties.

Although the theory is further away from the data in the case of  $n = 0.85$ , the  $\chi^2$  is lower than for  $n = 1$ . The reason for this counter-intuitive behaviour is that, at  $n = 0.85$ , the difference between the data and the theory is constant in terms of the systematic uncertainty. This corresponds to a normalization difference between the data and the theory, which results in a lower  $\chi^2$  than a difference in shapes. Because, as with our data, the relative size of the systematic uncertainties grows with the bin number, a constant offset between data and theory can be achieved by moving the theory to even lower values.

From Fig. A.3 it is also clear that contributions to the  $\chi^2$  from normalization and shape differences are inseparable. If the correlated systematic uncertainties increase (or decrease) with the bin number, changing the overall normalization of the theory inevitably means altering its shape, relative to the data.

Figure A.4 shows the corresponding information for our dijet mass data and the four theories. For each theory, we plot the values of  $(\text{data} - \text{theory}) / (\text{systematic uncer-}$

tainty) for two choices of the normalization:  $n = 1$  and  $n = n_{min}$ , where  $n_{min}$  is the value of  $n$  for which the  $\chi^2$  between the data and the theory is at its absolute minimum. As in Fig.A.1, the systematic uncertainty plotted in Fig.A.4 is the total systematic uncertainty (and not the sum over all individual components). Also displayed are linear fits to the data points and the statistical uncertainties.

We can see from Fig. A.4 that for each theory (with the possible exception of CTEQ4HJ) the linear fit to the data points has a slope that is smaller for  $n = n_{min}$  than for  $n = 1$ . For MRST( $g \downarrow$ ) and CTEQ4HJ the slope of the linear fit is smaller than for CTEQ4M and MRST. Accordingly, the latter two return a higher  $\chi^2$  value (see Fig.A.1). The low value of  $\chi^2$  for MRST( $g \downarrow$ ) can be explained by the fact that the data points are much less scattered around the straight line fit, particularly at low masses. This is confirmed by the plot of the fractional differences between the data and the theories (Fig.6.2). The parameterization that reproduces the shape of the data best at the low end of the dijet mass spectrum is MRST( $g \downarrow$ ). Although the situation is not as clear as in the case of the toy model, Fig. A.4 shows that the above argument can, at least in part, explain the  $\chi^2$  behavior.

## A.2 Variation of the Correlation Coefficients

We expect all systematic uncertainties to be 100% correlated. However, we cannot prove this assumption and there is an uncertainty associated with the values of the correlation coefficients. To check the dependence of the results of the  $\chi^2$  comparison on the correlation coefficients, we varied their values systematically from 0 to 1. Figure A.5 shows the  $\chi^2$  (for 18 DOF) for the four theories as a function of the correlation coefficients. Note that all values of  $\rho_{ij}^k$  in Fig. A.5 are identical and are changed simultaneously. In principle, each value of  $\rho_{ij}^k$  could be varied independently. The  $\chi^2$  exhibits a strong dependence of the correlation coefficients for values of  $\rho > 0.9$ , where the  $\chi^2$  rises drastically. This sharp increase can be explained with

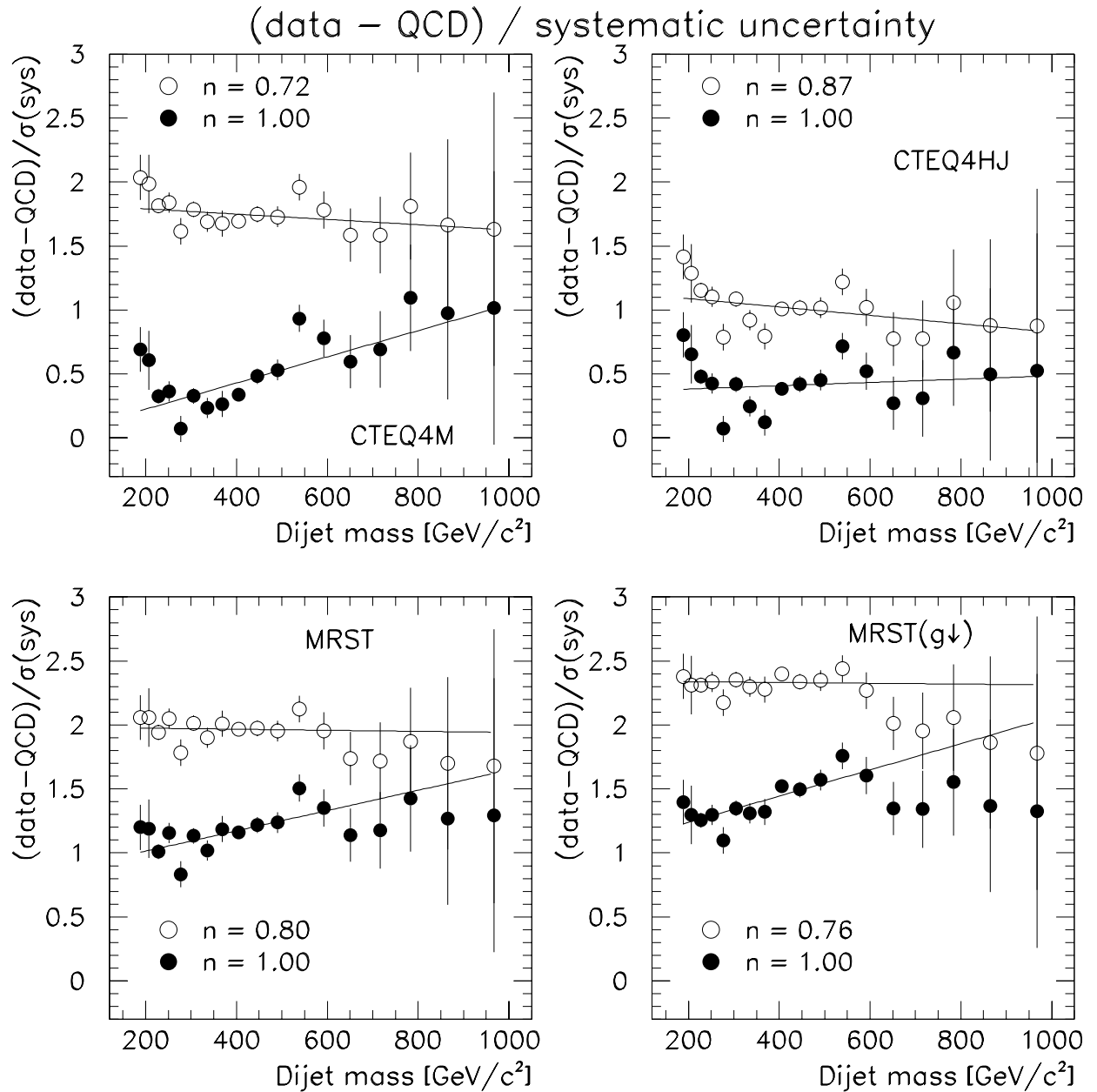


Figure A.4: The differences between the data and the four theories in terms of the absolute systematic uncertainties, as a function of dijet mass. For each theory, the values for two choices of  $n$  are plotted:  $n = 1$  and  $n = n_{min}$ , with  $n_{min}$ , the value of  $n$  for which the  $\chi^2$  between the data and the theory is in its absolute minimum. Also shown are linear fits to the data points. The errors bars represent the statistical uncertainty.

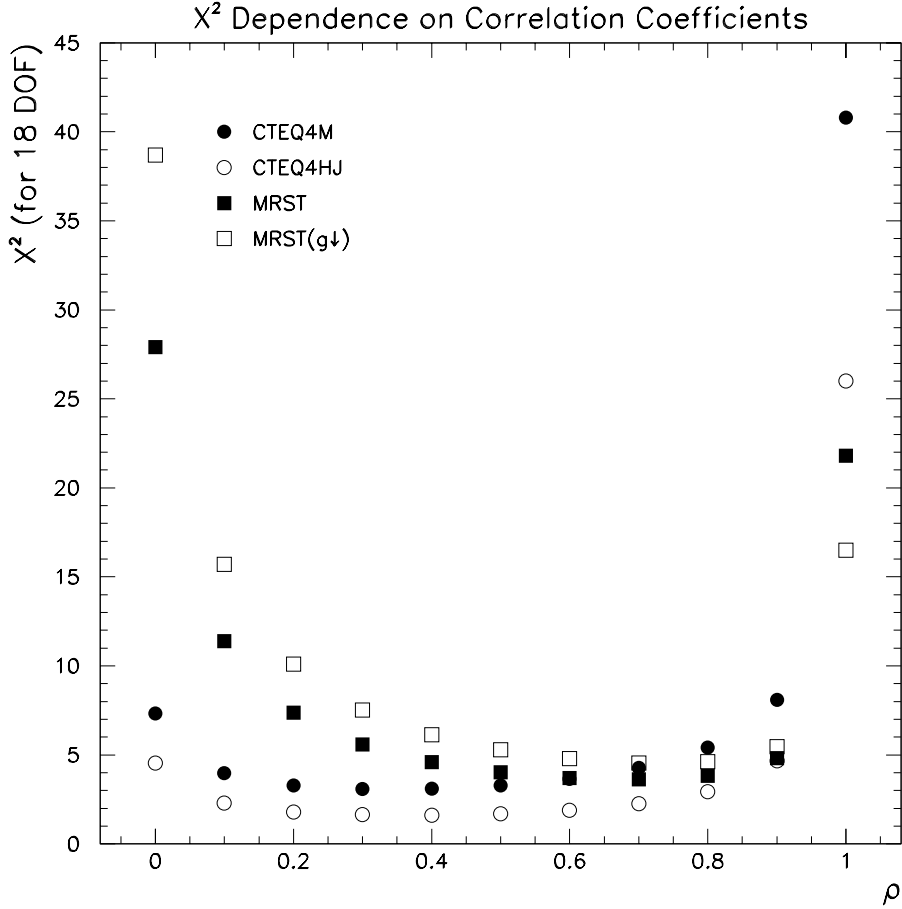


Figure A.5: The dependence of the total  $\chi^2$  on the correlation coefficient  $\rho$ .

the definition of the  $\chi^2$  (Eqn. (A.1)), which has a pole for 100%-correlated systematic uncertainties and zero statistical uncertainties. In our analysis, the statistical uncertainties are much smaller than the systematic uncertainties over most of the measured dijet mass range. Therefore, small deviations from values of  $\rho = 1$  can lead to large changes in the  $\chi^2$ .

From Fig. A.5 we can see that the data prefer the MRST and MRST( $g \downarrow$ ) parameterizations over CTEQ4HJ only for 100%-correlated uncertainties ( $\rho = 1$ ). For smaller values of the correlation coefficients, the normalization difference between the data and MRST( $g \downarrow$ ) results in higher  $\chi^2$  values. For the extreme case of uncorrelated

uncertainties ( $\rho = 0$ ), MRST( $g \downarrow$ ) is the theory that describes the data least, a result that one intuitively expects by looking at Fig. 6.2.

### A.3 Summary of the $\chi^2$ Procedure

When we established the systematic uncertainties on the dijet mass cross section, we varied each component individually. This is reflected by the sum over all individual components in the  $\chi^2$  calculation. The assumption that each component of the systematic uncertainty is 100% correlated is correct, provided that we have identified all of its individual components. We can see two ways of refining the  $\chi^2$  calculation.

1. More components of the systematic uncertainty could be identified. This would involve breaking up the known components even further. For instance, components of the uncertainty on the calibration of the calorimeter could be identified that affect different energy ranges differently (leakage, scintillator aging etc.).
2. Monte Carlo experiments could be performed to measure the correlation coefficients for each component of systematic uncertainty. However, considering the strong dependence of the  $\chi^2$  on the values of  $\rho_{ij}^k$ , it is doubtful that an enlightening accuracy could be achieved.

Looking at Fig. A.5, we see that for low values of  $\rho_{ij}^k$  the  $\chi^2$  becomes unphysically small for all theories. Nonetheless, for plausible values of  $\rho_{ij}^k$ , the ranking of the parameterizations of the PDF holds and we conclude that MRST( $g \downarrow$ ) and CTEQ4HJ describe our data best. Since the absolute values of  $\chi^2$  exhibit a dependence on the correlation coefficients, we refrain from excluding any of the theories we tested.

# Appendix B

## The CDF Collaboration

F. Abe,<sup>17</sup> H. Akimoto,<sup>39</sup> A. Akopian,<sup>31</sup> M. G. Albrow,<sup>7</sup> S. R. Amendolia,<sup>27</sup>  
D. Amidei,<sup>20</sup> J. Antos,<sup>33</sup> S. Aota,<sup>37</sup> G. Apollinari,<sup>31</sup> T. Arisawa,<sup>39</sup> T. Asakawa,<sup>37</sup>  
W. Ashmanskas,<sup>5</sup> M. Atac,<sup>7</sup> P. Azzi-Bacchetta,<sup>25</sup> N. Bacchetta,<sup>25</sup> S. Bagdasarov,<sup>31</sup>  
M. W. Bailey,<sup>22</sup> P. de Barbaro,<sup>30</sup> A. Barbaro-Galtieri,<sup>18</sup> V. E. Barnes,<sup>29</sup>  
B. A. Barnett,<sup>15</sup> M. Barone,<sup>9</sup> G. Bauer,<sup>19</sup> T. Baumann,<sup>11</sup> F. Bedeschi,<sup>27</sup>  
S. Behrends,<sup>3</sup> S. Belforte,<sup>27</sup> G. Bellettini,<sup>27</sup> J. Bellinger,<sup>40</sup> D. Benjamin,<sup>35</sup>  
J. Bensinger,<sup>3</sup> A. Beretvas,<sup>7</sup> J. P. Berge,<sup>7</sup> J. Berryhill,<sup>5</sup> S. Bertolucci,<sup>9</sup> S. Bettelli,<sup>27</sup>  
B. Bevensee,<sup>26</sup> A. Bhatti,<sup>31</sup> K. Biery,<sup>7</sup> C. Bigongiari,<sup>27</sup> M. Binkley,<sup>7</sup> D. Bisello,<sup>25</sup>  
R. E. Blair,<sup>1</sup> C. Blocker,<sup>3</sup> K. Bloom,<sup>20</sup> S. Blusk,<sup>30</sup> A. Bodek,<sup>30</sup> W. Bokhari,<sup>26</sup>  
G. Bolla,<sup>29</sup> Y. Bonushkin,<sup>4</sup> D. Bortoletto,<sup>29</sup> J. Boudreau,<sup>28</sup> A. Brandl,<sup>22</sup> L. Breccia,<sup>2</sup>  
C. Bromberg,<sup>21</sup> N. Bruner,<sup>22</sup> R. Brunetti,<sup>2</sup> E. Buckley-Geer,<sup>7</sup> H. S. Budd,<sup>30</sup>  
K. Burkett,<sup>11</sup> G. Busetto,<sup>25</sup> A. Byon-Wagner,<sup>7</sup> K. L. Byrum,<sup>1</sup> M. Campbell,<sup>20</sup>  
A. Caner,<sup>27</sup> W. Carithers,<sup>18</sup> D. Carlsmith,<sup>40</sup> J. Cassada,<sup>30</sup> A. Castro,<sup>25</sup> D. Cauz,<sup>36</sup>  
A. Cerri,<sup>27</sup> P. S. Chang,<sup>33</sup> P. T. Chang,<sup>33</sup> H. Y. Chao,<sup>33</sup> J. Chapman,<sup>20</sup> M. -T. Cheng,<sup>33</sup>  
M. Chertok,<sup>34</sup> G. Chiarelli,<sup>27</sup> C. N. Chiou,<sup>33</sup> F. Chlebana,<sup>7</sup> L. Christofek,<sup>13</sup> R. Cropp,<sup>14</sup>  
M. L. Chu,<sup>33</sup> S. Cihangir,<sup>7</sup> A. G. Clark,<sup>10</sup> M. Cobal,<sup>27</sup> E. Cocca,<sup>27</sup> M. Contreras,<sup>5</sup>  
J. Conway,<sup>32</sup> J. Cooper,<sup>7</sup> M. Cordelli,<sup>9</sup> D. Costanzo,<sup>27</sup> C. Couyoumtzelis,<sup>10</sup>

D. Cronin-Hennessy,<sup>6</sup> R. Culbertson,<sup>5</sup> D. Dagenhart,<sup>38</sup> T. Daniels,<sup>19</sup> F. DeJongh,<sup>7</sup> S. Dell'Agnello,<sup>9</sup> M. Dell'Orso,<sup>27</sup> R. Demina,<sup>7</sup> L. Demortier,<sup>31</sup> M. Deninno,<sup>2</sup> P. F. Derwent,<sup>7</sup> T. Devlin,<sup>32</sup> J. R. Dittmann,<sup>6</sup> S. Donati,<sup>27</sup> J. Done,<sup>34</sup> T. Dorigo,<sup>25</sup> N. Eddy,<sup>13</sup> K. Einsweiler,<sup>18</sup> J. E. Elias,<sup>7</sup> R. Ely,<sup>18</sup> E. Engels, Jr.,<sup>28</sup> W. Erdmann,<sup>7</sup> D. Errede,<sup>13</sup> S. Errede,<sup>13</sup> Q. Fan,<sup>30</sup> R. G. Feild,<sup>41</sup> Z. Feng,<sup>15</sup> C. Ferretti,<sup>27</sup> I. Fiori,<sup>2</sup> B. Flaughner,<sup>7</sup> G. W. Foster,<sup>7</sup> M. Franklin,<sup>11</sup> J. Freeman,<sup>7</sup> J. Friedman,<sup>19</sup> H. Frisch,<sup>5</sup> Y. Fukui,<sup>17</sup> S. Gadomski,<sup>14</sup> S. Galeotti,<sup>27</sup> M. Gallinaro,<sup>26</sup> O. Ganel,<sup>35</sup> M. Garcia-Sciveres,<sup>18</sup> A. F. Garfinkel,<sup>29</sup> C. Gay,<sup>41</sup> S. Geer,<sup>7</sup> D. W. Gerdes,<sup>20</sup> P. Giannetti,<sup>27</sup> N. Giokaris,<sup>31</sup> P. Giromini,<sup>9</sup> G. Giusti,<sup>27</sup> M. Gold,<sup>22</sup> A. Gordon,<sup>11</sup> A. T. Goshaw,<sup>6</sup> Y. Gotra,<sup>28</sup> K. Goulianos,<sup>31</sup> H. Grassmann,<sup>36</sup> C. Green,<sup>29</sup> L. Groer,<sup>32</sup> C. Grosso-Pilcher,<sup>5</sup> G. Guillian,<sup>20</sup> J. Guimaraes da Costa,<sup>15</sup> R. S. Guo,<sup>33</sup> C. Haber,<sup>18</sup> E. Hafen,<sup>19</sup> S. R. Hahn,<sup>7</sup> R. Hamilton,<sup>11</sup> T. Handa,<sup>12</sup> R. Handler,<sup>40</sup> W. Hao,<sup>35</sup> F. Happacher,<sup>9</sup> K. Hara,<sup>37</sup> A. D. Hardman,<sup>29</sup> R. M. Harris,<sup>7</sup> F. Hartmann,<sup>16</sup> J. Hauser,<sup>4</sup> E. Hayashi,<sup>37</sup> J. Heinrich,<sup>26</sup> A. Heiss,<sup>16</sup> B. Hinrichsen,<sup>14</sup> K. D. Hoffman,<sup>29</sup> C. Holck,<sup>26</sup> R. Hollebeek,<sup>26</sup> L. Holloway,<sup>13</sup> Z. Huang,<sup>20</sup> B. T. Huffman,<sup>28</sup> R. Hughes,<sup>23</sup> J. Huston,<sup>21</sup> J. Huth,<sup>11</sup> H. Ikeda,<sup>37</sup> M. Incagli,<sup>27</sup> J. Incandela,<sup>7</sup> G. Introzzi,<sup>27</sup> J. Iwai,<sup>39</sup> Y. Iwata,<sup>12</sup> E. James,<sup>20</sup> H. Jensen,<sup>7</sup> U. Joshi,<sup>7</sup> E. Kajfasz,<sup>25</sup> H. Kambara,<sup>10</sup> T. Kamon,<sup>34</sup> T. Kaneko,<sup>37</sup> K. Karr,<sup>38</sup> H. Kasha,<sup>41</sup> Y. Kato,<sup>24</sup> T. A. Keaffaber,<sup>29</sup> K. Kelley,<sup>19</sup> M. Kelly,<sup>20</sup> R. D. Kennedy,<sup>7</sup> R. Kephart,<sup>7</sup> D. Kestenbaum,<sup>11</sup> D. Khazins,<sup>6</sup> T. Kikuchi,<sup>37</sup> M. Kirk,<sup>3</sup> B. J. Kim,<sup>27</sup> H. S. Kim,<sup>14</sup> S. H. Kim,<sup>37</sup> Y. K. Kim,<sup>18</sup> L. Kirsch,<sup>3</sup> S. Klimenko,<sup>8</sup> D. Knoblauch,<sup>16</sup> P. Koehn,<sup>23</sup> A. Königeter,<sup>16</sup> K. Kondo,<sup>37</sup> J. Konigsberg,<sup>8</sup> K. Kordas,<sup>14</sup> A. Korytov,<sup>8</sup> E. Kovacs,<sup>1</sup> W. Kowald,<sup>6</sup> J. Kroll,<sup>26</sup> M. Kruse,<sup>30</sup> S. E. Kuhlmann,<sup>1</sup> E. Kuns,<sup>32</sup> K. Kurino,<sup>12</sup> T. Kuwabara,<sup>37</sup> A. T. Laasanen,<sup>29</sup> S. Lami,<sup>27</sup> S. Lammel,<sup>7</sup> J. I. Lamoureux,<sup>3</sup> M. Lancaster,<sup>18</sup> M. Lanzoni,<sup>27</sup> G. Latino,<sup>27</sup> T. LeCompte,<sup>1</sup> S. Leone,<sup>27</sup> J. D. Lewis,<sup>7</sup> M. Lindgren,<sup>4</sup> T. M. Liss,<sup>13</sup> J. B. Liu,<sup>30</sup> Y. C. Liu,<sup>33</sup> N. Lockyer,<sup>26</sup> O. Long,<sup>26</sup> M. Loreti,<sup>25</sup> D. Lucchesi,<sup>27</sup> P. Lukens,<sup>7</sup> S. Lusin,<sup>40</sup> J. Lys,<sup>18</sup> K. Maeshima,<sup>7</sup> P. Maksimovic,<sup>11</sup> M. Mangano,<sup>27</sup> M. Mariotti,<sup>25</sup> J. P. Marriner,<sup>7</sup> G. Martignon,<sup>25</sup> A. Martin,<sup>41</sup> J. A. J. Matthews,<sup>22</sup> P. Mazzanti,<sup>2</sup> K. McFarland,<sup>30</sup> P. McIntyre,<sup>34</sup> P. Melese,<sup>31</sup> M. Menguzzato,<sup>25</sup> A. Menzione,<sup>27</sup> E. Meschi,<sup>27</sup>

S. Metzler,<sup>26</sup> C. Miao,<sup>20</sup> T. Miao,<sup>7</sup> G. Michail,<sup>11</sup> R. Miller,<sup>21</sup> H. Minato,<sup>37</sup>  
 S. Miscetti,<sup>9</sup> M. Mishina,<sup>17</sup> S. Miyashita,<sup>37</sup> N. Moggi,<sup>27</sup> E. Moore,<sup>22</sup> Y. Morita,<sup>17</sup>  
 A. Mukherjee,<sup>7</sup> T. Muller,<sup>16</sup> A. Munar,<sup>27</sup> P. Murat,<sup>27</sup> S. Murgia,<sup>21</sup> M. Musy,<sup>36</sup>  
 H. Nakada,<sup>37</sup> T. Nakaya,<sup>5</sup> I. Nakano,<sup>12</sup> C. Nelson,<sup>7</sup> D. Neuberger,<sup>16</sup> C. Newman-  
 Holmes,<sup>7</sup> C.-Y. P. Ngan,<sup>19</sup> H. Niu,<sup>3</sup> L. Nodulman,<sup>1</sup> A. Nomerotski,<sup>8</sup> S. H. Oh,<sup>6</sup>  
 T. Ohmoto,<sup>12</sup> T. Ohsugi,<sup>12</sup> R. Oishi,<sup>37</sup> M. Okabe,<sup>37</sup> T. Okusawa,<sup>24</sup> J. Olsen,<sup>40</sup>  
 C. Pagliarone,<sup>27</sup> R. Paoletti,<sup>27</sup> V. Papadimitriou,<sup>35</sup> S. P. Pappas,<sup>41</sup> N. Parashar,<sup>27</sup>  
 A. Parri,<sup>9</sup> D. Partos,<sup>3</sup> J. Patrick,<sup>7</sup> G. Pauletta,<sup>36</sup> M. Paulini,<sup>18</sup> A. Perazzo,<sup>27</sup>  
 L. Pescara,<sup>25</sup> M. D. Peters,<sup>18</sup> T. J. Phillips,<sup>6</sup> G. Piacentino,<sup>27</sup> M. Pillai,<sup>30</sup> K. T. Pitts,<sup>7</sup>  
 R. Plunkett,<sup>7</sup> A. Pompos,<sup>29</sup> L. Pondrom,<sup>40</sup> J. Proudfoot,<sup>1</sup> F. Ptohos,<sup>11</sup> G. Punzi,<sup>27</sup>  
 K. Ragan,<sup>14</sup> D. Reher,<sup>18</sup> M. Reischl,<sup>16</sup> A. Ribon,<sup>25</sup> F. Rimondi,<sup>2</sup> L. Ristori,<sup>27</sup>  
 W. J. Robertson,<sup>6</sup> A. Robinson,<sup>14</sup> T. Rodrigo,<sup>27</sup> S. Rolli,<sup>38</sup> L. Rosenson,<sup>19</sup> R. Roser,<sup>13</sup>  
 T. Saab,<sup>14</sup> W. K. Sakumoto,<sup>30</sup> D. Saltzberg,<sup>4</sup> A. Sansoni,<sup>9</sup> L. Santi,<sup>36</sup> H. Sato,<sup>37</sup>  
 P. Schlabach,<sup>7</sup> E. E. Schmidt,<sup>7</sup> M. P. Schmidt,<sup>41</sup> A. Scott,<sup>4</sup> A. Scribano,<sup>27</sup> S. Segler,<sup>7</sup>  
 S. Seidel,<sup>22</sup> Y. Seiya,<sup>37</sup> F. Semeria,<sup>2</sup> T. Shah,<sup>19</sup> M. D. Shapiro,<sup>18</sup> N. M. Shaw,<sup>29</sup>  
 P. F. Shepard,<sup>28</sup> T. Shibayama,<sup>37</sup> M. Shimojima,<sup>37</sup> M. Shochet,<sup>5</sup> J. Siegrist,<sup>18</sup> A. Sill,<sup>35</sup>  
 P. Sinervo,<sup>14</sup> P. Singh,<sup>13</sup> K. Sliwa,<sup>38</sup> C. Smith,<sup>15</sup> F. D. Snider,<sup>7</sup> J. Spalding,<sup>7</sup>  
 T. Speer,<sup>10</sup> P. Sphicas,<sup>19</sup> F. Spinella,<sup>27</sup> M. Spiropulu,<sup>11</sup> L. Spiegel,<sup>7</sup> L. Stanco,<sup>25</sup>  
 J. Steele,<sup>40</sup> A. Stefanini,<sup>27</sup> R. Ströhmer,<sup>7a</sup> J. Strologas,<sup>13</sup> F. Strumia,<sup>10</sup> D.  
 Stuart,<sup>7</sup> K. Sumorok,<sup>19</sup> J. Suzuki,<sup>37</sup> T. Suzuki,<sup>37</sup> T. Takahashi,<sup>24</sup> T. Takano,<sup>24</sup>  
 R. Takashima,<sup>12</sup> K. Takikawa,<sup>37</sup> M. Tanaka,<sup>37</sup> B. Tannenbaum,<sup>4</sup> F. Tartarelli,<sup>27</sup>  
 W. Taylor,<sup>14</sup> M. Tecchio,<sup>20</sup> P. K. Teng,<sup>33</sup> Y. Teramoto,<sup>24</sup> K. Terashi,<sup>37</sup> S. Tether,<sup>19</sup>  
 D. Theriot,<sup>7</sup> T. L. Thomas,<sup>22</sup> R. Thurman-Keup,<sup>1</sup> M. Timko,<sup>38</sup> P. Tipton,<sup>30</sup>  
 A. Titov,<sup>31</sup> S. Tkaczyk,<sup>7</sup> D. Toback,<sup>5</sup> K. Tollefson,<sup>30</sup> A. Tollestrup,<sup>7</sup> H. Toyoda,<sup>24</sup>  
 W. Trischuk,<sup>14</sup> J. F. de Troconiz,<sup>11</sup> S. Truitt,<sup>20</sup> J. Tseng,<sup>19</sup> N. Turini,<sup>27</sup> T. Uchida,<sup>37</sup>  
 F. Ukegawa,<sup>26</sup> J. Valls,<sup>32</sup> S. C. van den Brink,<sup>15</sup> S. Vejcik, III,<sup>7</sup> G. Velez,<sup>27</sup>  
 I. Volobouev,<sup>18</sup> R. Vidal,<sup>7</sup> R. Vilar,<sup>7a</sup> D. Vucinic,<sup>19</sup> R. G. Wagner,<sup>1</sup> R. L. Wagner,<sup>7</sup>  
 J. Wahl,<sup>5</sup> N. B. Wallace,<sup>27</sup> A. M. Walsh,<sup>32</sup> C. Wang,<sup>6</sup> C. H. Wang,<sup>33</sup> M. J. Wang,<sup>33</sup>  
 A. Warburton,<sup>14</sup> T. Watanabe,<sup>37</sup> T. Watts,<sup>32</sup> R. Webb,<sup>34</sup> C. Wei,<sup>6</sup> H. Wenzel,<sup>16</sup>

W. C. Wester, III,<sup>7</sup> A. B. Wicklund,<sup>1</sup> E. Wicklund,<sup>7</sup> R. Wilkinson,<sup>26</sup> H. H. Williams,<sup>26</sup>  
 P. Wilson,<sup>7</sup> B. L. Winer,<sup>23</sup> D. Winn,<sup>20</sup> D. Wolinski,<sup>20</sup> J. Wolinski,<sup>21</sup> S. Worm,<sup>22</sup>  
 X. Wu,<sup>10</sup> J. Wyss,<sup>27</sup> A. Yagil,<sup>7</sup> W. Yao,<sup>18</sup> K. Yasuoka,<sup>37</sup> G. P. Yeh,<sup>7</sup> P. Yeh,<sup>33</sup> J. Yoh,<sup>7</sup>  
 C. Yosef,<sup>21</sup> T. Yoshida,<sup>24</sup> I. Yu,<sup>7</sup> A. Zanetti,<sup>36</sup> F. Zetti,<sup>27</sup> and S. Zucchelli<sup>2</sup>

(CDF Collaboration)

<sup>1</sup> *Argonne National Laboratory, Argonne, Illinois 60439*

<sup>2</sup> *Istituto Nazionale di Fisica Nucleare, University of Bologna, I-40127 Bologna, Italy*

<sup>3</sup> *Brandeis University, Waltham, Massachusetts 02254*

<sup>4</sup> *University of California at Los Angeles, Los Angeles, California 90024*

<sup>5</sup> *University of Chicago, Chicago, Illinois 60637*

<sup>6</sup> *Duke University, Durham, North Carolina 27708*

<sup>7</sup> *Fermi National Accelerator Laboratory, Batavia, Illinois 60510*

<sup>8</sup> *University of Florida, Gainesville, Florida 32611*

<sup>9</sup> *Laboratori Nazionali di Frascati, Istituto Nazionale di Fisica Nucleare, I-00044 Frascati, Italy*

<sup>10</sup> *University of Geneva, CH-1211 Geneva 4, Switzerland*

<sup>11</sup> *Harvard University, Cambridge, Massachusetts 02138*

<sup>12</sup> *Hiroshima University, Higashi-Hiroshima 724, Japan*

<sup>13</sup> *University of Illinois, Urbana, Illinois 61801*

<sup>14</sup> *Institute of Particle Physics, McGill University, Montreal H3A 2T8, and University of Toronto,  
 Toronto M5S 1A7, Canada*

<sup>15</sup> *The Johns Hopkins University, Baltimore, Maryland 21218*

<sup>16</sup> *Institut für Experimentelle Kernphysik, Universität Karlsruhe, 76128 Karlsruhe, Germany*

<sup>17</sup> *National Laboratory for High Energy Physics (KEK), Tsukuba, Ibaraki 305, Japan*

<sup>18</sup> *Ernest Orlando Lawrence Berkeley National Laboratory, Berkeley, California 94720*

<sup>19</sup> *Massachusetts Institute of Technology, Cambridge, Massachusetts 02139*

<sup>20</sup> *University of Michigan, Ann Arbor, Michigan 48109*

<sup>21</sup> *Michigan State University, East Lansing, Michigan 48824*

- <sup>22</sup> *University of New Mexico, Albuquerque, New Mexico 87131*
- <sup>23</sup> *The Ohio State University, Columbus, Ohio 43210*
- <sup>24</sup> *Osaka City University, Osaka 588, Japan*
- <sup>25</sup> *Universita di Padova, Istituto Nazionale di Fisica Nucleare, Sezione di Padova, I-35131 Padova, Italy*
- <sup>26</sup> *University of Pennsylvania, Philadelphia, Pennsylvania 19104*
- <sup>27</sup> *Istituto Nazionale di Fisica Nucleare, University and Scuola Normale Superiore of Pisa, I-56100 Pisa, Italy*
- <sup>28</sup> *University of Pittsburgh, Pittsburgh, Pennsylvania 15260*
- <sup>29</sup> *Purdue University, West Lafayette, Indiana 47907*
- <sup>30</sup> *University of Rochester, Rochester, New York 14627*
- <sup>31</sup> *Rockefeller University, New York, New York 10021*
- <sup>32</sup> *Rutgers University, Piscataway, New Jersey 08855*
- <sup>33</sup> *Academia Sinica, Taipei, Taiwan 11530, Republic of China*
- <sup>34</sup> *Texas A&M University, College Station, Texas 77843*
- <sup>35</sup> *Texas Tech University, Lubbock, Texas 79409*
- <sup>36</sup> *Istituto Nazionale di Fisica Nucleare, University of Trieste/ Udine, Italy*
- <sup>37</sup> *University of Tsukuba, Tsukuba, Ibaraki 305, Japan*
- <sup>38</sup> *Tufts University, Medford, Massachusetts 02155*
- <sup>39</sup> *Waseda University, Tokyo 169, Japan*
- <sup>40</sup> *University of Wisconsin, Madison, Wisconsin 53706*
- <sup>41</sup> *Yale University, New Haven, Connecticut 06520*

# Bibliography

- [1] J.J. Thompson, *Phil. Mag.* **44**, 293 (1897);  
*idem.*, *Nature* **55**, 453 (1897).
- [2] E. Rutherford, *Phil. Mag.* **21**, 669 (1911).
- [3] J. Chadwick, *Nature*, No. 3252, Vol. 129, 312 (1932).
- [4] C.D. Anderson, *Phys. Rev.* **43**, 491 (1933).
- [5] S.H. Neddermeyer and C.D. Anderson, *Phys. Rev.* **51**, 884 (1937).
- [6] F. Reines and C.L. Cowan, Jr., *Phys. Rev.* **92**, 8301 (1953).
- [7] M. Gell-Mann, *Phys. Lett.* **8**, 214 (1964).
- [8] G. Zweig, CERN-8419-TH-412 (1964).
- [9] UA1 Collab., G. Arnison *et al.*, *Phys. Lett.* **122B**, 103 (1983).
- [10] CDF Collab., F. Abe *et al.*, *Phys. Rev. Lett.* **74**, 2626 (1995).
- [11] DØ Collab., S. Abachi *et al.*, *Phys. Rev. Lett.* **74**, 2632 (1995).
- [12] CDF Collab., F. Abe *et al.*, *Phys. Rev. Lett.* **77**, 438 (1996).
- [13] CDF Collab., F. Abe. *et al.*, *Phys. Rev. Lett.* **80**, 3461 (1998).
- [14] R.P. Feynman, *Phys. Rev. Lett.* **23**, 1415 (1969);  
J.D. Bjorken and E.A. Paschos, *Phys. Rev.* **185**, 1975 (1969).

- [15] T.Muta, *Foundations of Quantum Chromodynamics*, World Scientific, Singapore, 1987.
- [16] V.D.Barger and R.J.N.Phillips, *Collider Physics*, Addison-Wesley, Redwood City, CA, 1987.
- [17] S.L.Glashow, Nucl. Phys. **22**, 579 (1961);  
A. Salam and J.C. Ward, Phys. Lett. **13**, 168 (1964);  
S. Weinberg, Phys. Rev. Lett. **19**, 1264 (1967).
- [18] P.W.Higgs, Phys. Rev. Lett. **13**, 508 (1964);  
*idem.*, Phys. Rev. **145**, 1156 (1966).
- [19] M. Gell-Mann, *The Quark and the Jaguar*, W.H. Freeman, New York, NY (1994).
- [20] W. Pauli, Z. Phys. **31**, 765 (1925).
- [21] J.D. Bjorken, Phys. Rev. **179**, 1547 (1969).
- [22] W. Heisenberg, Z. Phys. **43**, 172 (1927).
- [23] J. Friedman and I. Kendall, Ann. Rev. Nucl. Part. Sc. **22**, 203 (1972) (review).
- [24] D.J. Fox *et al.*, Phys. Rev. Lett, **33**, 1504 (1979).
- [25] S. Weinberg, Phys. Rev. Lett. **31**, 494 (1973);  
H. Fritzsch, M. Gell-Mann and H. Leutwyler, Phys. Lett. **47B**, 365 (1973);  
D.J. Gross and F. Wilczek, Phys. Rev. **D8**, 3633 (1973).
- [26] R.D. Field, *Applications of Perturbative QCD*, Addison-Wesley, Reading, MA, 1989.
- [27] F. Halzen and A.D. Martin, *Quarks & Leptons*, Wiley and Sons, New York, 1984.

- [28] D.J. Gross and F. Wilczek, Phys. Rev. Lett. **30**, 1343 (1973);  
H.D. Pollitzer, Phys. Rev. Lett. **30**, 1346 (1973).
- [29] The Particle Data Group, C. Caso *et al.*, *Review of Particle Physics*, Eur. Phys. J. C **3**, 1 (1998).
- [30] G. Altarelli and G. Parisi, Nucl. Phys. **B126**, 298 (1977).
- [31] V.N. Gribov and L.N. Lipatov, Sov. J. Nucl. Phys. **15**, 438 (1972).
- [32] Yu.L. Dokshitzer, Sov. Phys. JETP **46**, 641 (1972).
- [33] J.J. Lord, J. Fainberg and M. Schein, Phys. Rev. **80**, 970 (1950).
- [34] G. Hanson *et al.*, Phys. Rev. Lett. **35**, 1609 (1975).
- [35] D.P. Barber *et al.*, Phys. Rev. Lett. **43**, 830 (1979);  
Tasso Collab., R. Brandelik *et al.*, Phys. Lett. **86B**, 243 (1979).
- [36] UA2 Collab., M. Banner *et al.*, Phys. Lett. **118B**, 203 (1982).
- [37] S. Bethke, *Hadron Physics in Electron-Positron Annihilation*, HD-PY 93/7, 1993.
- [38] R.P. Feynman and R.D. Field, Nucl. Phys. **136**, 1 (1978).
- [39] T. Sjöstrand, Comput. Phys. Commun. **27**, 243 (1982);  
*idem.*, Comput. Phys. Commun. **39**, 347 (1986);  
*idem.*, *The LUND Monte Carlo Programs*, CERN Long Writeup, 1989.
- [40] D.H. Perkins, *Introduction to High Energy Physics*, Addison-Wesley, 3<sup>rd</sup> Edition, Menlo Park, CA, 1987.
- [41] R.K. Ellis, W.J. Stirling and B.R. Webber, *QCD and Collider Physics*, Cambridge University Press, Cambridge, 1996.
- [42] L.M. Lederman, *Scientific American*, 48 (1991).

- [43] A. Warburton, *A Study of Exclusive Nonleptonic Decays of B Mesons into Final States of Strange Mesons and 1S or 2S Charmonia*, Ph.D. Thesis, University of Toronto (1997).
- [44] D. Möhl, G. Petrucci, L. Thorndahl and S. van der Meer, Phys. Rep. **58**, 73 (1980)
- [45] These and other Tevatron parameters are available at <http://www-fermi3.fnal.gov/>.
- [46] CDF Collab., F. Abe *et al.*, Nucl. Instrum. Meth. A **271**, 387 (1988).
- [47] CDF Collab., F. Abe *et al.*, Phys. Rev. D **50**, 2966 (1994).
- [48] P. Azzi *et al.*, Nucl. Instrum. Meth. A **360**, 73 (1995).
- [49] F. Bedeschi *et al.*, Nucl. Instrum. Meth. A **268**, 50 (1988).
- [50] L. Balka *et al.*, Nucl. Instrum. Meth. A **267**, 272 (1988).
- [51] S. Bertolucci *et al.*, Nucl. Instrum. Meth. A **267**, 301 (1988).
- [52] Y. Fukui *et al.*, Nucl. Instrum. Meth. A **267**, 280 (1988).
- [53] S. Cihangir *et al.*, Nucl. Instrum. Meth. A **267**, 249 (1988).
- [54] R.M. Harris, *Two Jet Differential Cross Section and Structure Functions in  $\bar{p}p$  Collisions at  $\sqrt{s} = 1.8$  TeV*, Ph.D. Thesis, University of California at Berkeley, LBL-27246 (1989).
- [55] G. Ascoli *et al.*, Nucl. Instrum. Meth. A **268**, 33 (1988).
- [56] J.D. Lewis *et al.*, *The 1992 CDF Muon System Upgrade*, CDF Note 2858 (1995).
- [57] K. Byrum *et al.*, Nucl. Instrum. Meth. A **268**, 46 (1988).
- [58] D. Amidei *et al.*, Nucl. Instrum. Meth. A **265**, 326 (1988).

- [59] K.D. Hoffman, *The Search for Physics Beyond the Standard Model in the  $b\bar{b}$  Spectrum Observed in Tevatron Proton-Antiproton Collisions*, Ph.D. Thesis, Purdue University (1998).
- [60] J.T. Carroll *et al.*, Nucl. Instrum. Meth. A **300**, 552 (1991).
- [61] JADE Collab., W. Bartel *et al.*, Z. Phys. **C33**, 23 (1986).  
JADE Collab., S. Bethke *et al.*, Phys. Lett. **B213**, 235 (1988).
- [62] S. Catani *et al.*, Phys. Lett. **269B**, 432 (1991).
- [63] CDF Collab., F. Abe *et al.*, Phys. Rev. D **45**, 1448 (1992).
- [64] B. Flaughner and J. Mueller, *A Guide to JETCLU: The CDF Jet Clustering Algorithm*, CDF Note 1814 (1992).
- [65] UA2 Collab., J. Alitti *et al.*, Z. Phys. **C49**, 17 (1991).
- [66] L. Keeble, *A Study of Four-Jet Events and Search for Double Parton Interactions with the Collider Detector at Fermilab*, Ph.D. Thesis, Texas A&M University, CDF Note 1860 (1992).
- [67] A. Bhatti, *A Few More Studies of the Inclusive Jet Cross Section for the 1992-1993 Data Set*, CDF Note 3003 (1995).
- [68] A. Bhatti, *The Inclusive Jet Cross Section from run 1B*, CDF Note 3642 (1996).
- [69] T. Sjöstrand, Comput. Phys. Commun. **82**, 74 (1994).
- [70] W.R. Leo, *Techniques for Nuclear and Particle Physics Experiments*, Springer Verlag, Berlin, 1987.
- [71] C. Fabjan, *Calorimetry in High-Energy Physics*, in T. Ferbel, *Experimental Techniques in High-Energy Physics*, Addison-Wesley, Menlo Park, CA, 1987.
- [72] B. Rossi, *High-Energy Particles*, Prentice-Hall, New York, NY, 1964.

- [73] *GEANT - Detector Description and Simulation Tool*, CERN Program Library Writeup W5013, Geneva 1994.
- [74] B. Hinrichsen, J.K. Mayer and W. Trischuk, *Calibrating the Electromagnetic Energy Response of the Fast Plug Upgrade Calorimeter Simulation*, CDF Note 4479 (1998).
- [75] CDF II Collab., R. Blair *et al.*, *The CDF Detector Technical Design Report*, Fermilab-Pub-96/390-E, 1996.
- [76] R.C. Fernow, *Introduction to experimental particle physics*, Cambridge University Press, Cambridge, 1986.
- [77] F. James, CERN Program Library Long Writeup D506 (unpublished), available at <http://wwwinfo.cern.ch/asdoc/minuit.html3/minmain.html>.
- [78] M. Shapiro, *Some Comparisons of the Energy Scale of QFL Version 3.10 with Development*, CDF Note 3603 (1996).
- [79] S. Behrends, *A Plot of the Systematic Uncertainty on Jet  $E_t$* , CDF Note 3550 (1996).
- [80] S. Behrends, T. Devlin and M.D. Shapiro *Godparent Report: Run 1A Inclusive Jet  $E_t$  Spectrum Analysis*, CDF Note 3422 (1995).
- [81] C. Wei and R.M. Harris, *Dijet Angular Distribution from Run 1A+1B*, CDF Note 3637 (1996).
- [82] E. Kovács, *Jet Energy Resolutions from Dijet Balancing*, CDF Note 2608 (1995).
- [83] D. Cronin-Hennessy and A. Beretvas, *Luminosity at CDF*, CDF Note 4721 (1998).
- [84] W.T. Giele, E.W.N. Glover and D.A. Kosower, Nucl. Phys. **B 403**, 633 (1993).
- [85] W.T. Giele, E.W.N. Glover and D.A. Kosower, Phys. Rev. Lett **73**, 2019 (1994).

- [86] CTEQ Collab., H.L. Lai *et al.*, Phys. Rev. **D55**, 1280 (1997).
- [87] A.D. Martin, R.G. Roberts, W.J. Stirling and R.S. Thorne, Eur. Phys. J. **C 4**, 463 (1998).
- [88] CTEQ Collab., H.L. Lai *et al.*, Phys. Rev. **D51**, 4763 (1995).
- [89] A.D. Martin, R.G. Roberts and W.J. Stirling, Phys. Lett. **B387**, 419 (1996).
- [90] A.D. Martin, R.G. Roberts and W.J. Stirling, Phys. Lett. **B306**, 145 (1993).
- [91] J. Huston, private communication.
- [92] L. Lyons, *Statistics for Nuclear and Particle Physicists*, Cambridge University Press, Cambridge, 1989;  
T. Devlin, *Jet Inclusive Cross Sections: A Statistical Study of the "Excess"*, CDF Note 3301 (1995).
- [93] DØ Collab., B. Abbott *et al.*, hep-ex/980714 (1998), submitted to Phys. Rev. Lett.